

**Biopolymers:
from structural hierarchy to nonlinear rheology**

Izabela Katarzyna Piechocka



©2011, Izabela K. Piechocka. All rights reserved.

The work described in this thesis was performed at the FOM Institute (AMOLF), Science Park 104, 1098 XG Amsterdam, The Netherlands. This work is part of the research programme of the *Stichting voor Fundamenteel Onderzoek der Materie* (FOM), which is financially supported by the *Nederlandse Organisatie voor Wetenschappelijk Onderzoek* (NWO).

ISBN 978-90-77209-54-7

A digital version of this thesis can be downloaded from www.uvu.vu.nl/dissertations.
Printed copies can be obtained by addressing the library at the FOM Institute
AMOLF: library@amolf.nl.

VRIJE UNIVERSITEIT

**Biopolymers:
from structural hierarchy to nonlinear rheology**

ACADEMISCH PROEFSCHRIFT

ter verkrijging van de graad Doctor aan
de Vrije Universiteit Amsterdam,
op gezag van de rector magnificus
prof.dr. L.M. Bouter,
in het openbaar te verdedigen
ten overstaan van de promotiecommissie
van de faculteit der Exacte Wetenschappen
op woensdag 23 november 2011 om 9.45 uur
in de aula van de universiteit,
De Boelelaan 1105

door

Izabela Katarzyna Piechocka

geboren te Poznań, Polen

promotoren: prof.dr. G. H. Koenderink
prof.dr. F. C. MacKintosh

*Science exists
because we
do not know*

overige leden: prof.dr. H. Herrmann
dr. D. Iannuzzi
dr. C. Storm
prof.dr. D. Weitz
prof.dr. G. Wuite

PUBLICATIONS COVERED IN THIS THESIS

- I. K. Piechocka**, R. G. Bacabac, M. Potters, F. C. MacKintosh, G. H. Koenderink.
Structural hierarchy governs fibrin gel mechanics. *Biophysical Journal* *98*, 2281-2289 (2010).
- I. K. Piechocka**, A. S. G. van Oosten, R. G. M. Breuls, G. H. Koenderink.
Rheology of heterotypic collagen networks. *Biomacromolecules* *12*, 2797-805 (2011).
- I. K. Piechocka**, K. Jansen, C. P. Broedersz, F. C. MacKintosh, G. H. Koenderink.
Contribution of fiber microstructure to fibrin network mechanics. Manuscript in preparation.
- I. K. Piechocka**, B. Alonso-Latorre, G. H. Koenderink.
Fingerprinting the nonlinear rheology of fibrin clots. Manuscript in preparation.

OTHER PUBLICATIONS

- K. Jansen, R. G. Bacabac, **I. K. Piechocka**, G. H. Koenderink.
Cell traction in a biomimetic tissue model. Manuscript in preparation.
- J. Gutek, S. Winiarz, **I. K. Piechocka**, P. Płotka, R. Czajka.
Investigation of the coulomb blockade effect in double tunnel junctions. *Metrology and Measurements Systems XII* (2006).

CONTENTS

1	Introduction: The structural and mechanical integrity of the cell	11
1.1	Cytoskeleton and extracellular matrix	12
1.2	Biopolymers: supramolecular protein architectures	13
1.3	Nonlinear elasticity of biopolymer networks	15
1.3.1	Enthalpic and entropic contributions to network elasticity	15
1.3.2	Nonaffinity crossover point	16
1.4	Outstanding questions	17
1.5	Scope of this thesis	18
2	Measurement techniques	21
2.1	Structural characterization	22
2.1.1	Network characterization by confocal microscopy	22
2.1.2	Filament characterization by electron and atomic force microscopy	23
2.1.3	Filament characterization by turbidimetry	24
2.2	Mechanical measurements	25
2.2.1	Macroscopic rheometry	25
2.2.2	Optical Tweezer microrheology	26
3	Structural hierarchy governs fibrin gel mechanics	29
3.1	Introduction	30
3.2	Sample preparation	32
3.3	Results and Discussion	32
3.3.1	Network structure and single fiber mechanics	32
3.3.2	Low-strain mechanics of fibrin gels	35
3.3.3	High-strain mechanics of fibrin gels	38
3.4	Conclusion	44
3.5	Appendix	44
3.5.1	Calculations of fiber persistence length based on a bundle model	44
3.5.2	Calculations of the protofibril stretch modulus	45
4	Contribution of fiber microstructure to fibrin network mechanics	47
4.1	Introduction	48
4.2	Sample preparation	49
4.3	Results and Discussion	49
4.3.1	Network and bundle structure	49

4.3.2	Low-strain mechanics of fibrin gels	53
4.3.3	Nonlinear rheology of fine clots	54
4.3.4	Comparison between fine and coarse clot rheolog	61
4.4	Conclusion	63
5	Fingerprinting the nonlinear rheology of fibrin clots	65
5.1	Introduction	66
5.2	Experiments	70
5.3	Results	70
5.3.1	Nonlinear elasticity probed by LAOS and prestress tests .	70
5.3.2	Decomposition of the time-dependent oscillatory strain response	72
5.4	Discussion and concluding remarks	78
6	Molecular composition influences collagen gel mechanics	81
6.1	Introduction	82
6.2	Sample preparation	83
6.3	Results	84
6.3.1	Rheology of mixed collagen I/V networks	84
6.3.2	Collagen network microstructure	87
6.3.3	Quantification of fibril diameter	88
6.4	Discussion	93
6.5	Conclusion	98
6.6	Appendix	98
6.6.1	Summary of Young's moduli (E) and persistence lengths (l_p) determined for hydrated collagen fibrils	98
7	<i>In vitro</i> reconstitution of composite networks of vimentin and microtubules	101
7.1	Introduction	102
7.2	Sample preparation	104
7.2.1	Vimentin network purification and assembly	104
7.2.2	Composite vimentin-microtubule network assembly	105
7.3	Results	105
7.3.1	Network and filament structure	105
7.3.2	Mechanics of vimentin-microtubule networks	110
7.4	Discussion and concluding remarks	114
8	Towards <i>in situ</i> visualization of biopolymer networks under shear	117
8.1	Introduction	118
8.2	Parallel plate shear cell	120
8.3	Electronics and software interface to control shear deformation .	123
8.4	Fibrin network under shear	124
8.5	Conclusions and Outlook	125
	Bibliography	127

Summary	153
Samenvatting	157
Acknowledgement	161
Curriculum Vitae	165

1 INTRODUCTION:
THE STRUCTURAL AND
MECHANICAL INTEGRITY
OF THE CELL

1.1 CYTOSKELETON AND EXTRACELLULAR MATRIX

The cell is a composite, highly dynamic and heterogeneous system. Its shape, mechanical functions, and ability to adapt to changing circumstances are all controlled from within, by the *cytoskeleton* (CSK). The CSK is a network composed of three different filament types: actin microfilaments (MFs), microtubules (MTs) and intermediate filaments (IFs) (Fig. 1.1). These filaments contribute in distinct ways to the overall mechanical behavior of cells. Moreover, they may collectively balance preexisting forces inside the cell via local compression and tension [147, 278]. Actin and intermediate filaments are able to resist internal tension by stretching their bent shape. The stiffer microtubules, on the other hand, can bear larger compressive loads. The efficacy of this system is ensured by the presence of accessory proteins that link the filaments to each other and to other cell components. Unlike conventional, polymeric materials, the cytoskeleton can actively generate forces by means of active filament (de)polymerization and the action of motor proteins. As a result, cells can autonomously adapt their shape and mechanical behavior [196].

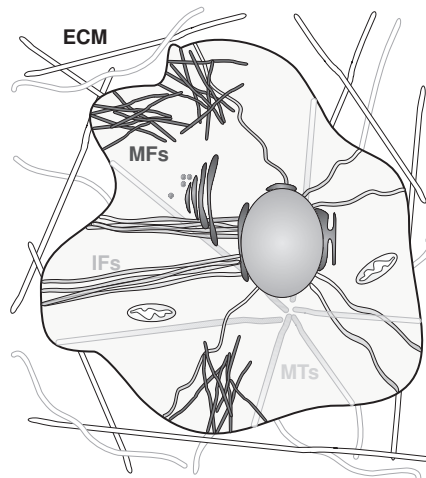


FIGURE 1.1. Schematic representation of a cell embedded in an extracellular matrix (ECM). Actin microfilaments (MFs) are attached to cell adhesion sites and contribute with myosin motors to cellular contraction. Microtubules (MTs) span the cell interior and provide tracks for transport of vesicles, proteins, and organelles by motor proteins. Intermediate filaments (IFs) link the nucleus (grey shaded oval) with the cell periphery, creating a supporting framework that distributes stresses.

Cellular functions are highly dependent on the surrounding *extracellular matrix* (ECM). This fibrous matrix composed of various macromolecules produced by cells provides an anchoring support to cells and helps to bind cells together to form tissues. The ECM is mainly composed of fibrous proteins such as collagen, elastin, fibronectin and laminin that strongly interact with each other [142]. The cytoskeleton inside cells is physically anchored to the ECM by means of

transmembrane proteins known as integrins. This connection enables cells to control the spatial organization of the ECM by the application of contractile forces, while at the same time contributing to ECM-dependent changes in cell shape [301].

1.2 BIOPOLYMERS: SUPRAMOLECULAR PROTEIN ARCHITECTURES

Proteins are made up of one or more long polypeptide chains, which are linear chains of different amino acids in a specific sequence that is encoded in an organism's genes. This sequence dictates how the polypeptide chains fold. There are various folding motifs, of which the α -helix or β -sheet are most prevalent. Proteins typically fold into a globular form (e.g. actin, tubulin) or fibrous form (e.g. intermediate filaments, fibrin, collagen). Self-assembly of many identical protein molecules driven by specific non-covalent interactions leads to formation of filaments constituting the cytoskeleton and the ECM.

The supramolecular architecture of the CSK and ECM fibers is specific for each filament type. Actin and microtubules are polar structures made of globular protein subunits held primarily by longitudinal bonds (Fig. 1.2 A-B). The weaker lateral bonds allow individual protofilaments to twist around each other to form a helical lattice in case of actin and helical tube in case of MTs. These relatively weak interactions make the filaments largely inextensible and rather fragile. Weak assembly allows, however, for rapid turnover of individual subunits and thereby helps to dynamically rearrange the cell's interior, which is necessary for cell locomotion as well as for intracellular transport. Fibers from the ECM, like collagen and fibrin, are on the other hand more stable, and their supramolecular architecture is reinforced by covalent bonds between their protein subunits.

The hierarchical architecture of protein biopolymers confers remarkable mechanical properties. Intermediate filaments, for instance, are extremely extensible due to their rope-like structure (Fig. 1.2 C). IFs lack the overall structural polarity that is characteristic for actin filament and microtubules and their multiple protofilament organization makes them easier to bent and more difficult to break compared to actin and microtubules. Fibers from the IF family can be stretched up to 4 times their original length [163], even though the lateral bonds that connect subunits are relatively strong. The high extensibility of IFs is a consequence of their multilevel architecture that is sensitive to an applied force. Under increased levels of deformation, stretching of individual protofilaments followed by molecular unfolding takes place [241]. A similar fiber stretching mechanism is observed for fibrin, which is the main blood clotting factor and an extracellular matrix protein. Due to a half-staggered organization of the fibrin molecules in protofibrils and further hierarchical assembly into fibers (Fig. 1.2 D), a succession of different structural levels is achieved. This, in return, results in a high extensibility of individual filaments [191] that is further enhanced by flexible polypeptide domains that connect the protofibrils [82].

Complex structural hierarchy does not always favor high extensibility of

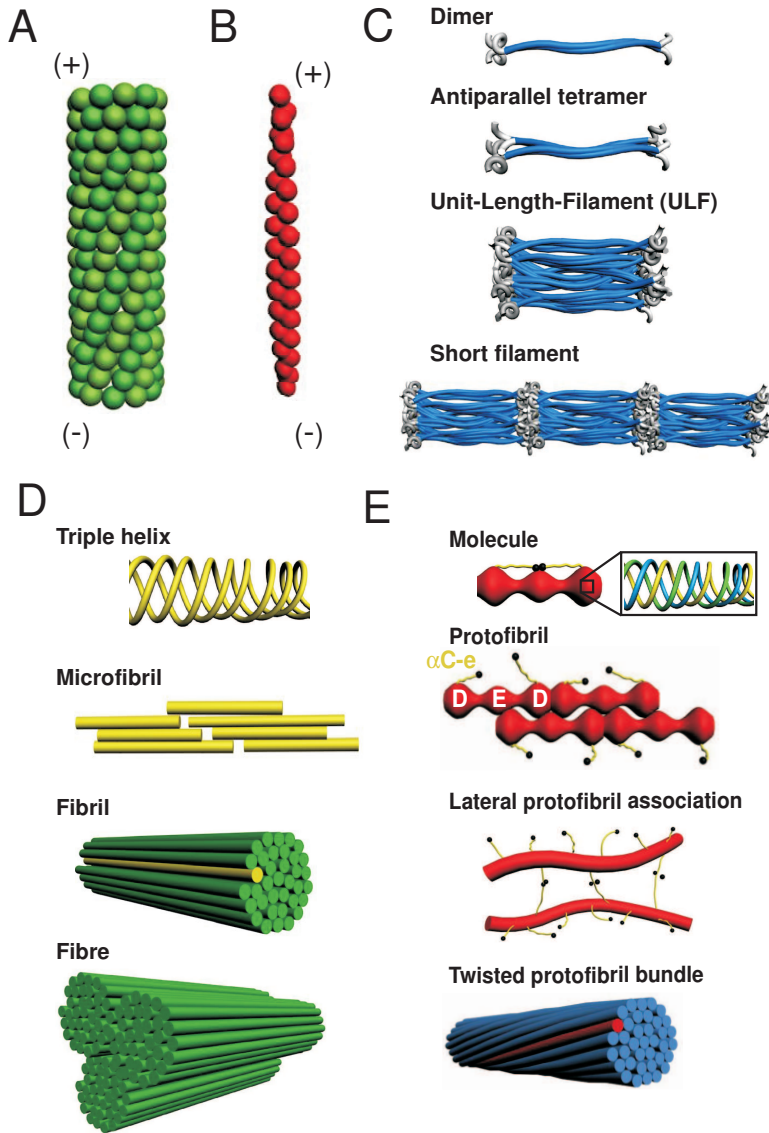


FIGURE 1.2. Supramolecular architecture of various protein filaments. Microtubules (A) and actin filaments (B) are polar filaments built up from globular protein subunits (actin and tubulin). Intermediate filaments (C) do not possess polarity due to an antiparallel arrangement of the fibrous protein subunits. Collagen fibres (D) are self-assembled from triple helical tropocollagen molecules in a quarter-staggered arrangement. Collagen microfibrils laterally and longitudinally associate into fibrils, and fibrils bundle to form fibres. Fibrin fibers (E) are twisted bundles of loosely coupled protofibrils, which are made of fibrin molecules in a half-staggered arrangement.

filaments. Collagen, the most abundant ECM protein in human tissue, is built from three long polypeptide chains wound into a triple helix. This tropocollagen molecule binds side-by-side and end-to-end to other tropocollagen molecules to form collagen fibrils (Fig. 1.2 E). Due to rigid connections between individual molecules, collagen fibers, like actin filaments and microtubules, are not very extensible. Yet, collagen's hierarchical organization allows for viscous sliding of subunits and results in very tough filaments [45].

1.3 NONLINEAR ELASTICITY OF BIOPOLYMER NETWORKS

Differences in the structure and self-assembly of subunits endow filaments with distinct mechanical properties. The largest difference between different filament types is evident from their highly disparate bending rigidities. Actin filaments are rather flexible filaments with diameter of $d \sim 7$ nm and the persistence length of $l_p \sim 17 \mu\text{m}$ [97]. Due to the structural organization these filaments are hard to stretch and easy to break. Hollow cylindrical microtubules ($d \sim 25$ nm and $l_p \sim 5$ mm) [97] are strong and rigid but fragile, while rope-like intermediate filaments ($d \sim 9$ nm and $l_p \sim 1 \mu\text{m}$) [182, 210] are easy to bend but hard to break. By contrast, ECM filaments have diameters that are at least 10-fold larger than those of cytoskeleton filaments. Nevertheless, those filaments can still be classified as a *semiflexible* polymers since their persistence length is comparable to their contour length, L_0 .

In living cells biopolymer filaments form crosslinked and bundled structures that are much stronger than individual filaments. *In vitro* reconstituted networks of different filament types, both from the cytoskeleton and ECM, have distinct mechanical properties and dynamics. However, these networks all show a common response to an applied stress: their network stiffness remains constant at small deformations but it increases nonlinearly at high stresses [285]. This unusual *strain-stiffening* response of biopolymers makes them different from most synthetic polymers and is thought to help protect cells and tissues from mechanical damage.

1.3.1 ENTHALPIC AND ENTROPIC CONTRIBUTIONS TO NETWORK ELASTICITY

The degree and the type of elastic nonlinearity in biopolymer networks depend on the network microstructure [177, 57], cross-linker density [177, 94] and processes such as cross-linker unbinding [175], stretching [41] and unfolding [71]. The stress-stiffening behavior has been shown to originate either from the entropic (*thermal*, E) elasticity of individual filaments [195] or from the enthalpic (*athermal*, mechanical, M) elasticity arising from network rearrangement or filament buckling [224]. The former corresponds to a more uniform (or *affine*, A) strain field, while the latter corresponds to a highly non-uniform (*nonaffine*, NA) strain field. Which of these two regimes is expected

depends on network connectivity and density. The nonaffine regime is characteristic of sparsely crosslinked networks, as shown by 2D [72, 118, 311, 67] and 3D computer simulations [49, 144]. In this limit, the shear modulus scales linearly with bending modulus of the filaments, κ [166, 262]. There are, however, no simple analytical models that can quantitatively describe the elasticity in this regime. The affine regime applies to densely crosslinked, homogenous networks. Since all filaments experience exactly the same deformations, the network elasticity can be calculated analytically from the density of the fibers and their single-fiber stretching rigidity, μ , by orientationally averaging over all fibers [285, 94]. This analytical model predicts that the network stiffness scales with protein concentration, c , according to $G_0 \sim c^{11/5}$ for a thermal (AE) system [195] and as $G_0 \sim c^1$ for an athermal (AM) system [119]. Any nonaffinity will tend to lower the network stiffness by increasing the number of degrees of freedom in the system.

1.3.2 NONAFFINITY CROSSOVER POINT

Sparsely crosslinked, heterogeneous networks exhibit a spatially inhomogeneous strain field even when the applied shear is uniform. The filaments therefore undergo reorientations rather than alignment in the shear direction as predicted by continuum elastic theory. This results in the elastic energy being predominantly stored in bending deformations and networks that are overall softer since only few filaments can store elastic energy. Nonaffine deformations can occur not only in case of low density networks, but they also occur in heterogeneous bundle systems [177, 134, 133] and were postulated affect even the mechanical behavior of high density F-actin networks [94].

The transition between NA/A regimes of deformation depends strongly on the density of filaments and three different filament length scales: the filament contour length, L_0 , the mean crosslink distance, l_c , and the bending length, l_b , that relates the bending and stretching moduli of filaments according to $l_b = (\kappa/\mu)^{1/2}$ [119]. In 2D random networks of monodisperse rods, the distribution of stress between stretching and bending modes is captured by the so-called nonaffinity length, λ , [119]. Scaling by this length universally captures the effect of changing l_c and the filament stiffness. The ratio of L/λ can therefore be used to establish what regime the network is in.

Recent lattice simulations and analytic theories have shown that, in addition to crosslink density and filament length, there is one more key parameter that defines the affine transition point, namely the network connectivity, z [40]. In case of a local connectivity of $z=3$ that corresponds to a branched network, the deformation field is expected to crossover from nonaffine to affine at a dimensionless ratio of bending to stretching rigidity, $\kappa_{bend}/\kappa_{stretch} l_c^2$ of 10^{-2} . Below this crossover point, fiber bending dominates, while above it, affine stretching dominates, in accordance with prior theoretical and computational studies. However around this crossover point, a remarkably broad intermediate regime exists. In this mixed stretch/bend regime, the shear modulus scales simultaneously with κ and μ .

The presence of other filamentous components that differ in length and rigid-

ity can also have effect on the A/NA crossover point. It was shown in polydisperse networks that the presence of stiffer filaments homogenizes the initially nonaffine strain field of monodisperse system in the linear mechanical regime, increases the shear modulus and shifts the mechanics of the network from nonaffine to affine even at low network densities [11, 10, 181]. This mechanism is only apparent close to the NA/A transition regime, while deep in the nonaffine regime stiff filaments redistribute nonaffine deformations making the system even more nonuniform [10]. In this case there is, however, no simple definition of the crossover point.

1.4 OUTSTANDING QUESTIONS

Most of the existing theoretical models that are commonly used to describe the nonlinear response of biopolymer network to large deformations treat the individual filament as isotropic inextensible rods with constant diameter. While some types of filaments, such as actin and microtubules, are indeed rather inextensible, the majority of biopolymer filaments from the cytoskeleton and ECM show a high extensibility that can be accounted for by their complex internal architecture. Recently the affine entropic model extended to include enthalpic stretching of the filament backbone [285] was used to explain this high extensibility of intermediate filament networks in the nonlinear mechanical response [180]. It still remains unclear, however, how various levels of organization of supramolecular filaments contribute individually to the overall nonlinear mechanics of those biopolymer networks.

The structural hierarchy of biopolymer filaments ensures high network functionality and the presence of multiple structural levels decreases the probability of catastrophic failure. Mutations in the basic structural units, however, cause defects in polymer assembly and can lead to pathological conditions [46]. Most human diseases related to mutations in IFs family and ECM proteins result from formation of filaments with a distorted internal architecture. Changes in intermolecular adhesion generally reduce network resilience and cause premature network failure by breaking, for example, hydrogen bonds that are crucial to defining the structure of the protein building blocks. These changes at the molecular level destabilize the whole filament structure, making fibrillar packing less regular and possibly causing protein unfolding, sliding of molecules against each other, or breaking of crosslink bonds much earlier than anticipated by Nature.

In some cases, structural defects can also enhance internal order. The highly ordered hierarchical structure of amyloid plaques, for instance, results in robust structures in which the dissipation of mechanical stresses is prevented. A full understanding of the contribution of the hierarchical structure to the mechanical stability of biopolymers and their nonlinear network mechanics is therefore crucial for future treatment strategies to remedy or even prevent disease states.

1.5 SCOPE OF THIS THESIS

The goal of this thesis is to elucidate the role of the supramolecular, internal architecture of protein filaments that build the cytoskeleton and extracellular matrix in the macroscopic nonlinear elasticity of the networks they form. This high nonlinear elastic response to external forces is thought to help protect cells and tissues from mechanical damage. To this end, we combine macroscopic rheology to characterize the nonlinear elasticity with imaging and scattering techniques to characterize the morphology and supramolecular structure of different biopolymer filaments. The experimental approach is described in **Chapter 2**.

In **Chapter 3**, we study the nonlinear elasticity of the major blood-clotting protein fibrin in relation to its supramolecular architecture. We show that in the limit of so-called “*coarse fibrin clots*”, which are composed of fibers that are thick bundles of thin, semiflexible protofibrils, fibrin clots exhibit a strong strain-stiffening response to an applied steady stress, with a complex dependence on stress. We can account for this response in terms of a loose semiflexible bundle model, where small stress causes entropic stretching of the fibrin bundles, moderate stress leads to filament backbone stretching, and large stress causes entropic stretching of flexible domains inside the fibers. These consecutive stretching processes under increasing levels of load ensure a high resistance of fibrin clots to large deformations.

In **Chapter 4**, we investigate the influence of bundle size on the nonlinear elasticity of fibrin clots. We characterize the nonlinear elasticity in the limit of so-called “*fine fibrin clots*”, which are composed of thin bundles of only 3 protofibrils. Similar to *coarse gels*, the *fine clots* also show a dramatic stress-stiffening response with a complex functional dependence on stress. In analogy to the *coarse clots* in Chapter 3, we can describe the nonlinear response by an affine entropic model if we include backbone extension and shear-induced alignment of the protofibrils. We show that the persistence length and stretch modulus of the protofibrils are fully consistent with the same parameters deduced from the rheology of *coarse clots*. Therefore, Chapters 3 and 4 together strongly support an affine entropic model for fibrin rheology, independent of bundle size.

In **Chapter 5**, we provide a complementary analysis of the nonlinear elasticity of *coarse fibrin clots* based on large amplitude oscillatory shear (LAOS). We show that the strain response to an imposed sinusoidal stress is highly non-sinusoidal, indicating strong nonlinearity. We quantify the departure from linearity by various methods, including Fourier Transform analysis and Lissajous plots. We find that these methods have comparable sensitivity to the onset of stress-stiffening as measurements of the differential modulus that we used to probe the nonlinear behavior of fibrin networks in Chapter 3 and 4.

In **Chapter 6**, we shift the focus to the rheology of a different type of extracellular matrix protein, namely collagen. In most tissues, collagen fibers consist predominantly of collagen type I, which forms heterotypic fibrils with another collagen, namely type V. This co-assembly is thought to provide a mechanism for diameter regulation. We show that increasing levels of collagen V strongly reduce the stiffness of hybrid collagen networks compared to homotypic

collagen I gels. It is, however, difficult to quantitatively interpret the influence of collagen V content on the mechanics of heterotypic collagen networks, since the network appears to deform in a nonaffine manner. There is not yet an analytical theory available to give quantitative predictions of the elastic modulus in this regime. We tentatively ascribe the influence of collagen V to changes in the interaction among tropocollagen molecules within or between fibers. Our results suggest that collagen composition can be used as an alternative control parameter to design collagen-based biomaterials.

In **Chapter 7**, we turn to cytoskeletal biopolymer networks. We implement a new *in vitro* model system that helps pave the way for future systematic studies of the influence of interactions between different filament types on composite network mechanics. *In vivo*, all three of the cytoskeletal filaments, actin microfilaments, microtubules (MTs) and intermediate filaments (IFs), are known to colocalize and strongly interact with each other. *In vitro* studies of composite actin-IF or actin-MT networks indicate that the disparate bending rigidities of the filaments and interactions between them can lead to surprising non-additive effects on network elasticity. We set up for the first time a composite network of MT and vimentin (a member of the IF family that is present in all mesenchymal cells) and identify buffer conditions that allow for simultaneous assembly of both proteins. Rheological data show that the stiffness and nonlinear response of this composite system are intermediate between those of the pure components.

Finally, in **Chapter 8**, we describe a new shear cell device that can be used to visualize changes in the microstructure of biopolymer networks under large shear by confocal microscopy. This device permits application of large oscillatory and steady shear strains while simultaneously imaging the sample through the glass bottom plate. The device can be used to quantify nonaffinity in the strain field by tracking fiducial markers such as probe beads embedded inside the network, or to directly observe fiber bending and stretching or network rupture at large stress. Such measurements are critical to obtain a full understanding of the influence of the multiscale structure of biopolymer networks on their remarkable nonlinear elasticity.

2 MEASUREMENT TECHNIQUES

T HIS chapter describes the main techniques used for experiments throughout this thesis. The microstructure of biopolymer networks was characterized with the use of confocal fluorescence microscopy. Individual filaments were imaged by atomic force microscopy and electron microscopy. Turbidimetry measurements were performed to probe the diameter and mass/length ratio of filaments in their native, hydrated state. Finally, macrorheology and microrheology were used to probe the mechanical properties of the networks.

2.1 STRUCTURAL CHARACTERIZATION

2.1.1 NETWORK CHARACTERIZATION BY CONFOCAL MICROSCOPY

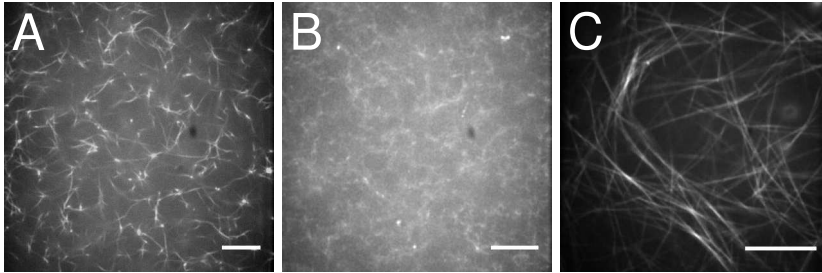


FIGURE 2.1. Confocal microscopy images of fluorescently labeled networks of (A) fibrin fibers, (B) collagen fibers and (C) microtubules, each prepared at a protein concentration of 1 mg/ml. Images represent single plane. Scale bars, 10 μm .

The various biopolymer networks studied throughout this thesis were labeled with the fluorescent dye Alexa488 (fibrin), Oregon Green (collagen) and Rhodamine (microtubules). Networks were imaged with a spinning disc confocal microscope (Leica Microsystems, Rijswijk, Netherlands) using a 488 nm laser (Sapphire 488-30 CHRH, Coherent Inc., Utrecht, Netherlands) or a 561 nm laser (85-YCA-015, Melles Griot) for illumination and a back-illuminated cooled EMCCD camera (C9100, Hamamatsu Photonics, Herrsching am Ammersee, Germany) for detection (Fig. 2.1). Three-dimensional (3D) image stacks were obtained by scanning through the z -direction in steps of 0.1 μm over a range of 10 μm with a piezo-driven 100x/1.3 NA oil immersion objective. Maximum intensity projections were made with ImageJ (<http://rsbweb.nih.gov/ij/>).

An estimate of the characteristic spacing between filaments (or pore size, ξ) was obtained by image analysis software in MatLab 7.1 (kindly provided by P.M. Bendix) [20]. Confocal images were band-pass filtered and maximum intensity projections of 101 planes separated by 0.1 μm steps were made with ImageJ. Binary images were obtained by thresholding maximum intensity projections with a threshold equal to the average pixel intensity plus one standard deviation [156]. Pixels with intensity above threshold were considered to be part of fibers. The distance between these pixels within each row and column was taken as ξ . The distribution between pixels in the X and Y directions was fitted well to an exponential, $P = P_0 e^{-\xi/\xi_c}$ with P_0 and the decay length ξ_c as fitting parameters, indicating that the networks were isotropic.

2.1.2 FILAMENT CHARACTERIZATION BY ELECTRON AND ATOMIC FORCE MICROSCOPY

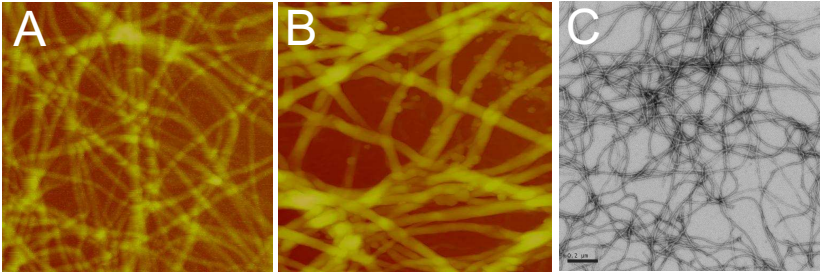


FIGURE 2.2. High-resolution images of various protein biopolymers. (A) AFM image of dried 0.2 mg/ml fibrin fibers. Area, $5 \times 5 \mu\text{m}$. (B) AFM image of dried 2 mg/ml collagen fibrils. Area, $3 \times 3 \mu\text{m}$. (C) EM image of 0.14 mg/ml vimentin filaments. Scale bar, $0.2 \mu\text{m}$.

Atomic Force Microscopy (AFM) images of filaments in a dried state (Fig. 2.2 A, B) were obtained in tapping mode with a Dimension V Scanning Probe Microscope (Veeco, Plainview, NY) using a silicon triangle cantilever with 15-30 kHz resonance frequency and 0.01-0.50 N/m nominal spring constant (Veeco). Fibrin and collagen gels were polymerized on mica surfaces in a moist 37°C atmosphere. Since the resulting gels were too dense to allow imaging by AFM, we removed excess material just before imaging by peeling the top of the gel off with filter paper. In this way, only filaments stuck to the mica were exposed and the filament density was sufficiently low to distinguish individual filaments by AFM. The samples were finally dried with nitrogen before imaging. The fibril diameter was analyzed in Nanoscope 6.14r1 software (Veeco) from the height, averaging over 20-30 fibrils per experimental condition. We compared the height with the width (determined from Gaussian fits to line profiles across each fibril), and found that the height was typically 3-5 times larger than the width for both fibrin and collagen filaments. This discrepancy is probably caused in part by a profile broadening effect due to tip-sample convolution. In addition, drying of the fibrils, that typically contain at least 50% water, may cause collapse and a reduction in height.

In order to visualize filaments in their hydrated state, an AFM fluid cell (Veeco) equipped with a tip with 2 nm radius and 0.12 N/m nominal spring constant was used. Samples were polymerized on parafilm in a moist 37°C atmosphere and next deposited on a glass slide coated with Formvar layer by peeling the top of the gel off. Next, the filaments were fixed with 1% glutaraldehyde solution (GA) and placed under the scanning probe of the microscope. 1-fold polymerization buffer was pipetted on top of the sample to keep filaments in a hydrated state. Images were taken in contact mode.

Vimentin filaments (Fig. 2.2 C) were imaged by electron microscopy (EM, Carl Zeiss, Oberkochen, Germany). Samples were polymerized at 22°C followed

by fixation with 1% glutaraldehyde on a glow-discharged, carbon-coated copper electron microscopy grid (Cu Copper grids, 300 mesh, SPI, Germany). The filaments were allowed to bind to the support surface for 15 seconds. The sample was then washed with distilled water and stained for 15 seconds with 2% uranyl acetate dissolved in water. The staining solution was removed by washing the sample with distilled water and the grid was dried in air.

2.1.3 FILAMENT CHARACTERIZATION BY TURBIDIMETRY

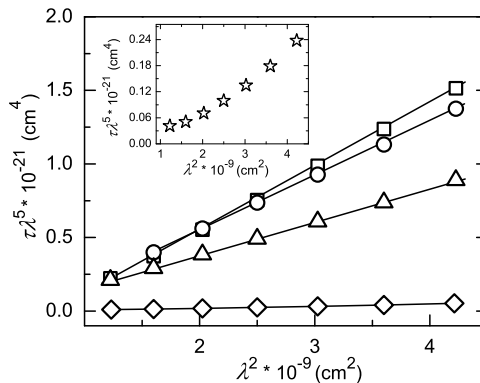


FIGURE 2.3. Wavelength dependent turbidity of 2 mg/ml collagen I networks (circles), mixed 80/20 collagen I/V networks (triangles), fibrin coarse clots (squares) and fine clots (diamonds). The data are scaled according to the theoretical prediction in Eq. (2.3) for long (>800 nm) rod-like polymers with a diameter below 200 nm. Pure networks of collagen V (stars, inset figure) do not follow the predicted relation, presumably because the filaments have a typical length of only ~ 1 μm .

The diameter of filaments in their native, hydrated state was determined using turbidimetry. Data were analyzed according to a theoretical model of Yeromonahos et al. [327], which is a corrected version of an earlier model of Carr and Hermans [52] for gels composed of rigid rod-like polymers. Gels were polymerized in 1 cm-path length cuvettes (UV-Cuvette micro, Plastibrand, Germany) and fibril diameters, d , and mass-length ratios, μ , were obtained by measuring the light transmission through the samples over a range of incident wavelengths, λ , between 350-650 nm with a UV1 Spectrophotometer (Thermo Optek). The transmitted light intensity, I_t , is lower than the incident intensity, I_0 , due to light scattering by the turbid gels. The optical density, D , of the solution is defined as [157]:

$$\frac{I_t}{I_0} = 10^{-D.L} \quad (2.1)$$

and the turbidity, τ , is:

$$\tau = D \cdot \ln 10, \quad (2.2)$$

where L is the path length in cm and D is in units of cm^{-1} . For a solution of randomly oriented fibers that are long (>800 nm) and thin compared to λ (<200 nm diameter), the turbidity is [327]:

$$\tau\lambda^5 = A\mu(\lambda^2 - Ba^2), \quad (2.3)$$

where $A=(88/15)c\pi^3n_s(dn/dc)^2(1/N_A)$ and $B=(368/462)\pi^2n_s^2$. In these equations, N_A is Avogadro's number, n_s is the refractive index of the solvent ($n=1.33$ for water), dn/dc is the specific refractive index increment ($dn/dc=0.186$ cm^3g^{-1} for collagen [42] and 0.17594 cm^3g^{-1} for fibrin [327]), and c is the protein concentration expressed in g/ml [327]. Plots of $\tau\lambda^5$ versus λ^2 should give straight lines whose slope ($=A\mu$) yields the mass/length ratio and whose intercept with the y-axis ($=-A\mu Ba^2$) gives the square of the average radius, a (Fig. 2.3). Data for fibrin networks and collagen networks of varying concentration could all be fit well by straight lines. Only pure networks of collagen V did not follow the expected scaling. This was probably due to the shorter length of collagen V fibers (on average 1 μm) compared to collagen I and fibrin fibers, which places these filaments right on the edge of the validity of the light scattering model.

2.2 MECHANICAL MEASUREMENTS

2.2.1 MACROSCOPIC RHEOMETRY

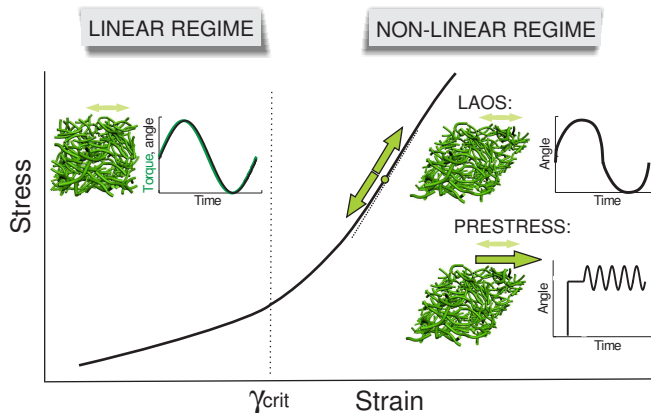


FIGURE 2.4. Schematic representation of linear and nonlinear rheology of a strain-stiffening network probed by LAOS and prestress measurements.

Rheology was performed with a stress-controlled rheometer (Physica MCR 501, Anton Paar, Graz, Austria) equipped with a steel cone top plate

(dimensions are specified in each chapter) and flat bottom plate (50 mm diameter). The bottom plate temperature was controlled using a Peltier element. Samples were polymerized between the rheometer plates, in combination with wet tissues or mineral oil applied to the sample edge, and a hood surrounding the geometry was used to maintain a moist atmosphere. Network polymerization was monitored by measuring the increase in the shear moduli with an oscillating shear at a frequency, ω , of 3 rad/s and small strain amplitude, γ , of 0.5%. We verified that this strain amplitude was small enough not to perturb network polymerization. The ratio of the stress response, $\sigma(\omega)$, to the applied strain equals the complex shear modulus, $G^*(\omega) = G'(\omega) + iG''(\omega)$. The elastic modulus, $G'(\omega)$, represents the in-phase (storage) response, while the viscous modulus, $G''(\omega)$, represents the out-of-phase (loss) response. When the elastic modulus reached a constant value, the linear viscoelastic moduli were measured as a function of frequency between 30-0.03 rad/s at a small strain amplitude of 0.5%. The non-linear moduli were measured by applying a large amplitude oscillatory shear (LAOS) with $\omega = 3$ rad/s and σ (*stress-control mode*) or γ (*strain-control mode*) increasing logarithmically until sample yielding. To characterize the onset of nonlinearity, the *critical strain*, γ_{crit} , or *critical stress*, σ_{crit} (for strain-stiffening samples) and *yield strain*, γ_{yield} , or *yield stress*, σ_{yield} (for strain-weakening samples) were defined as the value where σ differs from the product $G_0\gamma$ by more than 10%, where G_0 is the linear elastic modulus [294]. LAOS stress-strain data collected by the rheometer software were analyzed in the form of Lissajous plots and Fourier Transform spectra (see Chapter 5).

For fibrin gels, LAOS measurements were complemented with prestress measurements. The differential moduli, K' and K'' , were measured as a function of applied prestress [94, 39, 265]. Samples were pre-stressed with a steady stress σ_0 , and the differential response was measured by superposing a small oscillatory stress, $|\delta\sigma_0| < 0.1 \sigma_0$. This ensures that the measured oscillatory strain response is sinusoidal (Fig. 2.4). The stress-dependent tangent modulus follows from the oscillatory strain response, $K^* = \delta\sigma_0/\delta\gamma_0$. K' was independent of frequency and of the waiting time in the pre-stressed state, demonstrating that the prestress did not cause viscous flow.

2.2.2 OPTICAL TWEEZER MICRORHEOLOGY

To investigate thermal bending fluctuations of fibrin filaments and their rheological consequences *in situ*, optical microrheology was used (Fig. 2.5). Fibrin networks were polymerized in the presence of strongly adherent polystyrene particles with a diameter of 1 μm (Polybead®Polystyrene Microspheres, Polyscience, Inc.). Particles in the gel interior were weakly trapped using a laser with wavelength of 1064 nm [160]. Their thermal position fluctuations were detected by a quadrant photodiode at a sampling rate of 195 kHz.

There are two interpretations of the particle fluctuations inside the network interior. The first interpretation assumes that the bead fluctuations measure the local network rheology. In this case the shear modulus of the gel can be inferred from the particle fluctuations by linear response theory [98]. At high frequencies the shear modulus is controlled by the relaxation of individual polymer chains

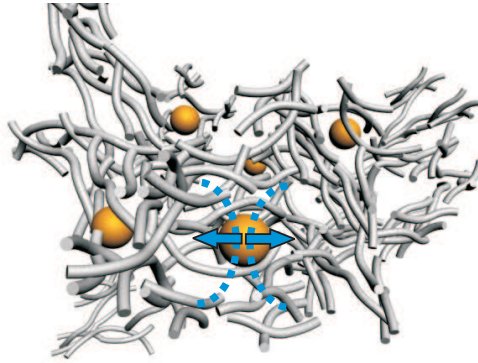


FIGURE 2.5. Schematic representation of beads embedded inside a polymer network. One bead is trapped in a focused laser beam.

[96, 207]. For a semiflexible polymer with a persistence length, l_p , similar to or greater than the contour length, the modulus is given by:

$$G^*(\omega) = \frac{1}{15} \rho \kappa l_p (-2i\zeta/\kappa)^{3/4} \omega^{3/4} - i\omega\eta, \quad (2.4)$$

where ρ is the filament length per volume, $\kappa = l_p k_B T$ is the bending stiffness, $\zeta = 4\pi\eta/\ln(0.6\lambda/d)$ is the lateral drag coefficient and η is the solvent viscosity at 37°C. Using for λ the characteristic mesh size, one can measure the polymer persistence length, l_p .

The second interpretation of the particle fluctuations is that the beads directly report on transverse fluctuations of the fibers to which they adhere. In this case we expect the same qualitative dynamics, with the same 3/4 exponent in either time or frequency dependence [83, 104]:

$$\langle (\Delta h(t))^2 \rangle \simeq 0.082 \left\{ \ln \left[\frac{\kappa \ln(\frac{L}{\pi a}) t}{4\pi\eta a^4} \right] \left(\frac{k_B T}{\kappa} \right)^{1/3} \frac{k_B T}{\eta} t \right\}^{4/3} \quad (2.5)$$

I would like to thank Martijn de Wild (AMOLF) and François Caton (Université de Grenoble, France) for discussion about turbidimetry and for sharing unpublished data; and Christoph Schmidt (University Göttingen, Germany) for hosting us for optical tweezer microrheology experiments.

3 STRUCTURAL HIERARCHY GOVERNS FIBRIN GEL MECHANICS

F *IBRIN* gels are responsible for the mechanical strength of blood clots, which are among the most resilient protein materials in nature. Here we investigated the physical origin of this mechanical behavior by performing rheology measurements on reconstituted fibrin gels. We found that increasing levels of shear strain induce a succession of distinct elastic responses that reflect stretching processes on different length scales. We present a theoretical model that explains these observations in terms of the unique hierarchical architecture of the fibers. The fibers are bundles of semiflexible protofibrils that are loosely connected by flexible linker chains. This architecture makes the fibers 100-fold more flexible to bending than anticipated based on their large diameter. Moreover, in contrast with other biopolymers, fibrin fibers intrinsically stiffen when stretched. The resulting hierarchy of elastic regimes explains the remarkable resilience of fibrin clots against large deformations.

I.K. Piechocka, R.G. Bacabac, M. Potters, F.C. MacKintosh, G.H. Koenderink
Structural hierarchy governs fibrin gel mechanics
Biophysical Journal **98**: 2281-2289 (2010)

3.1 INTRODUCTION

Fibrin is the main structural protein in blood clots, which stop bleeding and serve as scaffolds to promote wound repair [169]. Upon vascular injury, fibrin polymerizes to form a fibrous gel that can withstand the forces exerted by flowing blood and by embedded cells [165, 267]. Fibrin gels are among the most resilient polymer gels in nature [191, 44]. They stiffen strongly when deformed and thereby become increasingly resistant to further deformation [267, 307, 155, 246, 326, 149]. Fibrin clots can survive shear and tensile strains of up to 300% [191, 44]. This remarkable elastic behavior appears to be crucial for the biological function of blood clots. Abnormalities in the structure of fibrin or in its assembly can lead to bleeding or thrombosis, which are both associated with changes in clot mechanics [279]. However, the molecular basis of the extraordinary resilience of fibrin clots is still unresolved [304].

Fibrin clots are composed of fibers which appear stiff and straight when viewed by atomic force microscopy (Fig. 3.1 A). Based on their appearance and on their large diameter (typically 80 nm or more [281]), the fibers are often believed to behave as rigid rods with negligibly small thermal fluctuations [155, 44, 65, 253]. The persistence length, l_p , characterizing the distance over which the fibers are straight is expected to be in the mm-range, assuming that they possess a homogeneous elasticity (see Appendix). Various models indicate that crosslinked networks of rigid fibers should stiffen under shear, because the shear aligns the fibers and thereby causes a transition from a soft elastic regime dominated by fiber bending to a stiffer elastic regime dominated by fiber stretching [224, 67, 133]. While experimental studies indeed show that fibers align when fibrin gels are sheared [155] or stretched [44, 253], there is no evidence that this alignment is the cause of the strain-stiffening behavior of fibrin gels. In fact, there are structural clues that fibrin fibers are unlikely to be homogeneously elastic, as required by the models.

Fibrin fibers are bundles consisting of dozens of protofibrils (Fig. 3.1 B *Middle*), which themselves are composed of two half-staggered strands of fibrin monomers (Fig. 3.1 B *Bottom*) [88, 85]. The monomers in turn consist of three pairs of polypeptide chains, designated $A\alpha$, $B\beta$, and γ , folded into a central E-region and two distal D-region [324]. Fibrin fibers thus have a complex, hierarchical structure. They are furthermore known to contain almost 80% water [51, 112, 298]. This open internal structure may make the fibers more flexible than previously assumed, since the flexibility of a bundle is sensitive to the degree of coupling between the constituent protofibrils. The bundle will only behave as a simple elastic beam if the coupling is tight. The persistence length will then increase quadratically with bundle size N , reaching a few mm for typical values of N (see Appendix). If the protofibrils are not tightly coupled, however, the fibers will be much more flexible than anticipated by the elastic beam limit. In the limit of complete decoupling, the bending stiffness will show a weaker, linear increase with N [61]. Coupling between fibrin protofibrils is normally mediated by long, carboxy-terminal extensions of the $A\alpha$ -chains that protrude from the protofibril surface [102, 64, 187, 306] (Fig. 3.1 B *Bottom*). These chains are mainly unstructured and rather flexible [306, 73], suggesting

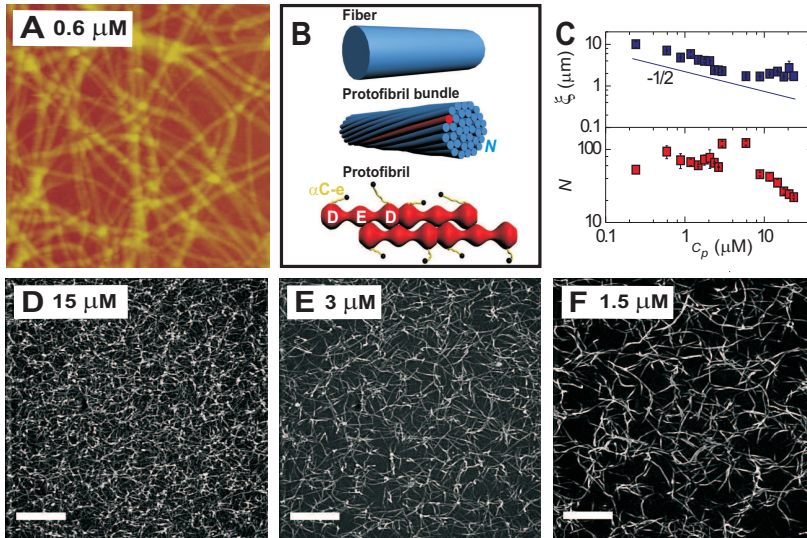


FIGURE 3.1. Structural properties of fibrin gels. (A) Atomic force microscopy shows a homogeneous network of thick and straight fibers ($5 \times 5 \mu\text{m}$ area). (B) Fibrin fibers have a hierarchical architecture: fibers (*Top*) are bundles of protofibrils (*Middle*), which consist of two half-staggered strands of fibrin monomers with $\alpha\text{C-e}$ protruding from the surface (*Bottom*). (C) (*Top panel*) The mesh size of fibrin gels estimated from confocal images decreases as the square root of protein concentration (symbols), consistent with the expectation for homogeneous networks of fibers of constant diameter (solid line). (*Bottom panel*) Concentration dependence of the number of protofibrils per fiber N , measured by turbidimetry. (D-F) Confocal microscopy demonstrates that fibrin gels are homogeneous over a large range of protein concentrations. Scale bars, $10 \mu\text{m}$.

that the protofibrils may be loosely coupled. Based on this structural evidence, we have studied the rheology of fibrin gels with the aim to identify the possible role of this flexibility.

In this chapter we show that the bundle-like structure of fibrin fibers is responsible for the strong strain-stiffening response and exceptional resilience of fibrin gels. We measured the fiber persistence length by optical tweezer microrheology and found that the fibers behave as flexible, loosely coupled bundles of protofibrils. We show that fibrin clots stiffen in two distinct stages when sheared, first by stretching out of fiber fluctuations between network crosslinks followed by stiffening of the fibers themselves. This intrinsic fiber nonlinearity makes fibrin gels unique among biopolymer networks, in which nonlinearities are commonly associated with network structure [224, 285, 195, 94]. We propose a new model which accounts for network and fiber nonlinearities and explains the elasticity of fibrin clots over the entire range of strains.

3.2 SAMPLE PREPARATION

Human fibrinogen and α -thrombin were obtained from Enzyme Research Laboratories (Swansea, UK). All other chemicals were purchased from Sigma-Aldrich (Zwijndrecht, NL). Fibrinogen solutions were made in a fibrinogen buffer of pH 7.4 containing 20 mM Hepes, 150 mM NaCl and 5 mM CaCl_2 . Networks of fibrinogen with concentration ranging from 0.1-8 mg/ml were formed by mixing at room temperature fibrinogen from a stock solution with a 10-fold concentrated fibrinogen buffer, calcium chloride to a final concentration of 5 mM Ca^{2+} and water. To initialize polymerization, thrombin with a final concentration of 0.5 U/ml was added. Thrombin cleaves off two fibrinopeptides (A and B) from the central domain of the fibrinogen molecule. This triggers polymerization, since the exposed sites bind to complementary sites in the distal end domains of the fibrinogen molecule. Initially, the fibrinogen molecules assemble into double-stranded protofibrils held together by noncovalent interactions. Next protofibrils twist around each other and laterally aggregate to form thicker fibrils. The resulting gels are commonly devoted in the fibrin literature as *coarse clots*. In the presence of calcium ions, thrombin also activates the enzyme factor XIII (FXIII), which introduces covalent bonds between fibrin monomers within and between protofibrils. We used a constant molar ratio between the fibrinogen and factor XIII concentration, since FXIII was present in our fibrinogen stock. We checked by gel electrophoresis that after polymerization γ monomers were fully converted to γ -dimers, and α monomers were fully converted to α -polymers (see Chapter 4, Fig. 4.3). Consistent with this observation, we did not find (within experimental error) any further increase of the elasticity when we added up to 150 U/ml extra FXIII. This evidence suggests that the fibrin gels are maximally crosslinked.

For confocal microscopy, Alexa488-labeled fibrinogen (Invitrogen, Breda, NL) was mixed with unlabeled fibrinogen in a molar ratio of 1:4. Samples were polymerized in a sealed glass microchamber for 4 hours at 37 °C and imaged as described in Chapter 2.

3.3 RESULTS AND DISCUSSION

3.3.1 NETWORK STRUCTURE AND SINGLE FIBER MECHANICS

We assembled fibrin gels from purified human fibrinogen under near physiological conditions. The gels were enzymatically crosslinked by fibrinolygase (FXIIIa), which provides molecular bonds both within and between fibers [213, 95]. Addition of thrombin to a solution of fibrinogen causes spontaneous polymerization into thick, straight fibers with average diameters of 120 nm (Fig. 3.1 A). The networks are homogeneous and isotropic over a wide range of fibrinogen concentrations, as revealed by fluorescence microscopy (Fig. 3.1 D-F). The mean distance between filaments progressively decreases as the fibrinogen concentration is raised. The average mesh size, ξ , decreases with the square root of fibrinogen concentration, c_p (Fig. 3.1 C *Top*), as expected for homogeneous networks of fibers with a constant diameter.

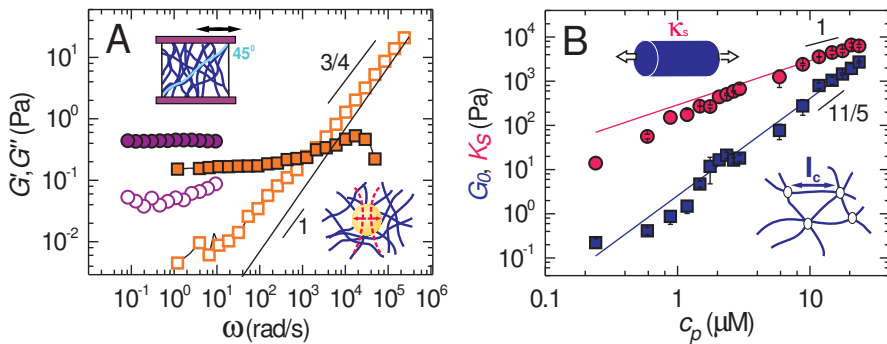


FIGURE 3.2. Low-strain rheology of fibrin gels. (A) Frequency dependence of the elastic (solid symbols) and viscous (open symbols) moduli for a network of $0.6 \mu\text{M}$ fibrin, measured by rheometry (circles) and microrheology (squares). Solid line shows the viscous modulus of the solvent. (*Upper inset*) The bulk rheology is measured by applying a small, oscillatory shear stress to a fibrin gel between two plates of a rheometer. (*Bottom inset*) The local rheology is measured by microrheology: a probe sphere inside the fibrin gel is held by an optical tweezer (dotted red lines). Its thermal fluctuations are tracked with a quadrant photodiode and converted to shear moduli using linear response theory. (B) The low-strain plateau modulus G_0 (blue squares) agrees with an entropic model of semiflexible fibers (blue line) with one adjustable parameter, the distance l_c between crosslinks (*Bottom inset*). The high-strain plateau modulus K_s (red circles) agrees with a single-fiber stretching model (red line) with one adjustable parameter, the fiber stretch modulus κ_s (*Upper inset*).

We first investigated whether the fibers within the gels exhibit any thermal bending fluctuations. This was investigated using optical tweezer microrheology as described in Chapter 2. Fibrin gels are viscoelastic materials, which store deformation energy, as quantified by the elastic modulus G' , but also dissipate energy, as quantified by the viscous modulus G'' . At frequencies below 1000 rad/s , G' is larger than G'' (Fig. 3.2 A), indicating that fibrin gels are predominantly elastic. However, at frequencies above 1000 rad/s , G'' dominates the response. The shear modulus at these high frequencies reflects the stress response of single filaments. G'' increases as a power-law in frequency with an exponent of 0.8 ± 0.01 . This exponent is consistent with the $\omega^{3/4}$ -scaling predicted for semiflexible polymers [96, 207, 160, 314] whereas it differs substantially from the linear scaling expected for stiff polymers. The data therefore strongly suggest that the fibers exhibit thermal bending fluctuations.

The persistence length of the fibers can in principle be calculated from the amplitude of the particle fluctuations in the high-frequency regime. The microrheology analysis used to compute G' and G'' assumes that the beads measure the bulk viscoelastic modulus. The amplitude of G'' then suggests a fiber persistence length of $60 \mu\text{m}$ as explained in the Appendix. However, since the probe particles are similar in size to the mesh size, it is not obvious that they

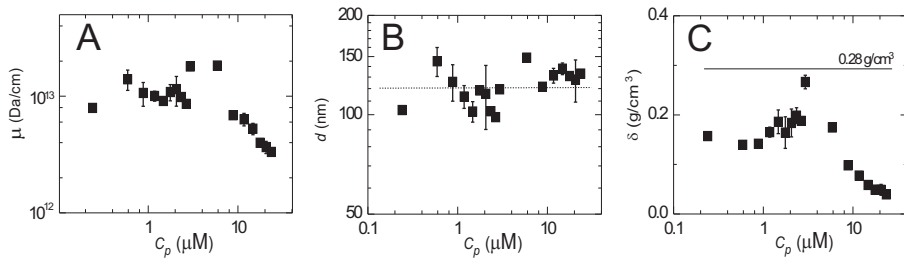


FIGURE 3.3. Turbidity measurements on fibrin gels. (A) Mass/length ratio is independent of fibrinogen concentration up to 10 μM and decreases afterwards. (B) Corresponding concentration dependence of fiber diameter. (C) The protein mass density within the fibers remains constant and low (symbols), at about 0.18 g/cm^3 .

measure bulk rheology. Because they adhere to the fibers, it is possible that the bead fluctuations instead directly reflect transverse fluctuations of the fibers. These fluctuations are characterized by the same $3/4$ exponent in either time or frequency as G'' [104]. Within this framework, the amplitude of the bead fluctuations we observe are consistent with a persistence length of 20 μm . We believe, however, that our microrheology measurements measure network rheology rather than fiber fluctuations. Such fiber fluctuations would be expected to be anisotropic, contrary to our observations. Moreover, the apparent elastic modulus measured by microrheology is close to the bulk modulus. In any case, our measurements clearly indicate the presence of significant thermal bending fluctuations, and both interpretations are consistent with a persistence length of the order of tens of μm . This is 100-fold less than the mm-sized persistence length expected for homogeneous fibers (see Appendix).

We hypothesized that this discrepancy is due to the bundle-like architecture of the fibers. The effective persistence length of a bundle of N protofibrils is sensitive to the compliance of the crosslinks between protofibrils, especially for large N [61]. To assess the bundle size *in situ*, we performed turbidimetry on fibrin gels. This technique probes the fibers in their native, hydrated state, in contrast to AFM. Both the mass/length ratio and the diameter of the fibers can be calculated from the wavelength dependence of the turbidity as described in Chapter 2. The mass/length ratio was $1.2 \cdot 10^{13}$ Da/cm and independent of fibrin concentration up to 10 μM (Fig. 3.3 A). Since protofibrils have a mass/length ratio of $1 \cdot 10^{11}$ Da/cm [88], the fibers contain on average 87 protofibrils (Fig. 3.1 C *Bottom*). This implies an expected fiber persistence length of 3.8 mm in case of tightly bound protofibrils and 44 μm in case of flexibly bound protofibrils. The latter value agrees well with the microrheology data. In support of the idea that the protofibrils may be loosely coupled, we note that according to turbidimetry the bundles are very open structures, with a diameter close to 120 nm (Fig. 3.3 B) and protein density of only 0.18 g/cm^3 up to 10 μM (Fig. 3.3 C).

3.3.2 LOW-STRAIN MECHANICS OF FIBRIN GELS

Microrheology provides measurements of the local gel rheology on the scale of the probe particle size. For probe particles that are similar in size to the mesh size, as is the case here, the local rheology usually differs somewhat from the bulk rheology [98]. To obtain more quantitative measurements of the low- frequency

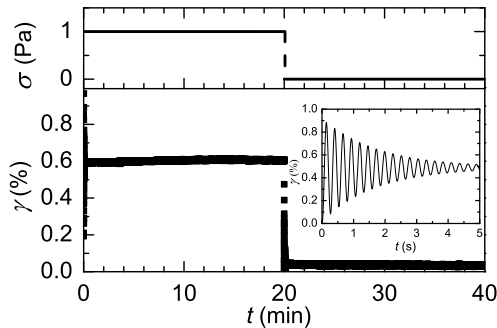


FIGURE 3.4. Time dependence of shear strain (*Bottom*) after imposition and subsequent removal of a steady shear stress (*Top*) for a network of $6 \mu\text{M}$ fibrin. After imposition of a constant stress, the fibrin network shows a very fast strain response with no subsequent creep. This characteristic solid-like behavior was observed for all fibrin networks. When the stress is released, an immediate and nearly complete recovery of the strain takes place. This suggests that the sample is predominantly elastic. At the beginning of a creep test, the strain response has a superposed damped oscillation (*Inset*). This inertio-elastic oscillation is characteristic for highly elastic materials [326, 15, 80].

rheology, we performed rheometry using a rotational rheometer with cone-and-plate geometry (top plate: 40 mm diameter, 1 degree angle, $49 \mu\text{m}$ truncation) as described in Chapter 2. Drying was prevented by coating the sample edge with mineral oil and maintaining a moist atmosphere. Consistent with microrheology, rheometry shows that the fibrin gels are predominantly elastic at low frequency (squares in Fig. 3.2 A). G' is independent of frequency and at least 100-fold larger than G'' . This indicates that the fibrin gels behave as near-perfect elastic solids. The networks remain solid-like even when subjected to a shear stress for 20 minutes (Fig. 3.4), indicating negligible sliding of protofibrils within fibrils or junctions between fibers [213, 95].

The concentration dependence of the low-frequency elasticity provides another way to distinguish between models of semiflexible and rodlike polymers. The elastic modulus in the elastic plateau region, G_0 , increases by 4 orders of magnitude, from 0.1 to 2000 Pa, when the protein concentration is raised 100-fold, from 0.2 to $24 \mu\text{M}$ (squares in Fig. 3.2 B). The increase follows a power-law in concentration with an exponent of 2.3, similar to other reports [213, 95, 270, 91]. This scaling agrees well with the $c^{11/5}$ -scaling predicted (and

observed) for semiflexible polymers such as actin, where the elasticity is dominated by entropic stretching of the thermally bent polymers [195, 94]. In contrast, a smaller exponent of 2 is expected for rodlike polymers that bend when the network is sheared [262, 166]. Since the difference between these exponents is rather small, we also tested more quantitatively whether the fibers behave as semiflexible polymers by comparing the data with a theoretical model [195]. The modulus for a densely crosslinked network of semiflexible polymers that strains uniformly is $G_0 = 6\rho k_B T l_p^2 / l_c^3$, where ρ is the total fiber length per volume, k_B is Boltzmann's constant, and T is absolute temperature. We can calculate ρ from the measured fiber mass/length ratio and the molar concentration of fibrin. The mesh size $\xi = (1/\rho)^{1/2}$, calculated from ρ , is consistent with the measured mesh size (Fig. 3.1 C *Top*). The crosslink distance, l_c , is proportional to the distance between filament entanglements, $l_e \sim l_p^{1/5} \rho^{-2/5}$ [195, 94]. Assuming that the fibers are loose protofibril bundles with $l_p = 44 \mu\text{m}$, we find excellent agreement of the experimental data with the entropic model over the entire range of polymer concentrations (blue line in Fig. 3.2 B). We used only a single free parameter, namely the prefactor between l_c and l_e . We found a best-fit value of 0.35, and values of l_c close to ξ . This indicates that the gels are densely crosslinked, consistent with their branched structure [304].

If the fibrin fibers are semiflexible, the network elasticity should remain linear until the shear straightens out the thermal slack of polymer segments between crosslinks [195, 94]. The critical strain, γ_c , where nonlinearity sets in should thus decrease with increasing polymer concentration. In contrast, γ_c will increase with concentration for rodlike polymers, since nonlinearity will set in when the shear aligns the polymers and buckles polymer segments between crosslinks [67]. One can therefore distinguish between rodlike versus semiflexible polymer behavior by measuring the concentration dependence of γ_c . We subjected the fibrin gels to a steady prestress σ_0 , and measured the tangent modulus K' by superposing a small oscillatory stress as described in Chapter 2. K' always increases strongly above a critical stress σ_c (Fig. 3.5 *Bottom*). The corresponding critical strain decreases with increasing polymer concentration, consistent with the entropic model and contrary to the model of rodlike polymers (squares in Fig. 3.6 A). Again, we can make this test more quantitative by comparing the data with the entropic model, which predicts $\gamma_c = l_c/3l_p$ [195]. The concentration dependence of γ_c agrees well with the predicted $c_p^{2/5}$ -scaling (line in Fig. 3.6 A). The values of γ_c are a factor 4 lower than the predicted values (using the same assumptions for l_c and l_p as before). Similarly, there is a 4-fold difference between the calculated and measured critical stress (Fig. 3.6 B). The small numerical discrepancy with the data suggests that strain-stiffening is postponed by a slight degree of nonaffine bending or rotation of filaments [144, 40]. Still, the agreement is rather good, thus providing independent evidence that the fibrin fibers are loose protofibril bundles.

The persistence length compatible with the rheology data is internally consistent with that obtained by laser tweezer microrheology. However, the value of 40-60 μm is smaller than values reported previously. A recent study using tweezers to actively bend fibrin fibers within a clot reported a Young's modulus of 14.5 MPa for ligated fibrin fibers with a diameter of 270 nm, suggesting

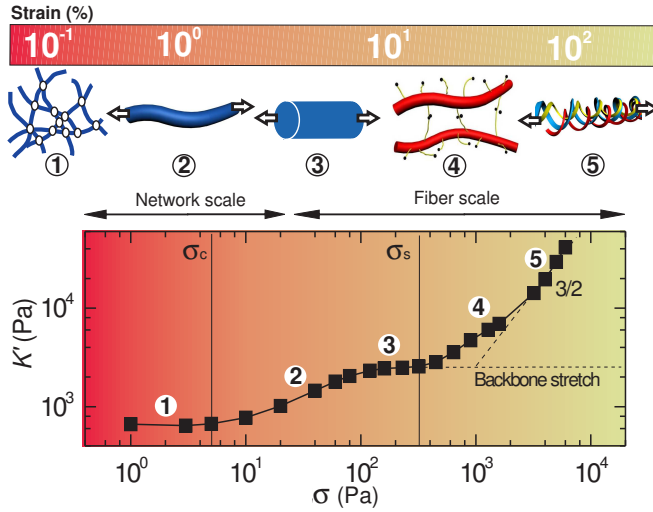


FIGURE 3.5. High-strain mechanics of fibrin gels. (*Top*) Increasing levels of shear strain (bar) induce a sequence of distinct elastic regimes. (*Bottom*) Typical stress-stiffening behavior of a fibrin gel ($9 \mu\text{M}$). The color coding of the background indicates the transition from a regime dominated by entropic elasticity at the network level (red) to a regime dominated by entropic elasticity at the fiber level (green). The initial, linear network stiffness reflects thermal fluctuations of the fibers (regime 1). Strains of a few % pull out the thermal slack from fiber segments between crosslinks, leading to network stiffening (regime 2). Even larger strains cause fiber stretching, resulting in a second linear regime (regime 3). The elastic modulus would remain constant for fibers with a linear stretch modulus (dashed line). Instead, the modulus increases again (regime 4), indicating stretching of flexible regions within the fibers. The increase is consistent with the $\sigma^{3/2}$ response expected for wormlike chains (dashed line). Forced-unfolding of fibrin monomers may start before network rupture (regime 5).

that l_p was around 1 m [65]. Two other studies tracking thermally induced transverse fiber fluctuations within clots using a fast camera [148] and dynamic light scattering [268] reported l_p around 20-40 cm, but the fiber diameter and mass/length ratio were not reported. The latter two studies did find a power-law exponent of $3/4$ for the bending fluctuations characteristic of semiflexible polymer behavior, consistent with our results. There are several factors that make it difficult to make a direct comparison between our study and the previous reports. Firstly, fibrin assembly is known to be highly sensitive to ionic strength, pH, the presence/concentration of certain ions (such as calcium), thrombin concentration, and temperature [259, 281, 219, 154]. Also, the presence of other proteins (likely present in the plasma but not in our reconstituted clots) can affect assembly. The assembly conditions can affect protein packing density, the degree of lateral binding between protofibrils within the fibers and fiber branching. Changes in lateral association between protofibrils can strongly affect fiber persistence length, sliding would for instance tend to lower l_p . Secondly, the

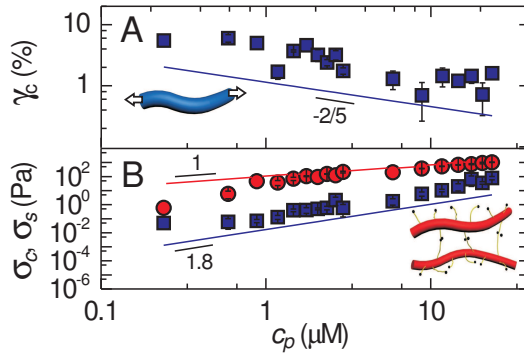


FIGURE 3.6. Strain-stiffening transitions of fibrin gels. (A) Critical strain characterizing the onset of the first strain-stiffening regime (regime 2), compared with a model (line) that assumes entropic stretching of fibers (*Inset*). (B) Critical stress characterizing the onset of the first strain-stiffening regime (regime 2, blue squares) and the onset of the second strain-stiffening regime (regime 4, red circles). Solid lines indicate model predictions for entropic stretching of fibers (blue line) and of loose protofibril bundles (red line and *Inset*).

hierarchical bundle-like structure of fibrin fibers implies that the measured persistence length may depend on the length scale and time scale on which it is probed. Our optical tweezer method probes the fibers on short length and time scales (frequencies of 1-100 kHz), whereas the previous reports probed l_p at lower frequencies of 3 Hz [65], 100 Hz [268], or up to 1k Hz [148]. We conclude that a detailed study of the variation of fiber persistence length with assembly conditions will be needed, using a combination of different techniques (at different spatiotemporal resolutions).

3.3.3 HIGH-STRAIN MECHANICS OF FIBRIN GELS

We next tested whether signatures of a loose bundle structure are present in the rheology of fibrin gels at high strains, where fibers are subject to large tensile forces. The network stiffness exhibits at least four distinct stress regimes (Fig. 3.5 *Bottom*). There is an initial linear regime (*regime 1*), followed by a rise in stiffness (*regime 2*), a second linear regime (*regime 3*), and finally a second stiffening regime (*regime 4*). The network ruptures at a maximum stress σ_{max} , labeled as *regime 5*. The rupture stress is nearly 1000-fold larger than σ_c across the entire concentration range (Fig. 3.7 A). The maximal stiffening relative to G_0 decreases from a factor 300 for the sparsest network to a factor 20 for the densest network (Fig. 3.7 B). Remarkably, the stress-stiffening curves are repeatable during many consecutive stress sweeps, even when the stress is increased almost to the breakage point (Fig. 3.8 A). Moreover, we observe no hysteresis between upward and downward stress sweeps (Fig. 3.8 B).

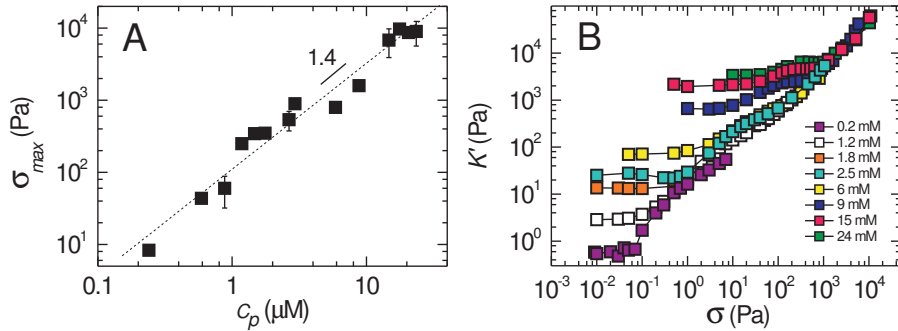


FIGURE 3.7. (A) Concentration dependence of rupture stress. Dashed line indicates power-law fit. (B) Stress-stiffening curves for fibrin networks with concentrations as indicated. The stiffening response becomes weaker with increasing fibrinogen concentration.

While the linear elastic response of the fibrin gels is consistent with an entropic model, the nonlinear response deviates strongly from this model. The model predicts an increase of elasticity with stress as $\sigma^{3/2}$ [94]. But this is valid only if the polymers are inextensible, whereas fibrin fibers are known to be extensible [191]. To test whether fiber stretching can explain the high-strain response of fibrin gels, we rescaled the stress-stiffening curves for different fibrin concentrations by the density of protofibrils, $N\rho$. Note that this scaling accounts for the changing bundle size above $10 \mu\text{M}$ fibrinogen (Fig. 3.1 C *Bottom*). If the elasticity is governed by single-fiber mechanics, the rescaled data should fall on a single curve. As shown in Fig. 3.9 A, rescaling indeed leads to data collapse onto one curve with a linear regime (*regime 3*) followed by a strain-stiffening regime (*regime 4*). The corresponding plateau modulus K_s (red circles in Fig. 3.2 B) and critical stress σ_s (red circles in Fig. 3.6 B) increase linearly with fiber concentration. Altogether, this suggests that the high-strain gel response is governed by single fiber mechanics, and that the fibers are intrinsically nonlinear in their response to stretch.

The linear stretch modulus of the fibers can be estimated from K_s . For an aligned network of fibers with stretch modulus κ_s , K_s can be approximated as $1/8\rho\kappa_s$ as explained in details in the Appendix. The rheology data are consistent with $\kappa_s = 15 \text{ nN}$ (red line in Fig. 3.2 B). This corresponds to a stretch modulus of 170 pN per protofibril, close to previously reported values of $50\text{--}100 \text{ pN}$ for protofibril gels polymerized from fish fibrinogen [285]. For fibrinogen gels with concentrations below $2 \mu\text{M}$, the data depart from the predicted stiffness. This may be due to a small degree of nonaffinity, but we also note that stress-stiffening curves for dilute gels do not show a pronounced plateau (Fig. 3.7 B). The nonlinear stretching of the fibers can have several origins. One possibility is suggested by the loose bundle structure of the fibers. Let us consider a fibrin bundle as a parallel array of protofibrils that fluctuate indepen-

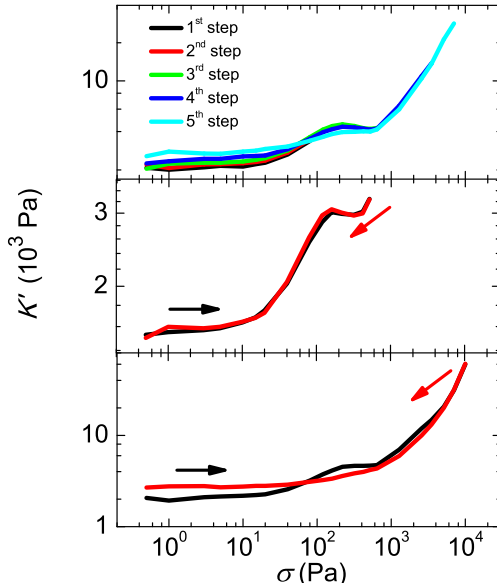


FIGURE 3.8. Repeatability of stress-stiffening curves for 15 μM fibrin network. (A) Stress-stiffening curves were repeatable during many consecutive stress sweeps in the nonlinear regime, even when the stress was brought up almost to the breakage point. Occasionally the stiffness in the linear regime increased after a previous stress sweep. This work-hardening phenomenon is reminiscent of the behavior of actin networks crosslinked by filamin, where it was explained by alignment and bundling of filaments at large strain [189]. (B) The stiffening curves obtained by gradually increasing the applied stress were indistinguishable from curves obtained by gradually decreasing the applied stress. (C) Only when the samples were subjected to strains close to the rupture strain, some hysteresis was observed.

dently over a length l_0 between cross-links to the rest of the fiber. The stretch modulus of this bundle for small extensions will be given by $90k_B T l_p^2 / l_c^3$, where l_p is the protofibril persistence length ($0.5 \mu\text{m}$ [285]). The measured stretch modulus of 170 pN corresponds to $l_0 = 80 \text{ nm}$, meaning that the protofibrils are crosslinked to the rest of the bundle at least at every other αC -chain (given that each fibrinogen monomer has a length of 46 nm). The protofibril bundle should stiffen once the thermal slack of flexible protofibril segments between crosslinks is pulled out. This occurs at a critical force $\tau = \pi^2 k_B T l_p^2 / l_0^2$, which is 3 pN for $l_0 = 80 \text{ nm}$. This number agrees well with the experimental value of about 2.5 pN that can be read off from Fig. 3.9 A.

The predictions of this model, including both the initial network elasticity (*regimes 1* and *2*) and the fiber stretching response (*regimes 3* and *4*) for $l_p = 0.5 \mu\text{m}$ and $l_0 = 0.1 \mu\text{m}$ are shown in Fig. 3.9 B. Curves are shown for four different fibrinogen concentrations between 0.3 (low) and 9 (high) μM . This model accounts well for the distinct elastic regimes observed in our experiments, particularly for dense networks.

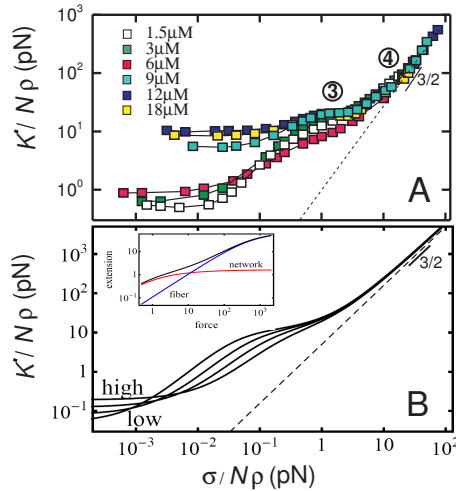


FIGURE 3.9. Intrinsic nonlinear stretch modulus of fibrin fibers. (A) Stress-stiffening curves measured for different polymer concentrations, rescaled by protofibril density. The data collapse onto a mastercurve at large strain, where the network elasticity is governed by stretching of fibers with a nonlinear stretch modulus. The stiffening is consistent with the response of a wormlike chain (dashed line). (B) Stress-stiffening curves predicted for fibrin concentrations of 0.3 (low), 1, 3, and 9 (high) μM . (*Inset*) The fibers are modeled as loose, parallel arrays of protofibrils that fluctuate independently over a length $l_0 = 0.1 \mu\text{m}$ between cross-links to the rest of the fiber. The model combines entropic elasticity of the fibers between *network* cross-links (red line), and intrinsic *fiber* nonlinear stretching due to entropic elasticity of the protofibrils (blue line). The extension (or compliance) of these two contributions add (black line).

The first strain-stiffening transition is dominated by the entropic force-extension relation of the whole fiber (sketched as red line in Fig. 3.9 B *Inset*) due to long wavelength bending fluctuations of the fiber as a whole [195, 47, 87]. In addition to this compliance, we also allow for an extension of the contour length of the fiber [285, 221] (blue line in Fig. 3.9 B *Inset*). These two effects can be thought of as (nonlinear) springs in series and the full extension is the sum of these two contributions, shown by the black line. As noted above, for the extensional response we model the fiber as a loose bundle of protofibrils that act as springs in parallel. The semiflexible nature of the protofibrils leads to a characteristic $3/2$ -scaling of network stiffness with stress [195, 94] (dashed line in Fig. 3.9 B). This is consistent with the experimental data in *regime 4* (dashed line in Fig. 3.9 A). Such entropic stretching is expected to be fully reversible like shown in our experiments (Fig. 3.8).

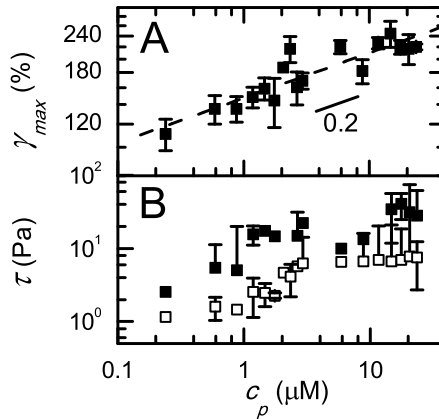


FIGURE 3.10. Rupture behavior of fibrin gels. (A) The rupture strain (symbols) increases weakly with fibrin concentration according to a power-law with exponent 0.2 (dashed line). (B) Tension per protofibril calculated from the shear stress where the second strain-stiffening regime starts (open symbols) and from the stress where the network ruptures (closed symbols).

While the loose bundle model appears to describe the measured gel elasticity well, it requires several assumptions because microscopic parameters such as the crosslink distance, binding affinity, and crosslink compliance are unknown. It is also possible that other flexible regions within the fibers cause the intrinsic fiber nonlinearity. For instance, the α C-regions might elongate under fiber extension. Recent stretching experiments on fibers composed of fibrinogen from different species that differ in the length of their α C-regions showed that the maximum elongation increased with the length of the α C-region [82]. Since these mainly unstructured regions have a small persistence length in the nm-range, stretching should also be characterized by an entropic force-extension relation and $3/2$ -scaling of stiffness with stress. Alternatively, flexible regions may be created by forced-unfolding of fibrin monomers, as suggested by X-ray diffraction studies on fibrin gels under tensile load [12, 44] or by staining of highly stretched gels with a dye specific to β -sheet rich regions [239]. The principal unfolding elements are the coiled-coils connecting the E-region to the distal D-regions, as shown by stretching of single molecules [179, 43] and protofibrils [44, 179]. To test if forced unfolding can explain the observed stress-stiffening behavior, we estimate the force experienced by fibers from the macroscopic shear stress. The average force per fiber at the onset of fiber stiffening is 500 pN, or 1-10 pN per protofibril (open squares in Fig. 3.10 B). This is far less than the average value of 130 pN required to unfold protofibrils (though this number is rate-dependent) [179]. The maximum force per protofibril just before network rupture is 10-40 pN, still less than required for unfolding (solid squares in Fig. 3.10 B). The maximum extensional strain per fiber is around 175% (a little over half of the shear strain in Fig. 3.10 A), which is less than the 300-500% strains reported for

single fibers [191, 82]. The onset of the nonlinear *regime 4*, however, occurs for strains substantially smaller than 100%. Moreover, the reversibility of the stress-stiffening curves is not expected when molecular unfolding occurs [179, 43]. We therefore consider it unlikely that forced unfolding can account for the second strain-stiffening regime. Perhaps unfolding starts at strains close to γ_{max} (*regime 5* in Fig. 3.5). However, the network probably breaks before unfolding is completed. The rupture stress σ_{max} increases more strongly with concentration than the linear increase expected if the network strength is governed by breakage of fibers (Fig. 3.7 A). This indicates that the network strength is limited by the strength of fiber-fiber contacts [183].

Our results indicate that the α C regions play an important role in controlling the extensibility and mechanical resistance of human fibrin clots. Interestingly, while these regions mediate lateral associations between protofibrils in normal clots, they are actually not necessary for lateral association. Fibrin monomers whose α C regions are removed by proteolytic digestion still assemble into striated fibers that form *coarse clots* which are similar in appearance to normal clots but more fragile [102]. There are also several clotting disorders (dysfibrinogenemias) involving mutations or truncations of fibrinogen in the carboxy-terminal region of its α chain (reviewed in [306]), which likely lead to changes in clot mechanics. Indeed, clots of recombinant fibrin with truncated α C regions showed plasticity due to slippage of protofibrils [64]. A true molecular scale understanding of fibrin clot mechanics will require an in-depth study of the role of the α C regions as well as that of other molecular domains mediating lateral association, such as the knob-hole interactions [9, 188] and γ - γ crosslinks [64, 280]. It will be interesting to perform similar nonlinear rheology studies as ours on proteolytically modified fibrin [102], recombinant fibrin with truncated α chains [64], fibrin from other species (differing in length of the α C region [82]), and variant fibrin from human patients with dysfibrinogenemias (such as Caracas II, Marburg, or Dusart) [306]. Based on our findings, we predict that these fibrin clots will be less extensible and more fragile than normal human fibrin clots.

Our study demonstrates that supramolecular assembly is a powerful strategy to build fibrous networks that are incredibly resistant to breakage. Supramolecular assembly is a widely used principle in biopolymers. However, few biopolymers are as extensible as fibrin. An archetypal example of a hierarchical biopolymer is collagen, which provides tensile strength to soft tissues (see Chapter 6). Collagen fibers can withstand large tensile loads but rupture at strains below 50% because the monomers are inextensible and tightly bundled [45]. Cytoplasmic intermediate filaments do match the elasticity and extensibility of fibrin fibers, but these filaments consist of tightly bundled subunits that, similar to fibrin, can unfold upon stretching [163, 12] (see Chapter 7). Fibrin thus has an extra hierarchical level of structure which provides additional mechanical resilience.

3.4 CONCLUSION

The major finding of this work is that the bundle-like structure of fibrin fibers accounts for the remarkable elastic properties of fibrin gels, as summarized in Fig. 3.5. The fibers behave as loosely crosslinked bundles of protofibrils with a built-in stretch-stiffening response. This structure leads to a rich elastic response that reflects stretching of thermal fluctuations of fibers between network crosslinks (*regimes 1 and 2*) followed by stretching of flexible regions within the fibers (*regimes 3 and 4*). From the rheology data alone it is not possible to identify exactly which molecular regions cause the intrinsic nonlinearity of the fibers. The protofibrils themselves are a likely candidate, but the α C-regions or unfolded molecular regions may also contribute. It appears that the clots break before the monomers are fully unfolded (*regime 5*). This is in apparent contrast to a recent study of fibrin gels under tensile load, where gel stiffening was accompanied by molecular unfolding [44]. However, our study addresses a complementary regime of lower strains, enabling us to observe a hierarchy of mechanical regimes that precedes molecular unfolding. We note that there are potentially differences between gel shearing and gel extension. It would therefore be interesting to perform direct measurements of the molecular structure of fibrin monomers in fibrin gels under shear, to prove to what degree molecular unfolding occurs. A promising avenue is to combine mechanical testing with small angle X-ray scattering (SAXS), as was reported for gels under tensile load [44]. Another promising avenues to achieve a molecular level understanding is to perform single fiber stretching experiments at smaller forces than hitherto probed.

Our data reveal molecular design principles that allow blood clots to recover reversibly from large shear forces. This may help to understand how mutations or pathological alterations in fibrin change the resilience of clots, which can cause hemorrhage or thromboembolism [279]. Specifically, our work sheds light on the molecular mechanism by which mutations or truncations of fibrinogen in the carboxy-terminal region of its α -chain lead to dysfibrinogenemias [306]. Moreover, our findings suggest a new design concept for resilient synthetic materials with potential applications in drug delivery and tissue repair [153, 277].

3.5 APPENDIX

3.5.1 CALCULATIONS OF FIBER PERSISTENCE LENGTH BASED ON A BUNDLE MODEL

The persistence length of a fibrin fiber can be estimated in a number of different ways. A coarse-grained approach is to model the fiber as a homogeneous, isotropic cylinder with radius r and Young's modulus E . The persistence length is then given as:

$$l_p = \frac{EI}{k_B T}, \quad (3.1)$$

where $I = \pi r^4/4$ is the moment of inertia and $k_B T$ denotes thermal energy, with k_B the Boltzmann constant and T absolute temperature. The Young's modulus of fibrin has been measured by bending and stretching of individual fibers within fibrin clots using optical tweezers [65]. Using values of E between 2 MPa (unligated fibers) and 15 MPa (ligated fibers), l_p of a fiber with a diameter of 100 nm would be 2-17 mm.

An alternative estimate of l_p can be obtained by taking into account that the fiber is a bundle of N wormlike protofibrils, each having a persistence length l_p^f of 0.5 μm [285, 307]. The effective persistence length of such a bundle depends on the resistance of the crosslinks between the protofibrils to shearing [61, 17]. When the crosslinks strongly resist shear and rigidly glue the protofibrils together (fully coupled regime), the bundle behaves as a homogeneous beam and $l_p = N^2 l_p^f$. On the other hand, when the crosslinks do not resist shear and 'tilt' freely during bundle bending (decoupled bending), the protofibrils bend independently and $l_p = N l_p^f$. Since crosslinks in general have a finite shear stiffness, l_p is expected to eventually crossover from N^2 -scaling to N -scaling with increasing N . The importance of crosslink shearing depends on several molecular parameters, including the axial spacing between crosslinks, the shear stiffness of the crosslinks, and the extensional stiffness of the protofibrils. For a bundle of $N = 87$ protofibrils (as in our experiments), l_p is 44 μm in the fully decoupled limit and 3.8 mm in the fully coupled limit.

3.5.2 CALCULATIONS OF THE PROTOFIBRIL STRETCH MODULUS

For an isotropic network of fibers with stretch modulus κ_s [96, 207]:

$$K_s = \frac{1}{15} \rho \kappa_s, \quad (3.2)$$

Using κ_s as an adjustable parameter, we find good agreement with our data for $\kappa_s = 26$ nN. This corresponds to a stretch modulus of 320 pN per protofibril, which is higher than values of 50-100 pN that were found for protofibril gels polymerized from fish fibrinogen [285]. However, we expect significant filament alignment in the stretch regime, which is not captured by the isotropic approximation. This alignment means that a larger fraction of filaments bears the load imposed by the applied stress. Thus, the actual force per fiber will be lower than the above. For comparison, for a highly aligned network, we can estimate the macroscopic modulus as $1/8 \rho \kappa_s$, based on the following. For a small strain increment $\delta\gamma$, the stress contribution due to a filament oriented with polar angle θ relative to the vertical axis and azimuthal angle ϕ is given by $\delta\sigma = \rho \sin\theta \cos\theta \cos\phi \kappa_s \delta\epsilon$, where the extensional strain of the filament is $\delta\epsilon = \sin\theta \cos\theta \cos\phi \delta\gamma$. Under shear, approximately half of the filaments will experience stretching, while the other half experiences compression. The latter will tend to buckle under shear and will not contribute to the macroscopic stress [224, 133, 67], while diagonal filaments, such as the one indicated in the inset of Fig. 3.2 A, will bear most of the load. Thus, assuming half of the filaments is oriented so as to

stretch and bear the load, we obtain $\delta\sigma \simeq 1/4\rho\kappa_s\delta\epsilon = 1/8\rho\kappa_s\delta\gamma$. This results in $K_s = 1/8\rho\kappa_s$ and a somewhat smaller value for κ_s of about 170 pN, in better agreement with ref. [285].

The theoretical modeling reported in this chapter was done by Fred MacKintosh (Vrije Universiteit, Amsterdam). Further, I would like to thank Paul Bendix (University of Copenhagen) for mesh size analysis software; Gijs Vollenbroek for help with AFM; Chase Broedersz and Enrico Conti (Vrije Universiteit, Amsterdam), Liesbeth Huisman (Universiteit Leiden), Kees Storm (Technische Universiteit, Eindhoven) and Paul Janmey (University of Pennsylvania) for discussions on fibrin mechanics.

4 CONTRIBUTION OF FIBER MICROSTRUCTURE TO FIBRIN NETWORK MECHANICS

SUPRAMOLECULAR assembly is a powerful strategy that is widely used in nature to build fibrous networks with superior mechanical properties. Protein polymers like fibrin fibers have a complex internal architecture that provides remarkable fiber extensibility and contributes to the highly nonlinear elasticity of blood clots. Here we investigated with the aid of rheology the contribution of the internal architecture of fibrin fibers to the mechanics of networks in the limit of so-called “fine clots”. In this regime, fibrin forms thin double-stranded filaments known as protofibrils. We show that increasing levels of shear stress result in a strain-stiffening response with a complex functional dependence on stress. We can quantitatively account for this stiffening using an affine model for crosslinked semiflexible polymers that assumes uniform network deformation. Moderate stresses induce stiffening due to entropic chain stretching, followed by backbone extension, and shear-induced alignment of the protofibrils at higher stresses. These different levels of structural hierarchy render networks of fibrin protofibrils highly resilient, enabling them to withstand large deformations. In addition, these results lend support the loose bundle model proposed in Chapter 3 to account for the nonlinear elasticity of coarse clots, which are composed of thick bundles of protofibrils.

I.K. Piechocka, K. Jansen, C.P. Broedersz, F.C. MacKintosh, G.H. Koenderink
Manuscript in preparation

4.1 INTRODUCTION

Living systems employ supramolecular assembly to build materials with complex architectures and remarkable mechanical properties [5]. The cytoskeleton that structures cells, and the extracellular matrix that structures tissues, are both examples of fibrous materials built of stiff protein polymers. These biopolymer materials are elastic, strain-stiffening, and mechanically resilient [46, 285, 151, 94]. The protein filaments that form the structural backbone of these materials are themselves also supramolecular assemblies made up of protein building blocks. Recent studies of the mechanical properties of protein fibers at the single filament level show rich mechanical behavior that is not captured by continuum elastic models [111]. Fibrin fibers [191, 82] and intermediate filaments [163] can, for instance, be extended by up to 4 times their original length, whereas collagen fibers are rather inextensible, but very tough owing to viscous sliding of subunits within the fiber [45].

In this chapter, we focus on fibrin, which is the main structural protein in blood clots [169]. Even though fibrin fibers in clots have a rather large diameter of around 100 nm, they are still remarkably flexible. This unexpectedly high flexibility can be accounted for by the loose coupling between the constituent protofibrils that build the individual fibers, as demonstrated in Chapter 3. The fibers consist of dozens of protofibrils, which themselves are composed of two half-staggered strands of fibrin monomers connected via flexible α C-regions (Fig. 4.1 A) [111, 88]. This complex hierarchical structure endows fibrin fibers with a built-in stretch-stiffening response that involves entropic stretching of thermal fluctuations of fibers between network crosslinks, followed by entropic stretching of flexible regions within the fibers (see Chapter 3). This can include the protofibrils themselves, but also the disordered and flexible α C-domains [82] or flexible domains caused by forced unfolding [44, 43, 179, 239].

Given the complex internal structure of fibrin fibers, it still remains unclear how the individual protofibrils contribute to the elastic response of fibrin clots, on scales ranging from the fiber to the whole network. To address this puzzle, experiments on the mechanical properties of networks of single (unbundled) protofibrils are crucial. A series of experiments performed in the 1980's showed that the bundle size of fibrin fibers can be varied over a wide range by tuning the polymerization conditions [211, 154]. Fibrin networks are generally prepared in one of two rather different structural limits. Physiological pH and low ionic strength favor *coarse fibrin clots*, made up of fibers that contain tens of protofibrils. This is the limit studied in Chapter 3. In contrast, high pH (8.5) and high ionic strength (0.45) favor *fine fibrin clots* with fibers composed of one or a few protofibrils [85, 149, 211, 95, 247, 13, 213, 254]. Thus, rheology measurements on fibrin networks assembled under different solution conditions may provide critical insights into the effect of filament bundle size on network mechanics.

Here we report rheology experiments on *fine fibrin clots* composed of thin fibers made of three protofibrils, according to turbidimetry. We show that increasing levels of shear stress cause network stiffening with a complex functional dependence on stress. We can quantitatively account for this stiffening using

an affine model for crosslinked semiflexible polymers. The protofibril networks resist large deformations by a combination of entropic stretching, backbone stretching, and alignment of protofibrils in the shear direction. We compare the rheology data with the rheology of *coarse clots* reported in Chapter 3, in order to further examine the validity of the loose bundle model that we propose there.

4.2 SAMPLE PREPARATION

Fibrinogen from Enzyme Research Laboratories in a pH 7.4 buffer of 20 mM sodium citrate was first dialyzed for 2 days at 4 °C against a buffer of pH 8.5 containing 50 mM Tris-HCl and 400 mM NaCl [211, 149, 13]. The dialyzed fibrinogen was centrifuged for 20 minutes at 9000 rpm to remove any aggregated material. The final protein concentration was determined by measuring light absorbance at 280 nm with correction for scattering at 320 nm, using an extinction coefficient of $\epsilon_{280}=1.6 \text{ ml}/(\text{mg cm})$ [13, 215]. The dialyzed fibrinogen stock was frozen in liquid nitrogen and stored at -80°C until use. Assembly of *fine clots* was initiated by addition of 0.5 U/ml thrombin (Enzyme Research Laboratories) in the presence of 3.2 mM Ca^{2+} in dialyzing buffer, after which the sample was quickly transferred to the preheated to 37 °C plates of the rheometer. For fluorescence confocal microscopy, Alexa488-labeled fibrinogen was mixed with unlabeled fibrinogen in a molar ratio of 1:40. Labeled fibrinogen for *fine clots* was dialyzed in the same way as unlabeled fibrinogen. Turbidity measurements on *fine gels* were performed using cuvettes with a path length of 1 cm. All components, except thrombin, were mixed directly in the cuvette, and the mixture was degassed for 5-10 minutes to remove air bubbles. Thrombin was carefully added, and the networks were polymerized for 1 hour at 37 °C taking care to prevent solvent evaporation.

SDS polyacrylamide-gel electrophoresis (SDS-PAGE) analysis for the determination of the crosslinking pattern caused by FXIIIa was performed with 7% polyacrylamide gels. The fibrin samples and a molecular marker (Kaleidoscope, Bio-Rad) were diluted in a 1:1 volume ratio with Laemmli Sample Buffer (Bio-Rad), heated up to 95 °C, and run on gel for 40 minutes at 220V. Protein bands were visualized using GelCode Blue Stain Reagent (Thermo Scientific).

Coarse fibrin clots that were used to compare data with fibrin *fine gels*, were prepared as described in Chapter 3.

4.3 RESULTS AND DISCUSSION

4.3.1 NETWORK AND BUNDLE STRUCTURE

Fibrin networks assembly in a complex manner. In the first step of polymerization process fibrin monomers always first assemble into double-stranded protofibrils that are held together by noncovalent interactions. This initial assembly process is triggered by the enzyme thrombin, which cleaves off two fibrinopeptides (A and B) from the central domain of the fibrinogen molecule. The

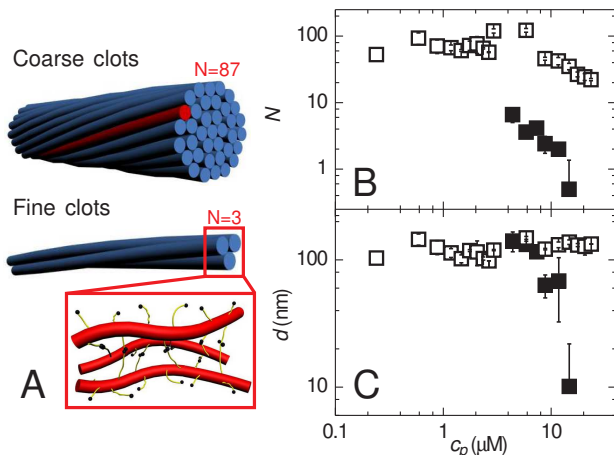


FIGURE 4.1. Two different structural limits of fibrin clot assembly. (A) Schematic showing fibrin fibers in *coarse* and *fine* clots, which differ in the number of protofibrils per cross-section, N , as indicated. The protofibrils are laterally associated by long, flexible α C-domains that protrude from their surface (yellow chains in zoom-in). (B) Bundle size and (C) diameter obtained by turbidimetry of fibrin gels assembled at different molar concentrations, c_p . Open symbols: *coarse clot* limit, solid symbols: *fine clot* limit.

exposed sites bind to complementary sites in the distal end domains of adjacent fibrin molecules. Next, the protofibrils laterally associate to form thicker fibers. The final bundle size N (i.e. the number of protofibrils per bundle) depends sensitively on pH, ionic strength and thrombin concentration [154]. In this study, we varied the pH and ionic strength, but used a fixed thrombin concentration (0.5 U/mL). We polymerized networks in two different limits. In the *coarse clot limit*, under near-physiological conditions, fibrin forms thick bundles composed of tens of protofibrils (Fig. 4.1 A *Top*). In the *fine clot limit*, at pH 8.5 and an ionic strength of 0.45, fibrin forms much thinner bundles, composed of 1-3 protofibrils only (Fig. 4.1 A *Bottom*).

To measure the bundle size of the fibers in the two structural limits, we performed turbidity measurements on gels with different fibrin concentrations, c_p . The wavelength dependence of the turbidity provides both the mass/length ratio, μ , and the diameter, d , of the fibers in their native, hydrated state [327] (see Chapter 2). The number of protofibrils can be calculated from μ using the mass/length ratio of single protofibrils, $\mu_{pf} = 1.5 \cdot 10^{11}$ dalton/cm, which follows from the molecular weight, M (340 kDa), and length, L (45 nm), of fibrin monomers: $\mu_{pf} = 2M/L$ [52]. The fibers in *coarse clots* consist on average of 87 protofibrils (open symbols in Fig. 4.1 B). The bundle size is independent of protein concentration up to 10 μ M (1 mg/ml fibrin corresponds to a molar concentration of 2.94 μ M), and then decreases slightly. Interestingly, the diameter of

the fibers is constant, with an average $d=120$ nm, over the entire concentration regime (open symbols in Fig. 4.1 C). This suggests a slightly reduced protein density in fibers formed at fibrin concentrations above $10 \mu\text{M}$. However, over the entire concentration range, the protein density within the fibers is rather low, being of order 0.18 g/cm^3 until $10 \mu\text{M}$ (see Chapter 3, Fig. 3.3 C). This is a consequence of the large spacing between protofibrils, mediated by the long and flexible αC -domains. In the *fine clot* limit, the number of protofibrils per fiber was much reduced, decreasing from $N=4$ at $4.41 \mu\text{M}$ to $N=1$ at $14.7 \mu\text{M}$ (closed symbols in Fig. 4.1 B). The fiber diameter was close to 100 nm, except at $15 \mu\text{M}$, where the diameter was 10 nm (closed symbols in Fig. 4.1 C). We suspect that this surprisingly large diameter may be an artifact arising from scattering by bundles or aggregates.

To obtain a more direct measurement of the fiber diameter, we imaged fibrin clots prepared at a concentration of 0.5 mg/ml by AFM in a dry state (Fig. 4.2 C). Fibrin networks polymerized at physiological conditions consist of thick fibers with diameter of ~ 130 nm and length exceeding tens of μm . In contrast, under higher pH and ionic strength, formation of much thinner filaments takes place. Occasionally, filaments bundle to create much thicker fibers.

To compare the structure of *fine* and *coarse clots* at the network scale, we performed confocal fluorescence microscopy. Both types of clots were homogeneous and isotropic. However, the thick fibers in the *coarse clots* could be resolved individually (Fig. 4.2 A-B *Bottom panels*), whereas the thinner fibers in the *fine clots* could not (Fig. 4.2 A-B *Top panels*). At the same mass density, the *fine clots* have much smaller voids between filaments than the *coarse clots*. This is in line with the much smaller mass/length ratio of the thin clot fibers. The mesh size, ξ , of an isotropic network of rigid fibers can be estimated from the total fiber length per volume, $\xi = 1/\sqrt{\rho}$. The length density follows from the known molar concentration of protein, c_p , and from the fiber mass/length ratio measured with turbidimetry: $\rho = Lc_p N_A / 2N$, where N_A is Avogadro's number and N is the number of protofibrils in a fiber ($N = \mu_{\text{fiber}} / \mu_{\text{pf}}$). For *coarse clots*, ξ is in the order of microns, well above the optical diffraction limit. In contrast, ξ in *fine clots* is close to $0.1 \mu\text{m}$, which is substantially smaller than the optical diffraction limit, making it difficult to resolve individual filaments. The spatial resolution is further reduced due to thermal fluctuations of the thin fibers during image acquisition.

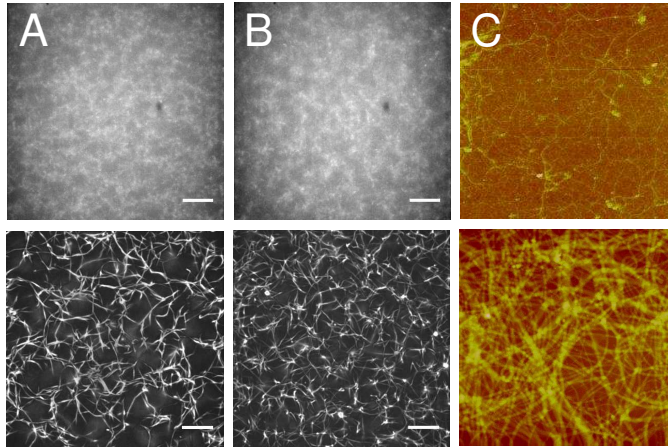


FIGURE 4.2. Structure of fibrin clots on the network and filament scale visualized by microscopy. (*Top panels*): Confocal (A, B) and AFM (C) images of *fine fibrin clots* polymerized at pH 8.5 and an ionic strength of 0.45 with 0.5, 1 and 0.5 mg/ml protein content, respectively. Confocal images are z-projections of 100 confocal planes over a $10\mu\text{m}$ -thick section of the gel with scale bars, $10\mu\text{m}$. AFM images show $10\times 10\mu\text{m}$ area. (*Bottom panels*): Corresponding confocal and AFM images of *coarse fibrin clots* assembled at physiological solution conditions.

Lateral aggregation of fibrin protofibrils is known to be promoted by the long, carboxy-terminal extensions of the α -chains (αC -domains) that protrude from the protofibril surface [102, 64, 187, 141]. The α -chains associate non-covalently [88], and these bonds are further reinforced by covalent crosslinking by the enzyme fibrinolytic factor XIII (FXIII) [193]. FXIII also generates covalent crosslinks between the γ -module of adjacent molecules. These dimeric γ - γ -crosslinks can be orientated longitudinally, or transversely between molecules of different strands [208, 214, 258, 305]. We quantified covalent crosslinking levels for the *coarse* and *fine gels* by SDS polyacrylamide-gel electrophoresis (SDS-PAGE). Uncleaved fibrinogen displays three characteristic bands on gel originating from its three constituent polypeptide chains: α (molecular weight: 63 kDa), β (56 kDa) and γ (47 kDa) [201] (Fig. 4.3 A-a). In *coarse clots*, the α - and γ -chains become cross-linked during polymerization, as evidenced by the disappearance of the α - and γ -chain band and the appearance of a major, high-molecular weight band at the top of the gel (Fig. 4.3 A-b). This high molecular weight material represents α_n -polymers of >250 kDa (multiple bonds between the αC -regions of adjacent molecules) and γ - γ dimers of 100 kDa. In contrast, in *fine clots*, we do not observe any conversion of α chains to α_n -polymers (Fig. 4.3 A-c). It is possible that a small fraction of α_n -polymers is present in a concentration that is too low to be observed on gel. Only formation of γ - γ dimers and compounds with molecular weights between 150-250 kDa can be seen. These compounds may correspond to hybrid α - γ bonds between protofibrils, which have also been reported for *coarse clots* (Fig. 4.3 B) [258]. The gel results suggest that the protofibrils in *fine clots* are not (significantly) coupled

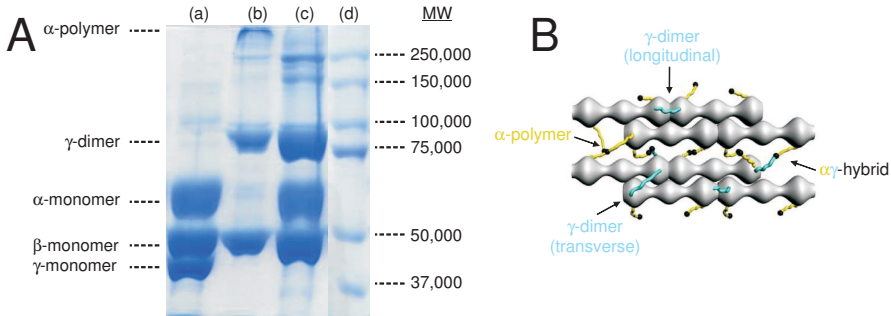


FIGURE 4.3. Quantification of covalent crosslinks within fibrin gels. (A) SDS-PAGE gel of fibrinogen (a), *fibrin coarse* (b) and *fibrin fine* (c) gels, (d) molecular weight marker. (B) Schematic representation of possible ligation pathways between fibrin molecules within/among protofibrils.

by α C-linkers, in contrast to protofibrils in *coarse clots*, which form distinct bundles held together internally by α C- α C crosslinks.

4.3.2 LOW-STRAIN MECHANICS OF FIBRIN GELS

We monitored fibrin polymerization in the rheometer, by subjecting polymerizing fibrin solutions to an oscillatory shear strain with a small enough amplitude to ensure linear response. Specifically, care was taken to avoid either stiffening or irreversible deformation of the network (see Chapter 2). Both *fine* and *coarse clots* showed an immediate rise in their linear elastic modulus upon initiation of network polymerization by addition of thrombin (Fig. 4.4 A). However, *fine clots* reached a constant stiffness within 10 minutes (closed symbols), whereas the stiffness of *coarse clots* continued to increase gradually for another few hours (open squared symbols). It has been reported that α C-crosslinks are formed slowly, whereas γ - γ crosslinks are formed within the first few minutes of polymerization [111, 280, 200]. To test whether slow formation of α C-crosslinks was responsible for the slow polymerization of *coarse clots*, we polymerized *coarse clots* in the presence of a specific inhibitor of γ -glutamyl- ϵ -lysine linkage formation (50 mM hydroxylamine) [269, 99]. In the presence of this inhibitor, the stiffness reached a constant value within 10 minutes (open circles in Fig. 4.4 A), supporting the hypothesis that slow polymerization of *coarse clots* is caused by slow formation of α C-crosslinks. The short polymerization time of the *fine clots*, on the other hand, suggests that there is negligible formation of α C-crosslinks, consistent with the SDS-PAGE results.

Covalent crosslinks are important for stabilizing contacts between protofibrils within fibers, and also between fibers. To test for the presence of intra-fiber crosslinks, we probed the frequency dependence of the linear viscoelastic moduli at small strain amplitudes. Both, *coarse* and *fine networks* behaved as almost perfectly elastic solids over the entire frequency range, independent of protein concentration (Fig. 4.4 B). The storage modulus, G' , was independent of fre-

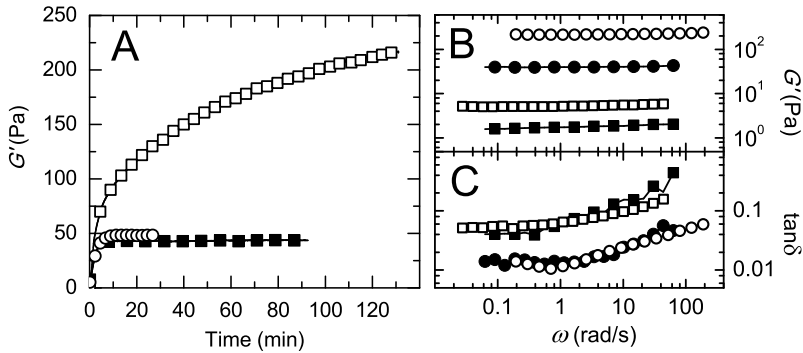


FIGURE 4.4. Linear viscoelastic behavior of *coarse* (open symbols) and *fine* (closed symbols) gels. (A) Polymerization of 3 mg/ml fibrin networks observed as an increase in the elastic shear modulus, G' , over time. In the presence of 50 mM hydroxylamine, 2 mg/ml fibrin network reaches a steady elasticity after only 10 minutes (circles). (B) Frequency dependence of G' for 0.5 (squares) and 3 mg/ml fibrin gels (circles). (C) Corresponding loss tangents, $\tan \delta = G''/G'$.

quency, ω , down to at least 0.02 rad/s. Moreover, the elastic modulus was always larger than the viscous modulus by a factor 10 for dilute gels (0.5 mg/ml) and a factor 100 for dense gels (3 mg/ml), indicating that there was little viscous dissipation (Fig. 4.4 C). Thus, even though α_n -polymer crosslinks were absent in fibrin *fine gels*, there were apparently still other types of crosslinks present to prevent structural relaxation. The *fine clots* at the same protein weight concentration always had a lower elastic modulus than the corresponding *coarse clot*. However, the loss tangents of *coarse* and *fine clots* at the same protein concentration were remarkably similar.

4.3.3 NONLINEAR RHEOLOGY OF FINE CLOTS

To test how reduced bundle size affects the nonlinear elastic behavior of fibrin networks, we subjected *fine clots* to different levels of a steady prestress, σ_0 , and measured the tangent modulus $K^*(\sigma_0, \omega)$ at this prestress by superposing a small amplitude oscillatory stress and measuring the oscillatory strain response (see Chapter 2). Remarkably, the networks displayed no creep up to absolute strains of 200%, and only a small amount of creep at even larger strains of 250% (Fig. 4.5 A). $K^*(\sigma_0, \omega)$ was therefore time-independent. The elastic tangent modulus, K' , and the viscous tangent modulus, K'' , were independent of applied prestress up to a certain characteristic stress value, σ_{crit} (Fig. 4.6 A, *regime 1*). In this linear elastic regime, K' and K'' correspond to the linear shear moduli, G' and G'' . Increasing σ_0 beyond σ_{crit} caused a strong increase in network stiffness, K' , with a complex dependence on stress. At all fibrin concentrations, there was an initial fast rise in stiffness (*regime 2*), followed by a slower rise (*regime 3*), and then another fast rise just before network rup-

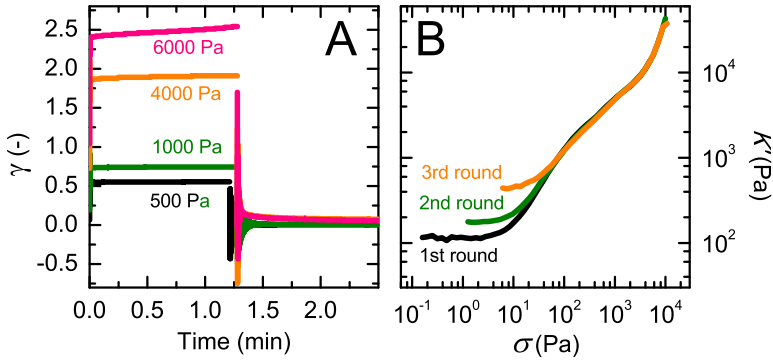


FIGURE 4.5. Creep response of 3 mg/ml fibrin gel under different levels of prestress (A) and reproducibility of stiffening behavior for a 4 mg/ml fibrin network (B), which is subjected to three consecutive steady shear ramps with the steady shear going up.

ture (*regime 4*). The total extent of stiffening before rupture, relative to the initial elastic modulus, decreased with increasing protein concentration: dilute gels (0.5 mg/ml) stiffened 1000-fold, whereas dense gels (3 mg/ml) stiffened only 100-fold. The strain-stiffening curves showed no hysteresis in the nonlinear regime during repeated stress sweeps, even when the stress had been increased close to the rupture stress (Fig. 4.5 B). However, the initial (linear) network stiffness increased with each cycle. This work-hardening phenomenon is reminiscent of observations for F-actin networks crosslinked with filamin [189, 263]. Actin-filamin networks have similarly large rupture strains as the fibrin gels. At large strains, the filaments will align, and this alignment may lead to partly irreversible bundling, as shown in the case of actin-filamin gels by fluorescence confocal microscopy during shear [189].

Stress-stiffening behavior is a common feature of many different types of biopolymer networks, including networks of fibrin, collagen, actin, and intermediate filaments [285, 151, 94]. In case of actin and intermediate filaments, this behavior was shown to be well described by an affine entropic model for semiflexible polymers. This model assumes that stiffening is caused by stretching of the thermally undulating polymer segments between crosslinks [195]. Moreover, it assumes that the network deforms in a uniform (affine) manner, so that the macroscopic elastic modulus can be calculated by performing an orientational average over all filaments [285]. Semiflexible polymers have a highly nonlinear force-extension behavior, with an entropic stretch modulus that diverges once the stored length is pulled out and the end-to-end length reaches the contour length. The model predicts for the linear elastic modulus, G_0 , and critical stress, σ_{crit} , the following dependencies on filament persistence length, l_p , and crosslink distance l_c :

$$\begin{aligned}
 G_0 &= 6\rho k_B T \frac{l_p^2}{l_c^3} \\
 \sigma &= \rho k_B T \frac{l_p}{l_c},
 \end{aligned}
 \tag{4.1}$$

where $k_B T$ denotes thermal energy and ρ is the contour length density. In the nonlinear regime, at stresses above σ_{crit} , the stiffness is expected to scale with stress as $K' \sim \sigma^{3/2}$. Stiffening curves measured at different protein concentrations are therefore expected to collapse onto a single master curve when rescaled by G_0 and σ_{crit} [94]. The stiffening curves of *fine fibrin clots* for concentrations between 0.5 and 5.8 mg/ml do indeed collapse onto one mastercurve when the modulus is normalized by G_0 and the stress is normalized by σ_{crit} (Fig. 4.6 B). This suggests that the linear modulus and the onset of stress-stiffening are indeed well described by the affine entropic model. However, the collapse only works up to stresses that are 10-fold larger than σ_{crit} . At larger stress, there are noticeable differences between the curves. Moreover, the rise in stiffness is weaker than the 3/2-increase predicted for inextensible semiflexible polymers (solid line). This behavior is in contrast with the stiffening behavior of rigidly crosslinked actin networks, which do stiffen as $K' \sim \sigma^{3/2}$, but it is similar to the stiffening behavior observed in previous studies of *coarse fibrin clots* (see Chapter 3), fish protofibril gels [285], and intermediate filament networks [180]. The deviation from the affine entropic model in those studies was ascribed to extensibility of the filament backbone and the stiffening curves were well described by the affine entropic model when enthalpic stretching was included [285, 222, 180]. The difference between the rheology of fibrin and intermediate filaments as compared to actin is in line with force-extension measurements on single fibers: fibrin fibers and intermediate filaments have a much smaller stretch modulus and larger extensibility [191, 153, 299] than actin filaments [192].

To test whether the affine entropic model extended with backbone extensibility can fit the nonlinear elastic stiffening of *fine clots*, we fitted the model to the measured stiffening curves over the entire stress range. We used three fit parameters, the crosslink distance l_c , persistence length l_p , and stretch modulus $\kappa_{stretch}$. We find excellent agreement of the theory with the experimental data for all protein concentrations, as exemplified for two protein concentrations (0.5 and 3 mg/ml) in Fig. 4.6 A (solid lines are theory curves). The theory captures the initial stiffening, caused by stretching of the thermally undulating fibrin fibers, as well as the slower stiffening at large stress. By itself, backbone extensibility leads to a saturation of the elastic modulus if the fibers have a linear stretch modulus. However, fiber alignment at large strains (*regime 3*) causes weak network stiffening simply by a geometrical effect. At high stress, just before network rupture (*regime 4*), the model underestimates the stiffness of the *fine clots*. This small discrepancy may indicate an intrinsic nonlinearity in the backbone elasticity of protofibrils. In fibrin *coarse clots*, we also identified stiffening at high stress due to an intrinsic nonlinearity in fiber stretching [232] (see Chapter 3). However, this nonlinearity was much more pronounced for *coarse clots* than it is for *fine clots*.

To thoroughly test the validity of the affine entropic model, we checked

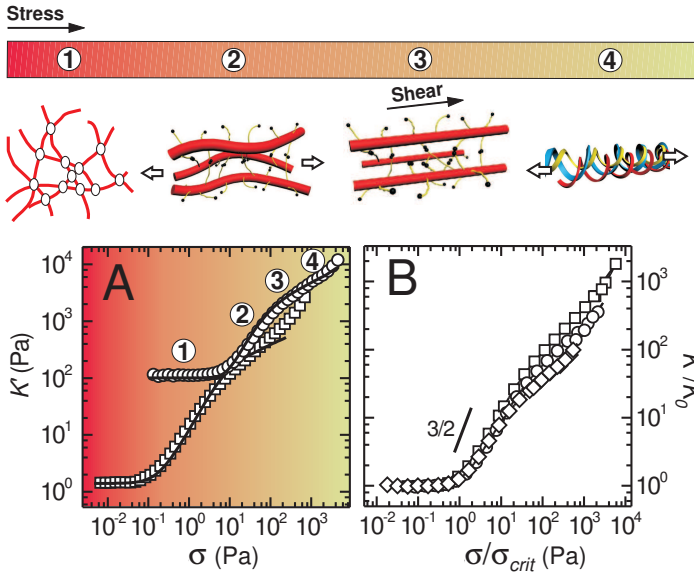


FIGURE 4.6. Nonlinear elastic response of *fine fibrin* networks with increasing levels of prestress (bar). (A) Stress-stiffening behavior of 0.5 (squares) and 3 mg/ml (circles) gels. Solid lines represent the affine entropic model for semiflexible polymers with a finite stretch modulus. The model was fitted to the data using three fit parameters, the crosslinking distance, l_c , the filament persistence length l_p , and stretch modulus, $\kappa_{stretch}$. (B) Stress-stiffening curves rescaled by G_0 and σ_{crit} , using values calculated from the best-fit values of l_c and l_p according to Eq. (4.1). Data are shown for 0.5 (squares), 2 (circles) and 4 mg/ml (diamonds) fibrin networks. Solid line indicates $3/2$ power-law stiffening expected for inextensible semiflexible chains. Cartoons above the graphs sketch the proposed mechanism underlying the 4 distinct regimes in the stress-stiffening curves: (1) entropic stretching of filaments between network crosslink points, (2) enthalpic stretching of filament backbones, (3) shear-induced alignment of filaments, and (4) forced unfolding of fibrin monomers within the filaments.

whether the fits returned physically reasonable values for the fit parameters. When we assumed an average bundle size of $N=3$, based on the turbidimetric data, we found unphysically small values for l_c and l_p . The apparent persistence length, for instance, was only 50 nm ($l_p=0.048 \mu\text{m}$ and $l_c=0.055 \mu\text{m}$ for 1 mg/ml fibrin network), which is inconsistent with values estimated from electron microscopy and atomic force microscopy of fish fibrin protofibrils (500 nm, [285, 307]), and by light scattering for human fibrin protofibrils (200 nm, [22]). If we instead assumed a bundle size of $N=1$, we obtained much more reasonable values for l_p , around 150 nm (inset of Fig. 4.7 C) and also for l_c . The crosslink distance decreased from $0.25 \mu\text{m}$ at 0.5 mg/ml fibrin to $0.05 \mu\text{m}$ at 3 mg/ml (symbols in Fig. 4.7 C). These values are similar to l_c values reported for intermediate filaments, which have a similar diameter (~ 10 nm) and persistence length (0.5-1 μm) as fibrin protofibrils [182]. The values are close to their lower

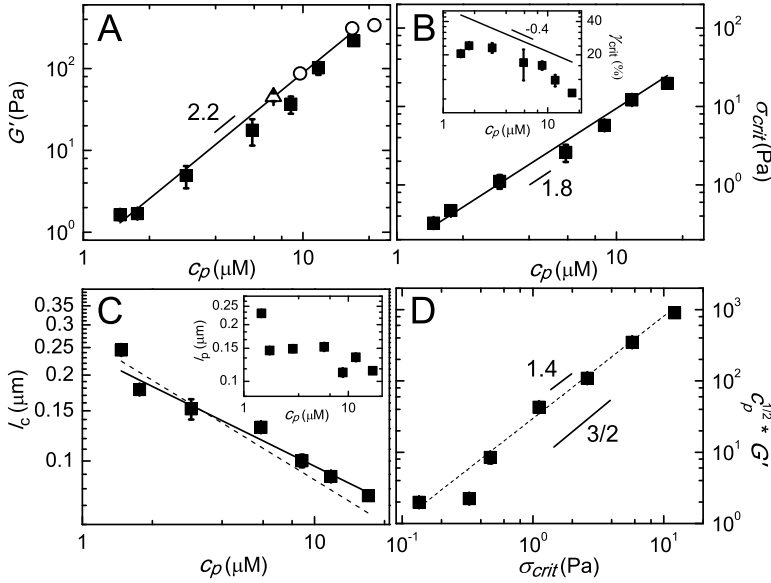


FIGURE 4.7. Concentration dependence of rheological and structural parameters derived from the rheology data in the context of an affine entropic model of semiflexible polymers. (A) Scaling of the elastic modulus with protein concentration. Data obtained in this study (closed symbols) agree well with data from other studies (open symbols) [307, 213] and with theory (line). (B) The critical stress (squares) also agrees well with theory (line). (*Inset*): Corresponding critical strain, which scales as $c_p^{-0.4}$. This scaling is consistent with theory, but the experimental values are 2-fold larger than predicted (line). (C) The crosslink distance decreases with concentration, in agreement with theory when assuming $l_c = l_e$ (solid line). The values are close to their lower bound, $l_c = \xi$ (dashed line). (*Inset*): the persistence length is $0.15 \mu\text{m}$, independent of concentration. (D) The plateau modulus and critical stress are internally consistent as predicted by the theory, showing a $3/2$ power-law slope (solid line) in the rescaled form of Eq. (4.3). Dashed line represents best-fit power-law slope of 1.4.

bound, corresponding to dense crosslinking, where the crosslink distance is comparable to the mesh size, $l_c = \xi$ (dashed line). The crosslink distance for semiflexible polymers is expected to be proportional to the entanglement length, l_e , which scales as $l_e \sim l_p^{1/5} \rho^{-2/5}$ [195, 94, 221]. Our measured values for l_c agree remarkably well with this prediction, with a proportionality constant of 1 (solid line in Fig. 4.7 C represents $l_c = l_e \sim l_p^{1/5} \rho^{-2/5}$). This proportionality constant is comparable to the value of 0.35 that we found for *coarse clots* (see Chapter 3).

The fact that all three fit parameters have realistic values when we assume a bundle size of $N=1$ suggests that the network behaves mechanically as if it is composed of protofibril filaments that are crosslinked at intersections. If the protofibrils within a fiber are loosely associated, then it seems reasonable that one cannot distinguish between crosslinks within or between fibers. The

protofibrils effectively behave independently from each other and contribute individually to the mechanical response of the network. This is different from *coarse clots*, where the fibers are distinct bundles consisting of a much larger number of protofibrils ($N=87$).

With the values for l_c and l_p obtained from the fits of the affine entropic model to the data, we can compute the linear elastic modulus, G_0 , and critical stress, σ_{crit} , using Eq. (4.1). We find excellent agreement of the experimental data and the calculated values in both cases. G_0 increases with fibrin concentration according to a power-law with exponent 2.2, in agreement with the predicted $c_p^{11/5}$ -scaling (Fig. 4.7 A). This exponent also falls well within the range of 2.1-2.3 reported previously for ligated fibrin *coarse clots* [270, 91, 213, 95, 232], and the absolute magnitude of the moduli agree well with prior measurements on *fine clots* (open symbols in Fig. 4.7 A) [307, 213]. The critical stress increases with concentration according to a power-law with exponent 1.8 in accordance with the predicted $c_p^{9/5}$ -scaling (Fig. 4.7 B). The corresponding critical strain, γ_{crit} , scales as $\gamma_{crit} \sim c_p^{-0.4}$, consistent with the theoretical prediction,

$$\gamma_{crit} = \frac{1}{3} \frac{l_c}{l_p} \quad (4.2)$$

However, the measured strain values are 2-fold larger than predicted. This small discrepancy suggests that the network deformation may be somewhat nonaffine due to bending or rotation of filaments; simulations show that nonaffinity postpones the onset of nonlinearity [224, 144, 40]. However, nonaffinity, if indeed present, is small, given that the linear modulus agrees well with theory. It is important to note that the affine model for G_0 that we use here represents an upper bound on the shear modulus for given values of the various parameters in the model, all of which except l_c are known independently. Furthermore, since our inferred values of l_c are close to their lower bound of ξ , if the network deformation in our samples were to be predominantly nonaffine, a significantly smaller value of G_0 would be expected. This conclusion is consistent with an earlier direct mapping of the strain field in sheared gels of fish fibrin protofibrils, which showed only slight nonaffinity at small strain, which decreased with increasing strain [307].

As a final test of the internal consistency of our data, we checked whether we could collapse all data onto a single master curve using the theoretically predicted rescaling form:

$$c_p^{1/2} G_0 \sim \sigma_{crit}^{3/2}, \quad (4.3)$$

which follows from Eq. (4.1). As shown in Fig. 4.7 D, the data are indeed in excellent agreement with Eq. (4.3), showing a power-law scaling close to 3/2 (best-fit value is 1.4, dashed line). Together with the fact that we obtain physically meaningful values of l_c and l_p from the affine model, this scaling provides strong evidence that the linear elasticity of fibrin fine gels is entropic in origin.

The affine entropic model gives a good description of the stress-stiffening behavior of fibrin gels over nearly the entire stress range. Even the upturn in

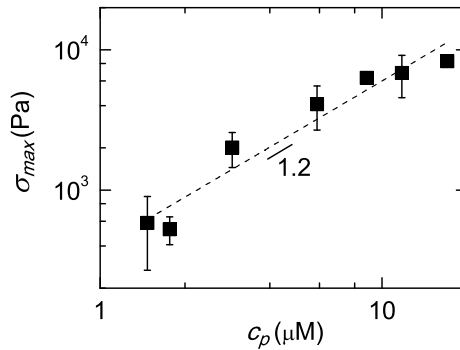


FIGURE 4.8. Maximum (rupture) stress of *fine clots* as a function of protein concentration. Dashed line indicates power-law fit with exponent 1.2.

the stress-stiffening curves at large stress is rather well captured by the model, which predicts slight stiffening due to shear-induced alignment of the protofibrils (*regime 3* in Fig. 4.6 A). This alignment may also account for the work-hardening phenomenon observed during repeated stress sweeps (Fig. 4.5 B). The shear cell described in Chapter 8 may permit us in future to quantify the degree of alignment as a function of strain, and confirm whether it is indeed consistent with the affine prediction.

Just before rupture, the *fine clots* stiffen slightly stronger than captured by the affine entropic model (*regime 4* in Fig. 4.6 A). This additional stiffening may reflect intrinsic nonlinearities in the protofibril stretch modulus occurring at large strain. Such nonlinearities may arise from forced unfolding of fibrin monomers or from entropic stretching of the flexible αC -domains. Forced unfolding has been shown to occur in *coarse fibrin clots* under tensile load [44], in single stretched fibers [44, 179], and in single molecules [43, 179]. Stretching of αC -domains was demonstrated in single-stretching experiments of *coarse clot* fibers [82]. To confirm whether unfolding occurs also in *fine clots*, complementary measurements will be needed, for instance using small-angle X-ray scattering (SAXS) [44] or by staining with dyes that bind to unfolded, β -sheet rich structures [239]. To test the role of the αC -domains, the rheology could be repeated with networks prepared from derivatives of human plasma fibrinogen whose αC -domains are enzymatically removed [203], or with fibrinogen from different species, which varies in the length of the αC -domains [82].

Forced unfolding of molecules or stretching of flexible αC -domains may contribute to the remarkable resilience of fibrin networks against large strains. Fibrin *fine gels* can survive strains of up to at least 250% (Fig. 4.5 A). The rupture stress, σ_{max} , is always at least 1000-fold larger than σ_{crit} , and it increases with protein content according to a power-law with exponent 1.2 (Fig. 4.8)

4.3.4 COMPARISON BETWEEN *FINE* AND *COARSE CLOT* RHEOLOGY

In Chapter 3, we proposed that the rheology of fibrin *coarse clots* can be described by an affine entropic model, where the fibers behave as semiflexible bundles of $N=87$ loosely coupled protofibrils. If this is true, then the *coarse*

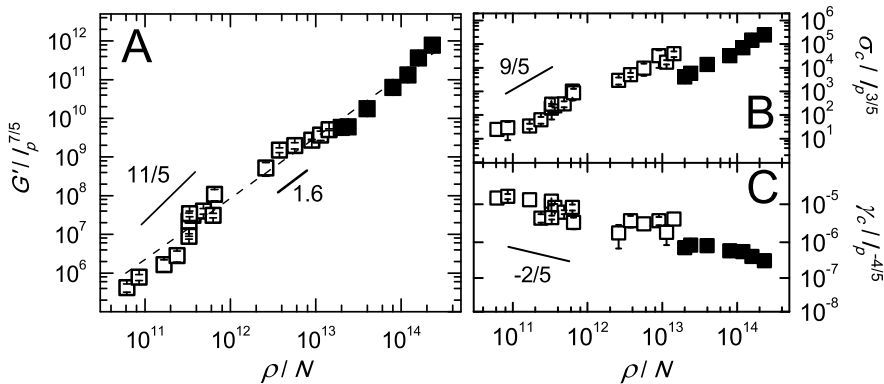


FIGURE 4.9. Comparison of the linear modulus (A), critical stress (B) and critical strain (C) for *coarse* (open symbols) and *fine* (closed symbols) fibrin gels, with the y-axes rescaled by fiber persistence length, l_p . Solid lines indicates the scaling expected based on the affine entropic theory.

clot data should be consistent with the *fine clot* data upon rescaling of the linear modulus, critical stress, and stretch modulus with the bundle-size dependent persistence length, $l_p = Nl_p^f$, where l_p^f is the persistence length of a single protofibril. To test this prediction, we first plot the linear modulus rescaled by $l_p^{7/5}$ as a function of contour length density (Fig. 4.9 A). We indeed find rather good agreement between the datasets for *coarse* and *fine clots*: the rescaled moduli nearly fall onto mastercurve with a power-law slope of 1.6 (close to the expected $11/5$ slope). We next test the correspondence of the critical stress (rescaled by $l_p^{3/5}$) and critical strain (rescaled by $l_p^{-4/5}$) of *fine* and *coarse clots*. As shown in Fig. 4.9 B-C, both the stress and strain of the *coarse clots* is higher than expected based on the *fine clot* data, though they exhibit similar scaling with filament concentration.

The larger critical stress and strain of the *coarse clots* compared to the *fine clots* suggests a higher degree of nonaffinity in the *coarse gels*. Indeed, the *coarse clots* are expected to be less affine than *fine gels*. Based on recent lattice simulations, a phase diagram was proposed which maps the affinity as a function of the network connectivity, z , and the ratio of bending/stretching rigidities, $\kappa_{bend}/\kappa_{bend}l_c^2$ [40]. The local connectivity in fibrin networks is expected to be on average between $z=3$ (corresponding to a branch) and $z=4$ (corresponding to two fibers crosslinked at a crossing). For $z=3$, the defor-

mation field is expected to crossover from nonaffine to affine at a dimensionless ratio $\kappa_{bend}/\kappa_{bend}l_c^2$ of 10^{-2} . Below this crossover ratio, fiber bending dominates, while above it, affine stretching. If we assume that the stretch modulus has an entropic origin, then [195]:

$$\kappa_{stretch} = 90\kappa_{bend} \frac{l_p}{l_c^3} \quad (4.4)$$

For *fine clots*, the crosslink distance l_c is comparable to the persistence length, l_p (Fig. 4.7 C), so the dimensionless crossover ratio is 10^{-2} . In *coarse clots*, the protofibrils are bundled, so the mesh size is larger than in *fine gels*. At a constant molar concentration of fibrin, the average crosslink distance increases with N as:

$$l_c = N^{1/2}l_c^{pf}, \quad (4.5)$$

where l_c^{pf} is the crosslink distance for the protofibril gel. The persistence length of the *coarse clots*, for completely loosely coupled bundles, is defined as:

$$l_p = Nl_p^{pf} \quad (4.6)$$

The crossover ratio scales therefore as $N^{-1/2}$:

$$\frac{\kappa_{bend}}{\kappa_{stretch}l_c^2} = \frac{1}{90} \frac{l_c^{pf}}{l_p^{pf}} N^{-1/2} \quad (4.7)$$

For *coarse clots* with $N=87$, this implies a ratio of 10^{-3} , 10-fold smaller than for *fine clots*. This implies that *coarse gels* are indeed expected to be less affine than *fine gels*. This nonaffinity could explain the enhancement of the critical stress and strain of *coarse clots* over the affine predictions. Yet, the linear modulus of the *coarse clots* agrees well with the affine prediction, suggesting that the degree of nonaffinity in *coarse networks* is still rather small.

Finally, we compared the enthalpic stretch moduli of the protofibrils as inferred from the rheology of *coarse clots* (normalized by $N=87$) and *fine clots*. We find remarkably good agreement between the stretch moduli obtained from *coarse* and *fine gels* rheology data (Fig. 4.10). This agreement corroborates the proposition in Chapter 3 that the *coarse clots* stiffen by an entropic mechanism combined with backbone extensibility, analogously to the *fine clots*. The stretch modulus extracted from the rheology data varies between 175 and 300 pN (solid squares in Fig. 4.10). These values are consistent with the stretch modulus of fish fibrin protofibrils (50-100 pN) [285]. The Young's modulus, assuming cylindrical fibers with a diameter of 9 nm and homogeneous elasticity, is 3-5 MPa. This value is consistent with single-fiber stretching and bending experiments on fibers within *coarse fibrin clots* (14 MPa) [65].

The most striking difference between the stiffening behavior of *coarse* and *fine clots* is that the *coarse clots* show a more pronounced nonlinearity at large

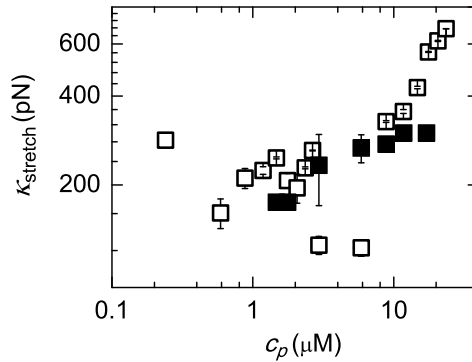


FIGURE 4.10. Protofibril stretch modulus retrieved from the strain-stiffening behavior of fibrin *fine clots* (closed symbols) and *coarse clots* (open symbols).

stress, with a distinct stiffening regime that scales as $K' \sim \sigma^{3/2}$, as expected from an entropic mechanism. Single fiber stretching experiments with *coarse clot* fibers also demonstrated intrinsically nonlinear stretching [143]. We proposed in Chapter 3 that this entropic stretching regime corresponds to stretching of flexible domains inside fibers. This interpretation relies on having distinct bundles, with a separation of length scales between crosslinks of protofibrils inside bundles and crosslinks between the surfaces of different bundles. Such a separation of scales is reasonable for the *coarse clots*, where the fibers have a large bundle size. In contrast, the protofibrils in *fine clots* behave as mechanically individual filaments.

4.4 CONCLUSION

Fibrin clots are among the most resilient protein networks found in the human body. Their supramolecular, internal structure assures high extensibility of the individual fibrin filaments and contributes to the rich nonlinear response of fibrin networks to large deformations. Fibrin fibers are composed of thin, semiflexible protofibrils that are laterally connected by flexible polypeptide linkers. The bundle size is sensitive to the solution conditions, including pH and ionic strength. In this chapter, we focused on the so-called “*fine clot*” regime at high pH and high ionic strength, where the bundle size is minimal. Turbidity measurements indicate a bundle size of 3. We showed that *fine clots* behave rheologically as networks of semiflexible polymers with a fine backbone extensibility. The clots strongly stress-stiffen, and stiffening is accurately described by an affine entropic model of polymers with a linear backbone elasticity over nearly the entire range of stress. Only at the highest levels of stress, just before network rupture, we see some evidence of intrinsic nonlinearity in the protofibril backbone extensibility that is not captured by the model.

The rheology of *fine clots* also provides key insights into the basis of the

stress-stiffening behavior of so-called “*coarse fibrin clots*” that form at near-physiological conditions. *Coarse clots* consist of fibers that are thick bundles of protofibrils. We compared the stress-stiffening behavior of *fine clots* with that of *coarse gels* with a bundle size of $N=87$. At small to moderate stress, both *fine* and *coarse clots* stiffen in accordance with the affine entropic model including backbone extension. The linear stretch modulus of the *fine clot* fibers agrees well with that of the *coarse gels* upon rescaling by bundle size. However, the *coarse clots* show a distinct stiffening regime at high stress that points to an intrinsically nonlinear entropic elasticity of the fiber backbone. This regime is not seen for *fine gels*. This difference from the *fine clot* rheology corroborates our proposition in Chapter 3 that the intrinsic nonlinear elasticity of the *coarse clot* fibers derives from their loose bundle structure.

The theoretical modeling and fitting of the experimental data to the model was performed by Chase Broedersz (Vrije Universiteit, Amsterdam). I also would like to thank Karin Jansen for providing data for this chapter as a part of her internship project at AMOLF; and Chase Broedersz and Fred MacKintosh (Vrije Universiteit, Amsterdam) for the fruitful discussions and collaboration.

5 FINGERPRINTING THE NONLINEAR RHEOLOGY OF FIBRIN CLOTS

VISCOELASTIC materials such as colloidal suspensions and polymer gels generally exhibit a nonlinear stress response to an applied shear strain and various methods have been devised to probe this nonlinearity. A popular method is the large amplitude oscillatory shear technique (LAOS), where a sinusoidal strain is applied and the stress response is measured. Nonlinearities in the stress can be "fingerprinted" by Fourier transforming, decomposition, or Lissajous plots. In biopolymer networks it is, however, difficult to interpret the physical basis of these fingerprints, since their nonlinear behavior is still incompletely understood. In this chapter, we explore different methods to probe the nonlinearity in the strain response of fibrin gels to an applied large amplitude oscillatory stress. We find that the sensitivity of Fourier Transform strain spectra and Lissajous stress/strain curves to the onset of strain-stiffening is comparable to the sensitivity of differential measurements, where a small oscillatory stress is superposed on a steady prestress. In the nonlinear regime, the Lissajous curves show complex shapes, whose interpretation is uncertain.

I.K. Piechocka, B. Alonso-Latorre, G.H. Koenderink
Manuscript in preparation

5.1 INTRODUCTION

Soft matter is a class of materials that is built of mesoscopic building blocks such as colloids, polymers, or bubbles. These building blocks are much larger than molecules, yet small enough to be susceptible to thermal fluctuations. Soft matter tends to exhibit viscoelastic behavior, which is time-dependent and changes under applied load. Biological materials such as cells and tissues can also be categorized as soft matter, since they are built of protein biopolymers such as actin, collagen, and fibrin. Gels reconstituted from purified protein biopolymers are viscoelastic and remarkably sensitive to applied loads. Typically, the gels already start to exhibit a nonlinear elastic response at shear or tensile strains of a few percent [285]. Crosslinked biopolymer networks generally strain-stiffen strongly, sometimes by up to factors of 100-1000, before rupture [246, 267, 307, 94, 325, 39]. Fibrin gels offer a particularly striking example of nonlinearity. They can withstand shear strains of up to 300% and can stiffen up to 1000-fold [191]. This rheological response provides resilience, which likely contributes to the efficacy of fibrin blood clots in stemming blood loss and promoting wound healing [169].

Several methods have been devised to characterize the nonlinear response of soft materials to an applied shear. A traditional method is large amplitude oscillatory shear (LAOS). In a strain-controlled experiment (which is most common), a sinusoidal strain, $\gamma(t)$, is applied, and the oscillatory stress response, $\sigma(t)$, is measured (Fig. 5.1 A):

$$\begin{aligned}\gamma(t) &= \gamma_0 \sin(t) \\ \sigma(t) &= \sigma_0 \sin(\omega t + \delta),\end{aligned}\tag{5.1}$$

where γ_0 is strain amplitude and the phase difference $\delta = G''/G'$. Here, G'' is the viscous (out-of-phase) component, and G' it the elastic (in-phase) component of the complex shear modulus, G^* :

$$G^*(\omega) = G'(\omega) + iG''(\omega)\tag{5.2}$$

Oscillatory measurements on fibrin clots show an increase in the elastic modulus above critical strain amplitudes of around 10% [149, 13]. However, it is difficult to interpret the modulus at strains above the critical strain, since the stress response in the nonlinear regime is highly non-sinusoidal [155]. G^* is commonly obtained in LAOS from the first harmonic in the response, and does not take into account higher-order terms, which do store energy [93]. For strain-stiffening materials such as fibrin gels, G^* underestimates the modulus in the nonlinear regime, since its correspond to the ratio of stress over strain, σ/γ , which is smaller than the local derivative, or slope, $\delta\sigma/\delta\gamma$ (see Fig. 5.1 D). Several methods have been proposed to probe the differential modulus, $K^* = \delta\sigma/\delta\gamma$. One method is known as the prestress or differential technique, where a small amplitude oscillatory stress is superposed on a large steady stress (Fig. 5.1 B). This method works particularly well for materials that are predominantly elastic

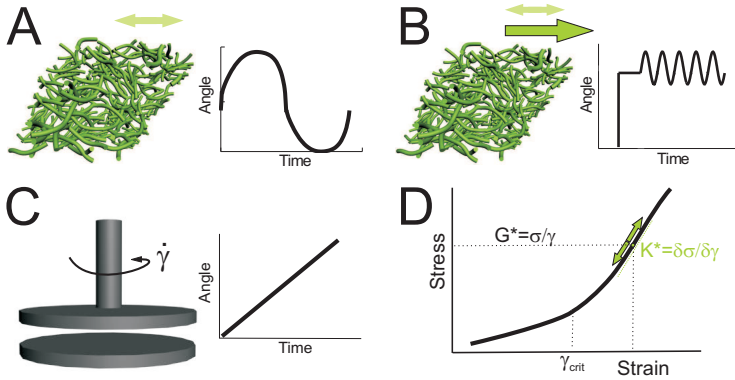


FIGURE 5.1. Schematic representation of three different commonly used techniques to measure nonlinearities in biopolymer networks and other soft materials: LAOS (A), prestress method (B), strain-ramp protocol (C). (D) The difference between the LAOS complex modulus G^* and the prestress differential modulus K^* illustrated for a strain-stiffening material.

and show minimal creep, and have already been applied to fibrin gels previously [39, 232]. An alternative method is the strain-ramp protocol, where the material is subjected to a steady shear with strain rate, $\dot{\gamma}$ [39, 265] (Fig. 5.1 C). This method returns a rate-dependent elastic modulus, which tends to agree with the prestress method at small rates of strain. In case of fibrin gels, the differential moduli obtained from the strain-ramp and prestress methods agree well, since these gels are nearly perfect elastic solids [39].

The advantage of the differential moduli is that they can be directly and quantitatively compared with theoretical models, which has helped to elucidate the mechanistic origin of the nonlinear rheology of actin gels [94], intermediate filament networks [325, 180, 182], and fibrin [232]. In contrast, the moduli obtained from LAOS suffer from a non-sinusoidal signal in the nonlinear regime and cannot be directly compared with models. However, it has been proposed that LAOS can be a useful and unique technique to fingerprint the nonlinear response of soft materials provided that the full spectrum of the stress (strain) response, including higher harmonics, is analyzed [81]. Several fingerprinting methods have been proposed and applied to nonbiological soft matter such as foams [256], and polymers [79], and to a few selected biological materials, such as native pedal mucus [78, 79]. However, these methods have not yet been applied to fibrin gels.

The most common method to analyze LAOS data in the nonlinear regime is known as Fourier transform (FT) rheology. The stress response to an oscillatory strain input is decomposed in terms of a Fourier series [312]:

$$\sigma(t; \omega, \gamma_0) = \gamma_0 \sum_{n \text{ odd}} G'_n(\omega, \gamma_0) + G''_n(\omega, \gamma_0) \cos n\omega t, \quad (5.3)$$

where the mode number n includes only odd harmonics, since the stress is a

function of shear direction and its sign changes as the sign of shearing changes. G'_1 and G''_1 are the first-harmonic viscoelastic coefficients that are generally reported by commercial rheometer software. At small strain amplitudes and low frequencies, the Fourier transformed stress shows a single response peak with intensity $I(\omega_1)$ at the excitation frequency, ω . This dominant intensity contributes in 99% to the linear response. The contribution of 3rd and 5th harmonic, $I_3(\omega_1)$ and $I_5(\omega_1)$, is less than 1% and it is usually not included into data analysis. As the strain amplitude increases, higher harmonics appear, and the ratio of their intensities relative to the first harmonic ($n=1$) has been proposed to provide a characteristic fingerprint of the material [313]. Furthermore, it has been proposed that the appearance of higher harmonics is a more sensitive indicator of nonlinearity than the appearance of nonlinearity in the first-harmonic modulus, G'_1 [245]. Since the intensity of the higher harmonics grows with an odd power of strain amplitude [212], the intensity of the third harmonic scaled by the first, I_3/I_1 , is expected to show a quadratic dependence on strain. Based on this scaling, two new nonlinear coefficients to characterize the relaxation dynamics of polymer chains were recently introduced [146]. However, the physical meaning of these coefficients, and in fact the interpretation of the higher harmonics in the Fourier spectrum themselves, is not fully understood yet and remains a matter of debate [159]. It is particularly problematic to deconvolve the elastic (stored energy) and viscous (dissipated energy) response, since the FT analysis only considers the nonlinearity of the total stress. To overcome this limitation, an alternative method was recently proposed, where the total LAOS stress is decomposed into an elastic stress, $\sigma'(\gamma(t))$, which is a function of strain, and a viscous stress, $\sigma''(\dot{\gamma}(t))$, which is a function of strain rate [59]. This decomposition provides generalized storage and loss moduli that remain meaningful at large deformations:

$$\begin{aligned}\sigma' &\equiv \gamma_0 \sum_{n \text{ odd}} G'_n(\omega, \gamma_0) \sin n\omega t \\ \sigma'' &\equiv \gamma_0 \sum_{n \text{ odd}} G''_n(\omega, \gamma_0) \cos n\omega t\end{aligned}\tag{5.4}$$

Further orthogonal decomposition of the elastic and viscous stress using Chebyshev polynomials of the first kind gives harmonic components, or Chebyshev coefficients [79]. These coefficients provide a quantification of the elastic and viscous nonlinearities:

$$\begin{aligned}\sigma'(x) &= \gamma_0 \sum_{n \text{ odd}} e_n(\omega, \gamma_0) T_n(x) \\ \sigma''(x) &= \gamma_0 \sum_{n \text{ odd}} \nu_n(\omega, \gamma_0) T_n(y),\end{aligned}\tag{5.5}$$

where $T_n(x)$ is the n^{th} -order Chebyshev polynomial of the first kind, and $e_n(\omega, \gamma_0)$ and $\nu_n(\omega, \gamma_0)$ are the elastic and viscous Chebyshev coefficients, respectively. The latter coefficients can be directly related to the time-domain Fourier coefficients [79]:

$$\begin{aligned} e_n &= G'_n(-1)^{(n-1)/2}, n \text{ odd} \\ \nu_n &= G''_n/\omega = \eta'_n, n \text{ odd} \end{aligned} \quad (5.6)$$

The sign of the third-order Fourier coefficient can now be attributed to the stiffening/softening and thickening/thinning nature of the probed material.

A different way to decompose the LAOS stress response into elastic and viscous components is to use a geometrical interpretation of the stress in the form of Lissajous-Bowditch plots [231]. These are parametric plots of the total shear stress versus strain whose shape provides another way to fingerprint the nonlinear rheological response of the material. In the linear regime, Lissajous curves are straight lines for a purely elastic solid, circles for a purely viscous fluid, and ellipses for a viscoelastic material. The area enclosed by the Lissajous curve can be physically interpreted as the total energy dissipated per unit volume, $E_d = \pi\gamma_0^2 G''_1$, where G''_1 is the loss modulus of the first harmonic [93]. As the strain amplitude increases, the Lissajous curve shape for viscoelastic materials deviates from an elliptical shape in a manner that reflects the type of nonlinear response. The frequency dependence of this response can be probed by performing LAOS tests at different frequencies, ω , and arranging the resulting Lissajous curves in the form of a Pipkin diagram [233]. This diagram visualizes how the elastic and viscous response depend on frequency under increased levels of deformation. The onset of nonlinearity can be estimated from the Lissajous curves through the minimum-strain modulus, G'_M (the slope of the Lissajous curve at zero strain), and the large-strain modulus, G'_L (the ratio of stress and strain at maximum strain), which capture the local elastic response of the material at small and large strains, respectively [79]. These moduli can be related to the FT description and the Chebyshev stress decomposition, providing a geometrical interpretation of the elastic and viscous moduli in the nonlinear regime:

$$\begin{aligned} G'_M &\equiv d\sigma/d\gamma_{\gamma=0} = \sum_{n \text{ odd}} nG'_n = e_1 - 3e_3 + \dots \\ G'_L &\equiv \sigma/\gamma_{\gamma=0} = \sum_{n \text{ odd}} G'_n(-1)^{(n-1)/2} = e_1 + e_3 + \dots \end{aligned} \quad (5.7)$$

The strain-stiffening index, $S_{\gamma_0} \equiv (G_L(\gamma_0) - G_M(\gamma_0))/G_L(\gamma_0)$, represents a measure of the elastic nonlinearity [79]. Similarly, the minimum-strain and large-strain dynamic viscosity (η'_M and η'_L) can be used to estimate a shear-thickening index, $T_{\gamma_0} \equiv (\eta_L(\gamma_0) - \eta_M(\gamma_0))/\eta_L(\gamma_0)$. Lissajous curves like higher harmonics in FT rheology, have been proposed to give a more precise estimate of the onset of nonlinearity than $G'_1(\omega)$ [77]. Moreover, analysis of the Lissajous curves can provide evidence of strain-stiffening in biopolymer networks for which stiffening is so weak that the first harmonic does not show it [78].

In this chapter, we explore various methods to analyze the full nonlinear response of fibrin gels to a large amplitude oscillatory stress. In particular, we test the performance of nonlinearity indices obtained from FT rheology and Lissajous curves to probe the onset of strain-stiffening, and we compare their

sensitivity to that of both the first harmonic of the LAOS response and differential measurements.

5.2 EXPERIMENTS

Large amplitude oscillatory shear measurements and prestress tests (see Chapter 2 for measurement techniques) were performed on *fibrin coarse clots* (see Chapter 3 for sample preparation) with a wide range of protein concentrations (0.1-8 mg/ml). Samples were polymerized for periods of 1 to 4 hours, depending on fibrin content, to ensure that the network structure and the modulus reached steady-state. We performed LAOS experiments on a stress-controlled rheometer, where the oscillatory strain response to a sinusoidal stress was measured. Due to stress input the mathematical formalism of the various fingerprinting methods described in section II is not directly applicable to our data, since the stress decomposition assumes a strain-controlled experiment. In future, we plan to make a direct comparison of LAOS in stress and strain control. LAOS data were collected using a constant oscillation frequency of 0.5 Hz (except for the data shown in Fig. 5.3 C) and a stress amplitude that was increased logarithmically until sample breakage. The time-dependent sinusoidal stress and strain response were measured using RheoPlus software (Anton Paar, version 3.31). Lissajous curves (normalized by the maximum stress and maximum strain) were constructed based on a single oscillation. At the beginning of each sinusoidal cycle, several oscillations were applied to ensure a steady-state strain response.

5.3 RESULTS

5.3.1 NONLINEAR ELASTICITY PROBED BY LAOS AND PRESTRESS TESTS

To quantify the nonlinear behavior of fibrin networks, we used the LAOS technique and compared the results with data obtained by the prestress method. All fibrin networks were homogenous and isotropic, and their mesh size decreased with increasing protein content (image panel in Fig. 5.2). In oscillatory measurements with increasing stress amplitude, two viscoelastic regimes were visible, as shown in the inset of Fig. 5.2 A. In the linear regime, where the applied stress is sufficiently small, the elastic and viscous moduli are independent of stress amplitude, σ . Above a critical stress value, σ_{crit} , the network stiffness increases with stress. This nonlinear stress-stiffening response is followed by sample failure at a maximum stress value, σ_{max} . The corresponding maximum strains were rather large, being of order 250%. This is typical of fibrin gels, and reflects their extraordinary extensibility [232, 44, 239, 43]. Stress-stiffening occurred over the entire range of fibrin concentrations, but the extent of stiffening depended on protein content. Dilute networks stiffened more (relative to the initial, linear modulus) than concentrated networks Fig. 5.2 A.

Prestress measurements also revealed a linear and nonlinear elastic regime (Fig. 5.2 B). However, the stress dependence of the differential elastic modu-

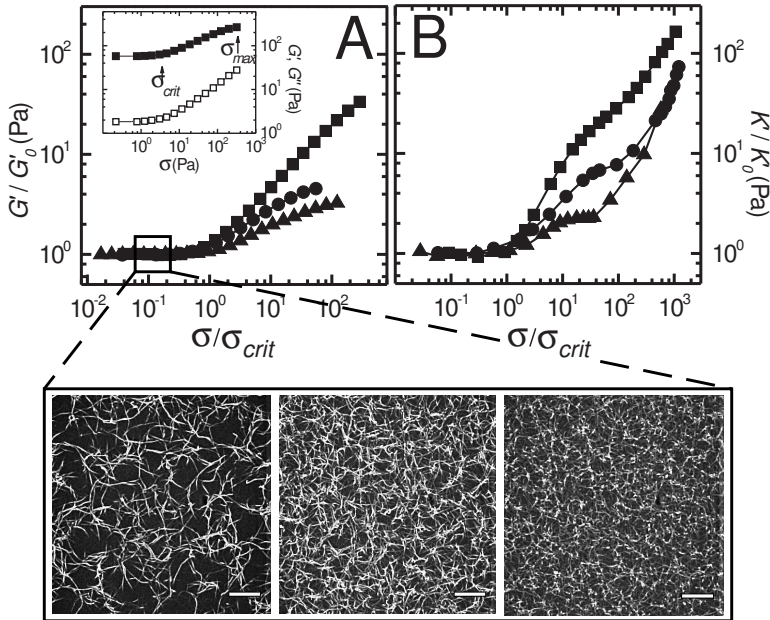


FIGURE 5.2. Nonlinear elastic response of fibrin networks subjected to either oscillatory or steady shear. Elastic moduli are normalized by the linear modulus and the stress is normalized by the critical stress value at the onset of nonlinearity. Symbols correspond to 0.5 mg/ml (squares), 2 mg/ml (circles) and 5 mg/ml (triangles) fibrin networks. (A) Elastic response to an oscillatory stress (LAOS test). (*Inset*): Non-normalized storage (solid symbols) and loss (open symbols) moduli as a function of non-normalized stress amplitude for a 2 mg/ml fibrin network. The moduli are constant at small stresses up to a critical value, σ_{crit} , and increase thereafter. (B) Differential elastic modulus as a function of applied prestress. Image panel shows maximum intensity projections of z-stacks of the corresponding fibrin networks over a $10\ \mu\text{m}$ depth with $0.1\ \mu\text{m}$ steps between confocal planes. Scale bars, $10\ \mu\text{m}$.

lus in the nonlinear regime was more complex than for G' , and concentration dependent. The stiffness showed an initial fast rise above the critical stress, followed by a slower rise or even a distinct plateau (for 5 mg/ml), and yet another fast rise till sample ruptured. Similar to the LAOS tests, the degree of stiffening was higher for dilute gels than for dense gels. Strikingly, the prestress tests show a 10-fold larger degree of stiffening than the LAOS tests. Also, the maximum stress normalized by the critical stress was somewhat larger in prestress tests. This difference may be caused by an underestimation of the LAOS analysis, which does not account for higher harmonic terms in the strain response in the calculation of the viscoelastic moduli.

5.3.2 DECOMPOSITION OF THE TIME-DEPENDENT OSCILLATORY STRAIN RESPONSE

The calculation of the viscoelastic shear moduli, G' and G'' , from a LAOS test assumes that the strain response to the applied sinusoidal stress is also sinusoidal. However, inspection of the strain response in the nonlinear regime shows deviation from sinusoidal shape (Fig. 5.3 A). The nonlinear distortion in the response becomes more evident when σ is plotted versus γ in a Lissajous plot (Fig. 5.3 B). For a viscoelastic material, the Lissajous plot in the linear regime has an ellipsoidal shape whose enclosed area is a measure of the viscously dissipated energy in an oscillation cycle. In the nonlinear regime, the ellipsoidal shape is generally distorted for soft materials, and the enclosed area often increases with increasing stress [93]. The nonlinearity in the strain response is also evident in the Fourier transformed strain response. In the linear regime, only one harmonic at the fundamental frequency is visible (inset of Fig. 5.3 C), whereas in the nonlinear regime numerous peaks corresponding to higher order harmonics appear (Fig. 5.3 C).

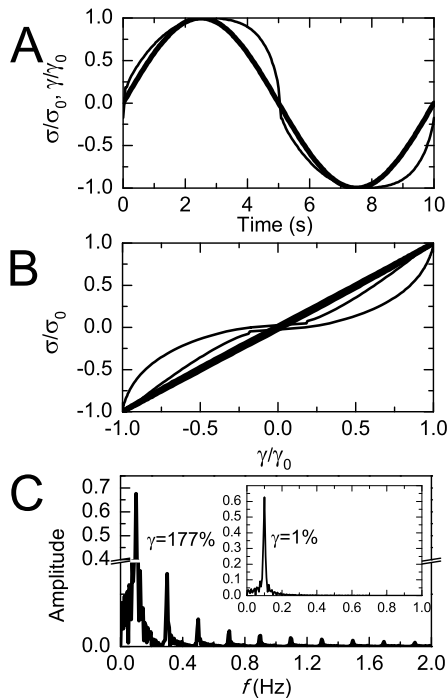
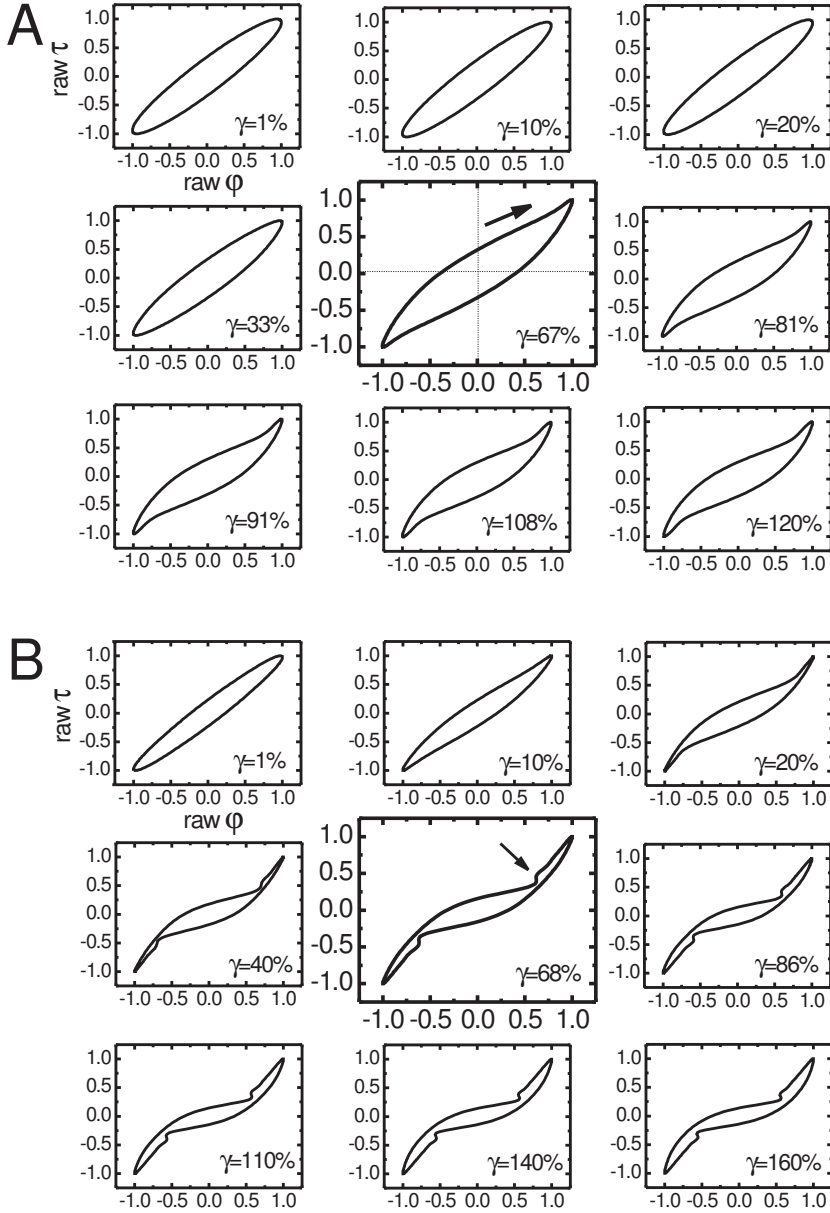


FIGURE 5.3. Oscillatory strain response upon application of a sinusoidal stress in the linear regime (thick line, strain amplitude $\gamma_0 = 1\%$) and in the nonlinear regime (thin line, $\gamma_0 = 177\%$). Plots show data in the time domain (A), corresponding Lissajous plots (B), and FT spectra recorded with an oscillation frequency of 0.1 Hz (C). Curves are normalized by the maximum amplitude of the oscillatory signal.

It has been shown that the shape of the Lissajous curves can provide additional information about the material properties in the nonlinear regime. For fibrin networks, the shape of the Lissajous curves depends on strain amplitude as well as on protein concentration. At a strain amplitude of 1%, the Lissajous curves for all fibrin gels have an elliptical shape (Fig. 5.4, A-0.2 mg/ml, B-1 mg/ml and C-5 mg/ml). However, the area enclosed by the Lissajous curve decreases with increasing protein concentration. Fibrin networks of 5 mg/ml are nearly perfect elastic solids, with a Lissajous curve that is almost a straight line. As the strain amplitude increases, the Lissajous curves start to deviate from an elliptical shape, indicating a crossover from linear to nonlinear behavior. Following the Lissajous curve clockwise and starting at zero strain (Fig. 5.4 A, $\gamma=67\%$), stress increases with strain. The slope of the Lissajous curve increases however more rapidly when the strain approaches its maximum value in the cycle. When the strain starts to decrease back to zero, the stress decreases to zero as well, after which the other half of the cycle starts, with negative stress and strain. The critical strain amplitude at the onset of stress-stiffening behavior depends on fibrin concentration. The denser the network, the lower is the strain required to enter the nonlinear regime. The Lissajous curves show a marked inflection for gels of 1 and 5 mg/ml fibrin, where the stress rises rapidly at a constant strain (arrow in Fig. 5.4 B, $\gamma=68\%$). This feature is seen for all fibrin concentrations above 1 mg/ml in the high strain regime.

The area enclosed by the Lissajous curve (calculated with stress and strain in dimensional form) is a measure of the energy per unit volume, E_d , that is dissipated by viscous flow. This energy can be directly related to the loss modulus, $E_d = \pi\gamma_0^2 G_1''$. An increase in applied stress causes an increase in E_d as evident from the increase in the area enclosed by the Lissajous curves (Fig. 5.5). For all fibrin networks, E_d increases as γ^2 up to a strain amplitude of 10%, after which it increases more rapidly with strain (with a power-law exponent of 4.4) until sample breakage at the maximum strain (inset in Fig. 5.5). This strain dependence of the E_d is in line with the stress dependence of G'' , which is constant at small stresses and increases nonlinearly with stress above σ_{crit} (inset of Fig. 5.2 A). The increase in dissipated energy relative to the linear regime varies between 10^5 - 10^6 and does not show a clear concentration dependence, in contrast to the relative degree of elastic stiffening, which decreases with concentration (Fig. 5.2 A).



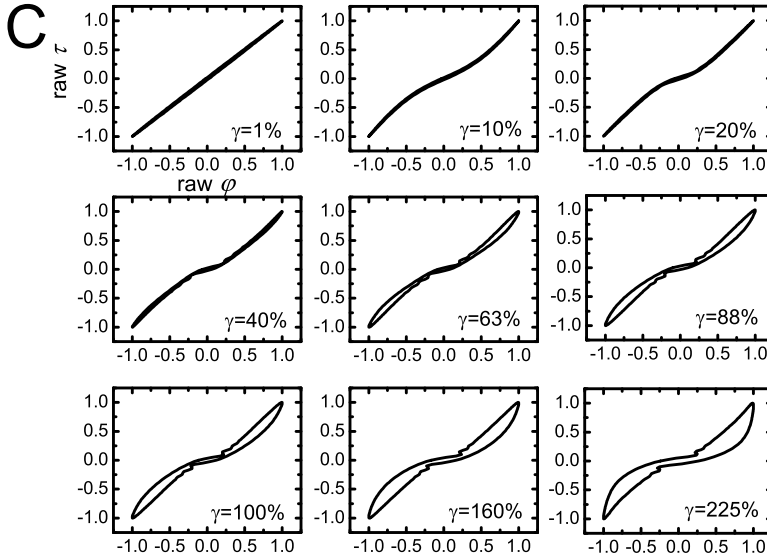


FIGURE 5.4. Changes in the shape of Lissajous curves with increasing strain amplitude for 0.2 (A), 1 (B) and 5 mg/ml (C) fibrin networks.

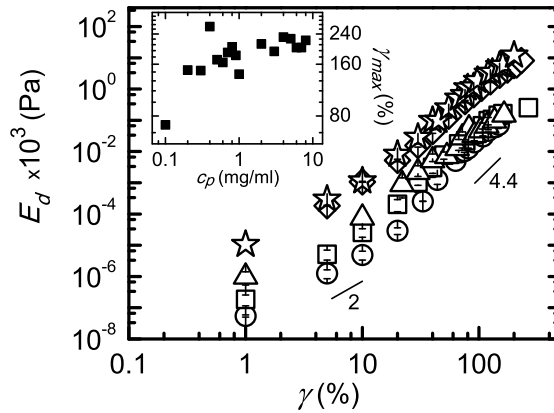


FIGURE 5.5. Dissipated energy calculated from the area enclosed by Lissajous curves for fibrin networks of different concentrations: 0.2 (circles), 0.4 (squares), 0.6 (triangles), 4 (diamonds) and 7 mg/ml (stars). (Inset): Maximum strain amplitude where networks rupture as a function of protein concentration.

A different way to analyze nonlinearities in the material response is to quantify the intensities of higher harmonics in the Fourier spectrum of the strain response. The FT spectra for all fibrin concentrations show an increasing number of higher harmonics peaks and the increase in peaks intensities with increasing strain amplitude (Fig. 5.6). Since the stress has odd symmetry with respect to the strain, only odd harmonics are visible (inset in Fig. 5.6). The intensity of the higher harmonics has been predicted to decrease as $1/n^2$ for strain-hardening materials [159]. For the fibrin networks, we observe a somewhat weaker scaling of I_n/I_1 with n (power-law exponent -1.7) for the first 10 harmonics, and a stronger n -dependence for higher order harmonics.

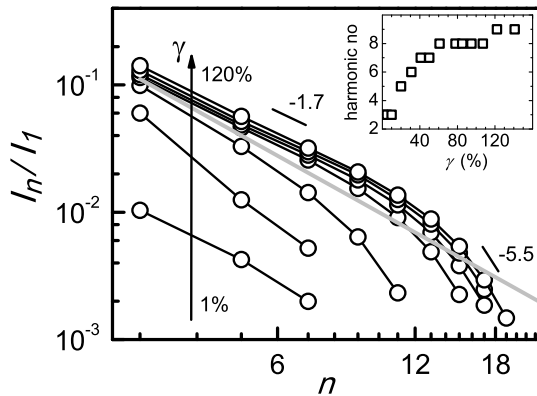


FIGURE 5.6. Contribution of higher harmonics to the nonlinear LAOS response of a 2 mg/ml fibrin network. With increasing strain amplitude (vertical arrow), the intensity I_n of the higher harmonic contributions (normalized by the first harmonic, I_1) increases, and more and more higher harmonic peaks are detected. The gray solid line corresponds to the predicted $1/n^2$ scaling for strain-stiffening materials [159]. (Inset): The number of higher harmonics detected as a function of strain amplitude.

Both FT spectra and Lissajous plots can be used to identify the strain amplitude where nonlinearity first sets in [312]. For the FT spectra, one can define a nonlinearity parameter, S , either as the amplitude of the third harmonic relative to the first, $\sum_{FT3} = I_{3\omega}/I_{1\omega}$ or as the sum of amplitudes of all higher harmonics normalized by the first, $S_{FT\Sigma} = \sum_{n=3}^{\infty} I_{n\omega}/I_{1\omega}$. As shown in Fig. 5.7 A, both nonlinearity parameters (up and down triangles) show onset of nonlinearity at the same strain amplitude, which is 1% for a 2 mg/ml fibrin network. For the Lissajous curves, the strain-stiffening index, $S(\gamma_0) \equiv (G_L(\gamma_0) - G_M(\gamma_0))/G_L(\gamma_0)$, where G'_M is the slope of the Lissajous curve at zero strain and G'_L is the ratio of stress and strain at maximum strain. The Lissajous index (circles) is less sensitive to the onset of nonlinearity than the FT spectra, and it is even somewhat less sensitive than the first harmonic modulus, $S_{LAOS} = G'(\gamma)/G_0(\gamma)$ (squares).

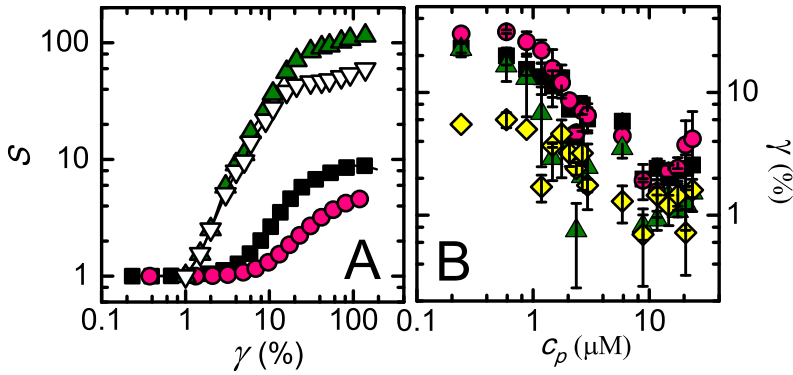


FIGURE 5.7. Nonlinearity parameters for a 2 mg/ml fibrin network plotted against strain amplitude, calculated from three different methods: the first harmonic elastic modulus extracted directly from the stress-stiffening curve, $S_{LAOS} = G'(\gamma)/G_0(\gamma)$ (squares), the elastic stiffening ratio calculated from Lissajous curves, $S_{Lissajous} = L(\gamma_0)/M(\gamma_0)$ (circles), the sum of the amplitudes of higher harmonics in the FT spectrum, $S_{FT\Sigma} = \sum_{n=3}^{\infty} I_{n\omega} / I_{1\omega}$ (up triangles) and the amplitude of the third harmonic in the FT spectrum, $S_{FT3} = I_{3\omega} / I_{1\omega}$ (down triangles), respectively, each normalized by the first harmonic. (B) Concentration dependence of the critical strain obtained from LAOS strain-stiffening curves (black squares), prestress measurements (yellow diamonds), and from $S_{Lissajous}$ (red circles) and S_{FT} (green up triangles).

The critical strain, γ_{crit} , extracted from the dependence of all different stiffening indexes on the strain amplitude decreases about 10-fold as the fibrin concentration increases from 0.2 to 10 μM , and saturating to a constant level above 10 μM (which corresponds to 3 mg/ml) (Fig. 5.7 B). This implies an earlier onset of strain-stiffening with increasing fibrin concentration, in accordance with the earlier onset of non-ellipsoidal Lissajous curves (Fig. 5.4). The critical strain extracted from LAOS tests and the strain-stiffening index for the Lissajous curves decreases from 20 to 2%. The γ_{crit} extracted from the higher harmonics in FT spectra is 2-fold smaller, indicating a higher sensitivity to the onset of nonlinearity. The FT spectra yield critical strain values which are in rather good agreement with the critical strain measured by the prestress method (yellow diamonds in Fig. 5.7 B). Interestingly, the sum of the amplitudes of higher harmonics also shows a similar strain-dependence as the differential elastic modulus, $K'(\gamma)$, on fibrin concentration (Fig. 5.8). $S_{FT\Sigma}$ is constant, rises above the critical strain, and then shows a slower rise for more dilute gels (squares: 0.5 mg/ml, circles: 2 mg/ml) or even a distinct plateau for denser gels (triangles: 5 mg/ml) followed by a further rise in stiffness. This complex strain dependence may have the same origin as the analogous strain-dependence of $K'(\gamma)$ shown in Fig. 5.2 B, which was ascribed to nonlinear stretching of the fiber backbones. However, $S_{FT\Sigma}$ has no clear physical interpretation, unlike $K'(\gamma)$.

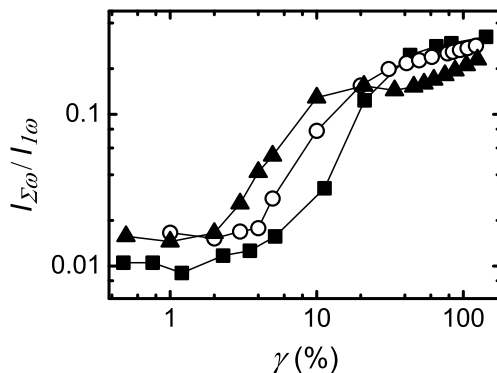


FIGURE 5.8. Dependence of the sum of the amplitudes of higher harmonics, $S_{FT\Sigma} = \sum_{n=3}^{\infty} I_{\Sigma\omega} / I_{1\omega}$ on strain amplitude for 0.5 (squares), 2 (circles) and 5 mg/ml (triangles) fibrin networks.

5.4 DISCUSSION AND CONCLUDING REMARKS

Large amplitude oscillatory shear is a popular method to probe the response of soft materials to large shear deformations. Soft materials tend to exhibit a highly nonlinear viscoelastic response, which is reflected in a highly non-sinusoidal stress (or strain) response to an applied sinusoidal strain (or stress).

In this chapter we examined the information stored in the non-sinusoidal strain response of fibrin gels to an applied oscillatory stress. We first looked at the nonlinear response of the elastic shear modulus, G' , which represents the first harmonic in the strain response. We found that the first harmonic strongly underestimates the nonlinearity of fibrin gels. This is especially obvious when comparing the stress-stiffening behavior of fibrin networks obtained from LAOS tests with the stiffening measured by the prestress method (Fig. 5.2). Pre-stressing the sample has the advantage of allowing locally linear measurements even at high stress, thus providing more accurate measurements of the moduli in the nonlinear regime. Moreover, we observed that the differential elastic modulus, K' , shows a richer dependence on stress than G' , revealing three distinct regimes in the nonlinear response. As explained in Chapter 3, these regimes can be ascribed to distinct structural levels at which fibrin gels deform. This richness is lost in the LAOS data, where a continuous increase in G' with strain is observed till the network ruptures. However, the full nonlinear response in LAOS captured in the form of a FT spectrum of the strain response does show a similar, complex stress-dependence as the differential modulus (Fig. 5.8). Moreover, the full nonlinear response provides a more sensitive measure of the onset of nonlinearity than the first harmonic modulus. The FT spectra show comparable values for the critical strain as prestress measurements (Fig. 5.7 B). These observations indicate that a full characterization of the nonlinearity of

fibrin networks with LAOS requires a consideration of the higher harmonic contributions in the rheological response.

The Lissajous curves for fibrin networks in the nonlinear regime show complex shapes, which strongly deviate from the ellipsoidal shape in the linear regime. The curves show clear evidence for strain-stiffening in the form of a steep rise in stress at high strain. Similar behavior was previously reported for strain-stiffening actin networks [320, 293, 265]. However, in fibrin networks Lissajous curves show unique for this biopolymer stress shape at high protein concentrations with the characteristic inflections, which, to the best of our knowledge, have not been reported for other soft materials. It is unclear whether these inflections reflect some intrinsic material property related to the hierarchical structure of fibrin, or perhaps some form of elastic coupling, similar to creep ringing [326]. For polymer solutions, changes in the shape of Lissajous curves were previously shown to be indicative of shear-induced changes in the microstructure [145]. To resolve this question for fibrin, it will be interesting to check the influence of bundle size of the fibrin fibers on the shape of the Lissajous curves. If the inflections are related to the internal structure of protofibril bundles, then a reduced bundle size should affect the Lissajous curve shape.

The FT rheology and Lissajous curves provided in this chapter consider the total stress, which is a sum of elastic and viscous stresses. In future, it will be interesting to decompose the strain response into elastic and viscous contributions, to achieve a more physically meaningful interpretation of the data [79]. Moreover, a comparison needs to be made between LAOS performed in stress and strain control. In this way, LAOS analysis may eventually provide a fingerprint of the nonlinear rheology of fibrin gels (in the form Chebyshev coefficient) that is complementary to prestress experiments.

I would like to thank Baldomero Alonso-Latorre for discussions and for performing additional LAOS tests on fibrin clots; Marco Seynen for writing a software program to record and analyze the raw data from the rheometer with high sampling rate (unfortunately not used here); and Hincó Schoenmaker for the enormously valuable technical assistance.

6 MOLECULAR COMPOSITION INFLUENCES COLLAGEN GEL MECHANICS

COLLAGEN fibrils are the main structural element of connective tissues. In many tissues, these fibrils contain two fibrillar collagens (types I and V) in a ratio that changes during tissue development, regeneration, and various diseases. Here we investigate the influence of collagen composition on the structure and rheology of networks of purified collagen I and V, combining fluorescence and atomic force microscopy, turbidimetry, and rheometry. We demonstrate that the network stiffness strongly decreases with increasing collagen V content, even though the network structure does not substantially change. We compared the rheological data with theoretical models for rigid polymers and found that the elasticity is dominated by nonaffine deformations. There is no analytical theory describing this regime, hampering a quantitative interpretation of the influence of collagen V. Our findings are relevant for understanding molecular origins of tissue biomechanics and for guiding rational design of collagenous biomaterials for biomedical applications.

I.K. Piechocka, A.S.G. van Oosten, R.G.M. Breuls, G.H. Koenderink
Rheology of heterotypic collagen networks
Biomacromolecules **12**: 2797-805 (2011)

6.1 INTRODUCTION

Collagen is the main constituent of the extracellular matrix (ECM) of animal connective tissues [36]. Collagen forms elastic networks of fibrils that confer superior tensile strength. Moreover, the mechanical properties of collagen influence the behavior of cells within tissues [19, 115]. The biophysical mechanisms underlying the remarkable tensile strength of collagen have been studied extensively using fibrils isolated from tissue or reconstituted from purified collagen. Collagen fibers are rather stiff polymers with a Young's modulus in the range of 1-800 MPa in the hydrated state [273, 321, 105, 296, 271]. They form viscoelastic networks with elastic shear moduli in the range of 1-200 Pa, dependent on pH, ionic strength, and temperature [297, 156, 322, 282, 283, 243, 323, 8]. When strained, collagen gels tend to stiffen, which may serve as a mechanism to protect tissues against excessive deformation [156, 294, 285, 282, 283, 8].

Previous biophysical research has largely focused on networks of purified collagen I, the most abundant type of collagen in non-cartilaginous tissues. However, *in vivo* collagen I usually forms heterotypic fibrils together with collagen type II [122], III [251, 168, 287], or V [26, 186, 29, 185]. This co-assembly is thought to provide a mechanism for regulating fibril diameter. This view is mainly based on studies of collagen I and V, which form heterotypic fibrils whose diameter decreases with increasing collagen V content [86, 26, 3, 28, 56, 206]. In tissues, a similar inverse dependence of fibril diameter on collagen V content is observed. In most adult tissues, collagen fibrils contain only 2-5% collagen V and have a broad distribution of diameters in the range of 40-200 nm [202]. In the cornea, however, heterotypic fibrils contain 15-25% collagen V and have a uniform diameter of only 25-34 nm [202, 27, 139]. Several human connective tissue disorders such as Ehlers-Danlos syndrome are associated with increased collagen V content, indicating that a correct stoichiometry of collagen I and V is critical for normal tissue [56, 197, 7, 308]. Moreover, several other pathological conditions such as tumors, atherosclerotic plaques, and scars are also associated with increased levels of collagen V [35].

The effect of collagen V on the mechanical behavior of collagenous materials is unknown. The aim of our work was to study this effect in a model system of purified collagen I and V. The formation process of the heterotypic fibrils is relatively well understood. The building block of collagen fibrils is the *tropocollagen* molecule, a coiled triple helix composed of three α -chains. At 37°C and under appropriate buffer conditions (neutral pH, appropriate ionic strength, and presence of phosphate), purified tropocollagen spontaneously assembles into fibrils [317, 315]. Specific, non-covalent interactions lead to a precise axial stagger of each molecule by one-quarter of its length relative to its neighbor, giving the fibers a banding pattern with a periodicity of 67 nm in electron microscopy [230, 225]. This periodicity remains the same when collagen V is present [29, 3, 56, 184]. Several mechanisms have been proposed to account for diameter regulation by collagen V. Collagen is first synthesized as procollagen, which is enzymatically processed to collagen by cleavage of N- and C-terminal propeptides. In contrast to collagen I, collagen V retains a long (~17 nm) part of its N-propeptide. The collagen V helix is buried inside the

fibrils, but the N-propeptide extends outward through the gap zones of the quarter-staggered array. The exposed domains may limit lateral growth of fibrils by steric or electrostatic hindrance of monomer addition [28, 184, 56]. Yet, the diameter-limiting effect is still partly present when the N-propeptide is removed with pepsin, suggesting an influence of the collagen V helix on diameter regulation [3, 28, 56, 206]. The longer length of the type V helix compared to the type I helix (321 nm versus 299 nm) could make molecular packing less regular [272], or the larger amount of glycosylated hydroxylysine residues in collagen V may limit lateral growth [206].

In this chapter rheological measurements on collagen networks reconstituted from purified type I and V collagen will be presented. We varied the total collagen concentration and the composition of the networks. The microstructure of the pure and hybrid collagen networks was examined by fluorescence microscopy and the morphology of the fibrils by atomic force microscopy (AFM) and turbidimetry. We compare the rheological measurements with theoretical models of stiff polymers in an effort to uncover the physical origin of collagen V's influence on the rheology of hybrid collagen networks.

6.2 SAMPLE PREPARATION

Rat tail collagen I in 0.02 N acetic acid solution (with telopeptides) was purchased from BD Biosciences (Franklin Lakes, NJ). Lyophilized collagen V from human placenta was obtained from Sigma-Aldrich (St. Louis, MO) and dissolved in 0.02 M acetic acid at 4 °C for 24 hours. This collagen V was pepsin-treated and thus lacked telopeptides, consistent with most prior studies of collagen structure and cell physiology in the presence of collagen V. Hybrid collagen networks were prepared from mixed stock solutions having collagen V contents of 0, 10, 20, 50, 80, and 100 wt%. Samples with a final volume of 300 μ l and total collagen concentration of 0.5-5 mg/ml were prepared on ice by diluting collagen with 30 μ l Minimal Essential Medium (MEM 10X, Gibco BRL, Paisley, Scotland) and water, and adjusting the pH to 7.3 with sodium hydroxide (Sigma-Aldrich) within 4 minutes to prevent premature polymerization [216]. MEM has a near-physiological ionic strength and pH and contains 1 mM phosphate, thus promoting formation of fibrils with a native D-banding pattern, as verified by AFM imaging.

For fluorescence microscopy, collagen was mixed on ice in a molar ratio of 7:1 with CNA35 [162], a bacterial collagen-binding protein with molecular weight of 35 kDa [261]. The CNA35 protein was labeled with Oregon Green and was a kind gift from dr. M. Merckx (TU Eindhoven, Netherlands). We checked by confocal microscopy on collagen networks with varying collagen/CNA35 molar ratio that the CNA35 protein did not affect collagen network structure. Moreover, collagen networks with CNA35 looked identical to unlabeled networks in bright field microscopy. The collagen solution was gelled at 37 °C in a glass microchamber, which was sealed to prevent solvent evaporation and imaged as described in Chapter 2.

6.3 RESULTS

6.3.1 RHEOLOGY OF MIXED COLLAGEN I/V NETWORKS

Hybrid networks of collagen type I and V were polymerized between the plates of a rheometer as described in Chapter 2, using a steel cone (40 mm diameter, 1 degree angle, 49 μm truncation) and bottom plate. Rheology results were the same in parallel plate geometries with various gap sizes, indicating no-slip conditions. The time dependence of the shear moduli during polymerization is shown in Fig. 6.1 A, for samples with a fixed total collagen concentration of 2 mg/ml but varying collagen V content. For all compositions studied, the shear moduli began to increase immediately after initiation of collagen polymerization by heating to 37 °C, with no detectable lag phase. From the onset, the elastic modulus was larger than the viscous modulus (inset of Fig. 6.1 A), suggesting that a space-spanning, elastic network was formed within 30 s. Polymerization was also evident from an immediate rise in gel turbidity (Fig. 6.1 B). The elastic modulus continued to rise slowly for at least 15 hours, but after 3 hours the increase was less than 10% over a 12 hour window. Therefore we decided to perform all rheological tests after 3 hours of polymerization (arrow in inset of Figure 6.1 A).

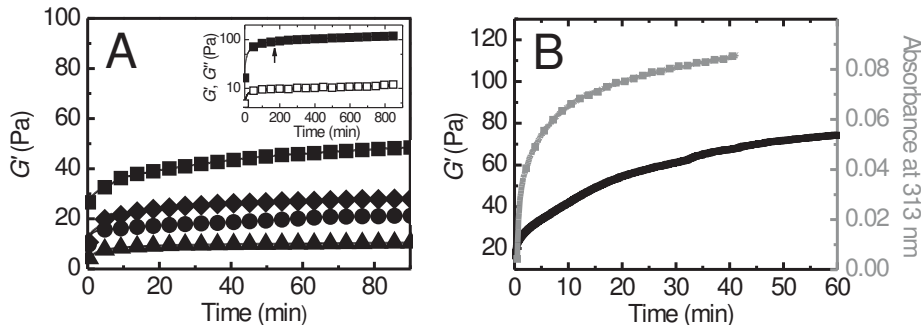


FIGURE 6.1. Polymerization behavior of collagen networks. (A) Time dependence of the elastic modulus of collagen solutions heated to 37 °C inside the rheometer with varying proportions of type I and V and a fixed total collagen concentration of 2 mg/ml. Symbols denote weight/weight ratios of collagen I to collagen V: 100/0 (squares), 90/10 (diamonds), 80/20 (circles) and 0/100 (triangles). *Inset*: Elastic (solid squares) and viscous (open squares) shear moduli for 3.5 mg/ml collagen type I gel. (B) Network polymerization monitored by rheology (black line) and turbidimetry (red line) for 3.5 mg/ml collagen type I gel.

Incorporation of collagen V substantially decreased the final gel stiffness. Pure collagen I networks of 2 mg/ml had an average stiffness of 45 Pa while pure collagen V networks had a 10-fold lower stiffness of 4 Pa ($p < 0.01$). The mixed networks had intermediate values of G' (Fig. 6.2 A). Addition of up to 20% collagen V caused a continuous decrease in G' , whereas G'' remained

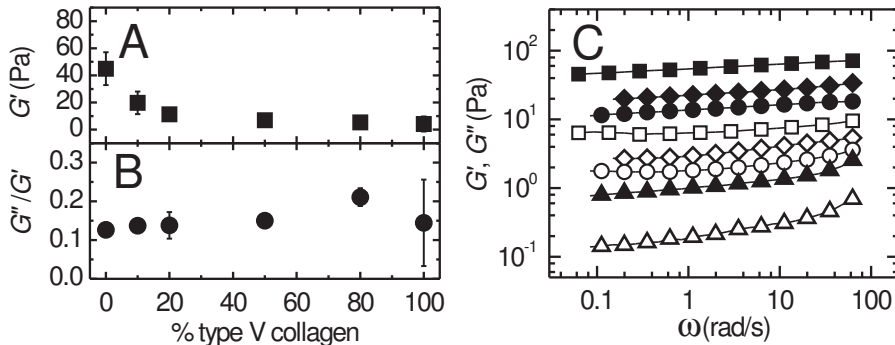


FIGURE 6.2. Effect of collagen type V percentage on the linear viscoelastic behavior of mixed collagen I/V networks at a fixed, total collagen concentration of 2 mg/ml. (A) Elastic modulus as a function of weight percentage collagen type V. (B) Corresponding loss tangent. (C) Frequency dependence of the linear elastic (closed symbols) and viscous (open symbols) shear moduli for collagen networks with varying collagen type I and V composition and a fixed total collagen concentration of 2 mg/ml. Symbols denote weight/weight ratios of 100/0 (squares), 90/10 (diamonds), 80/20 (circles), 0/100 (triangles). Data are presented as average \pm SD with $n=3$. Means were compared using unpaired Student's *t*-tests).

constant for larger collagen V contents (Fig. 6.2 A). The loss tangent, G''/G' , was around 0.13, independent of collagen V content (Fig. 6.2 B). Incorporation of collagen V did not influence the dynamics of stress relaxation in the collagen networks. G' was weakly dependent on frequency according to a power-law with an exponent of ~ 0.1 for all collagen compositions (Fig. 6.2 C). This type of behavior is typical for (bio)polymer gels that are transiently crosslinked by noncovalent interactions [297].

We next compared the dependence of the shear moduli on total collagen concentration for pure collagen I and hybrid collagen I/V (80/20) gels. In both cases, the stiffness increased when the concentration was raised from 0.5 to 3 mg/ml, but it saturated above 3 mg/ml to a value of 100 Pa for collagen I and 55 Pa for collagen I/V (Fig. 6.3 A). This saturation was not caused by incomplete fibrillization; concentration measurements on supernatants collected after precipitation of the fibrils by centrifugation showed less than 7% nonfibrillated collagen for all collagen concentrations (Fig. 6.4). The elastic moduli of pure collagen I networks are comparable to prior reports for rat tail collagen [243, 8] and pepsinized bovine skin collagen [297, 156, 322, 282, 283, 323, 294]. At the same total collagen concentration, the hybrid networks were always about 3-fold softer than pure collagen I networks (Fig. 6.3 C). The loss tangents of hybrid gels was similar to that of pure collagen I gels up to 3 mg/ml collagen, while at higher concentrations it was somewhat larger ($p < 0.05$, Fig. 6.3 B).

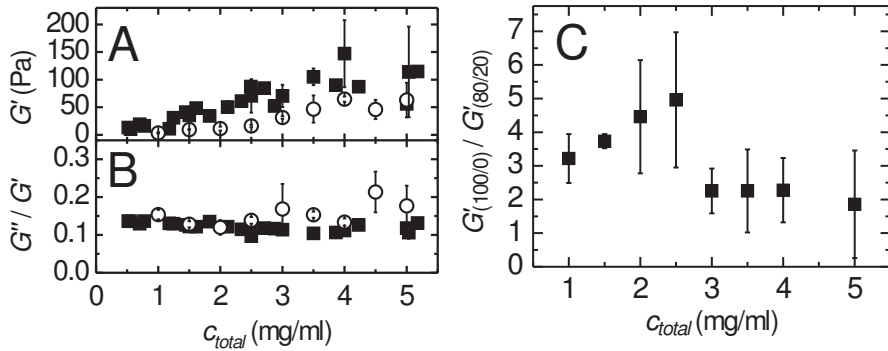


FIGURE 6.3. Effect of collagen V addition on the linear viscoelastic behavior of collagen networks. (A) Elastic moduli for pure type I collagen networks (solid squares) and mixed 80/20 collagen type I/V networks (open circles) as a function of total collagen concentration. (B) Corresponding loss tangents. (C) Ratio of the linear elastic modulus, G_0 , of collagen 100/0 and 80/20 as a function of total collagen concentration.

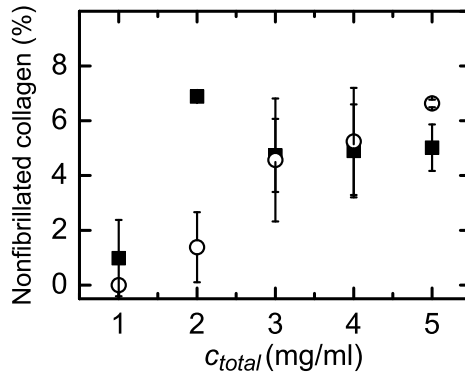


FIGURE 6.4. Percentage of nonfibrillated collagen versus total collagen concentration for type I (solid squares) and hybrid 80/20 collagen gels (open circles).

To assess whether collagen V affects the nonlinear elastic response of collagen networks, we subjected the gels to large amplitude oscillatory shear. Both collagen I networks and hybrid collagen I/V networks (80/20) stiffened up to collagen concentrations of 2 mg/ml and weakened at higher concentrations (Fig. 6.5 A), although the hybrid networks were overall softer. The critical strain where strain-stiffening set in for dilute gels was ca. 17% for both homotypic and heterotypic networks (Fig. 6.5 B). Consistent with prior reports for pepsinized collagen I [294], the critical strain was insensitive to collagen concentration. However, the pepsinized collagen gels stiffened over a concen-

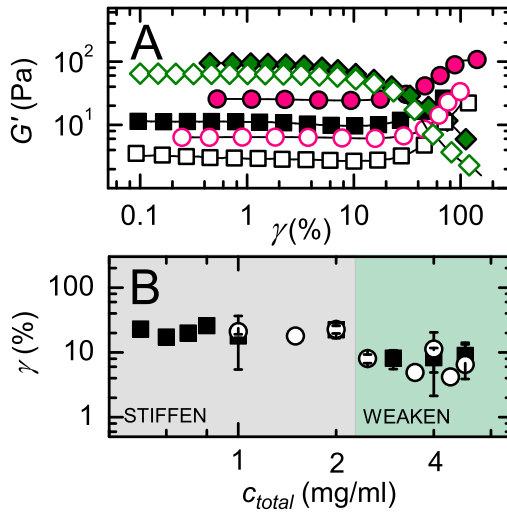


FIGURE 6.5. Effect of collagen V addition on the nonlinear rheology of collagen networks. (A) Both pure type I collagen networks (solid symbols) and hybrid 80/20 type I/V networks (open symbols) strain-stiffen for collagen concentrations of 1 mg/ml (black squares) and 2 mg/ml (pink circles), while they strain-weaken for larger collagen concentrations (green diamonds: 4 mg/ml). (B) Dependence of critical strain (onset of strain-stiffening, grey-colored area) and yield strain (onset of strain-weakening, green-colored area) on total collagen concentration for collagen I networks (solid squares) and hybrid collagen I/V networks (open circles).

tration range of 0.5-5 mg/ml, whereas rat tail collagen I gels studied here strain-weakened above 2 mg/ml. The yield strain characterizing the onset of strain-weakening was independent of collagen concentration, being around 8% for both homotypic and heterotypic gels (Fig. 6.5 B).

6.3.2 COLLAGEN NETWORK MICROSTRUCTURE

To investigate whether the effect of collagen V on collagen rheology is accompanied by structural changes on the network scale, we performed fluorescence confocal microscopy. Figure 6.6 (top panels) shows representative images of hybrid networks with varying mixing ratio but a fixed total collagen concentration of 2 mg/ml. The networks were rather homogeneous and isotropic for all collagen I/V ratios. Networks with 50% or 100% collagen V appeared to have somewhat larger open spaces than networks with 20% or less collagen V. This observation was confirmed by considering the average mesh size of the networks obtained by thresholding the images and measuring the distribution of distances between on-pixels (corresponding to detected fibers) [20]. For collagen gels containing predominantly collagen I (80-100%), the average mesh size was 3 μm . Networks containing 50% collagen V had an increased average mesh size of 4 μm , and networks composed of 100% collagen V had an even

larger average mesh size of 7 μm . To test whether collagen V affects the network structure at the fiber scale, we also performed atomic force microscopy (AFM) on 10x10 μm and 3x3 μm areas (Fig. 6.6, middle and bottom rows of images). The collagen fibers were smooth and appeared unbranched. Images of hybrid networks showed evidence of loose association of some of the fibrils into twisted bundles (white arrows in Fig. 6.6). Fibrils of pure type V collagen were thinner than the collagen I-containing fibers. Moreover, they were shorter, with a typical length of only 1 μm . In contrast, collagen I-containing fibers were too long to recognize both ends in 10x10 μm or 3x3 μm areas.

Pure collagen I and hybrid collagen I/V networks both displayed two distinct concentration regimes. They looked rather inhomogeneous with dense collagen areas interspersed with large open spaces at concentrations below 1 mg/ml, whereas they were more homogeneous above 2 mg/ml (Fig. 6.7, upper panels). In both concentration regimes, pure collagen I networks and hybrid networks of the same concentration looked comparable, indicating that collagen V did not substantially affect the network structure.

6.3.3 QUANTIFICATION OF FIBRIL DIAMETER

To quantify the effect of collagen V on fibril diameter, we performed light scattering measurements with turbidimetry as described in Chapter 2. The advantage of this approach is that it noninvasively measures the diameter and mass/length ratio of fibers in their hydrated state [52]. The average fiber mass/length ratio substantially decreased upon increasing the collagen V content from 0 to 100% (Fig. 6.6 A). Pure collagen I fibers had a mass/length ratio of $1.23 \cdot 10^{13}$ Da/cm. Given a quarter-staggered axial packing of collagen molecules with a periodicity of $D = 67.2$ nm (Fig 6.9 B), the number of molecules per cross-section is $N = \mu / (M / 4.6D)$, where M is the molecular mass (290 kDa for collagen I and 352 kDa for collagen V) [139]. Pure collagen I fibers thus had close to 1200 monomers per cross-section (Fig. 6.8 A). Fibrils with 10% collagen V had a comparable mass/length ratio (N around 1700), but incorporation of 20% or more collagen V caused a reduction in μ compared to pure collagen I fibrils. Pure collagen V fibrils had a 5-fold lower mass/length ratio than pure collagen I fibrils ($p < 0.01$) with $\mu = 2.3 \cdot 10^{13}$ Da/cm and $N = 220$.

The diameter of the fibers as measured with turbidimetry also decreased with increasing collagen V content, but only weakly, going from 117 nm at 0% collagen V to 96 nm at 50% collagen V (Fig. 6.6 B). Surprisingly, the apparent diameter of pure collagen V fibrils was 157 nm, larger than that of pure collagen I fibrils. However, this diameter value is probably inaccurate because the light scattering spectra for collagen V were not well-fitted by the theoretical expression for rigid fibrils (see Chapter 2), Fig. 2.3. The reason is probably that the theoretical analysis is only valid when the fiber length exceeds 800 nm, which is close to the average length of the pure collagen V observed by AFM [327]. We note that the measured diameters for all collagen compositions are larger than expected based on the mass/length ratio assuming a close-packed lateral packing arrangement of tropocollagen monomers in the fibers. For a close-packed arrangement, the effective diameter should be $d_{eff} = 1.83\sqrt{N}$ (nm)

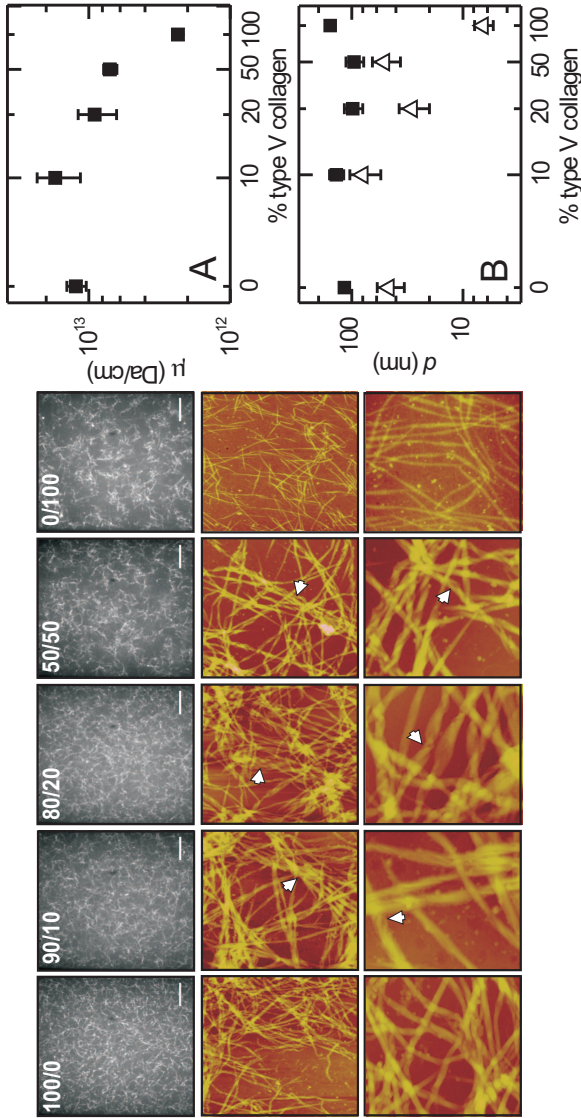


FIGURE 6.6. Effect of collagen V on network architecture and fiber structure in networks with a constant overall collagen concentration of 2 mg/ml. (*Top row of images*): Confocal micrographs of hydrated collagen networks with different collagen type V contents as indicated. The fibers are labeled with a fluorescent collagen-binding protein, AlexaFluor488-CNA35. Images represent single confocal planes. Bars, 10 μm . (*Middle row of images*): AFM images of dried collagen fibers deposited on mica, showing 10x10 μm areas. (*Bottom row of images*): AFM images of 3x3 μm areas. Arrows point to loose bundles of fibrils. (A) Fibril mass/length ratio measured with turbidimetry, versus collagen V content. (B) Fibril mass/length ratio measured with AFM (open triangles) and for dried fibrils with AFM (closed squares).

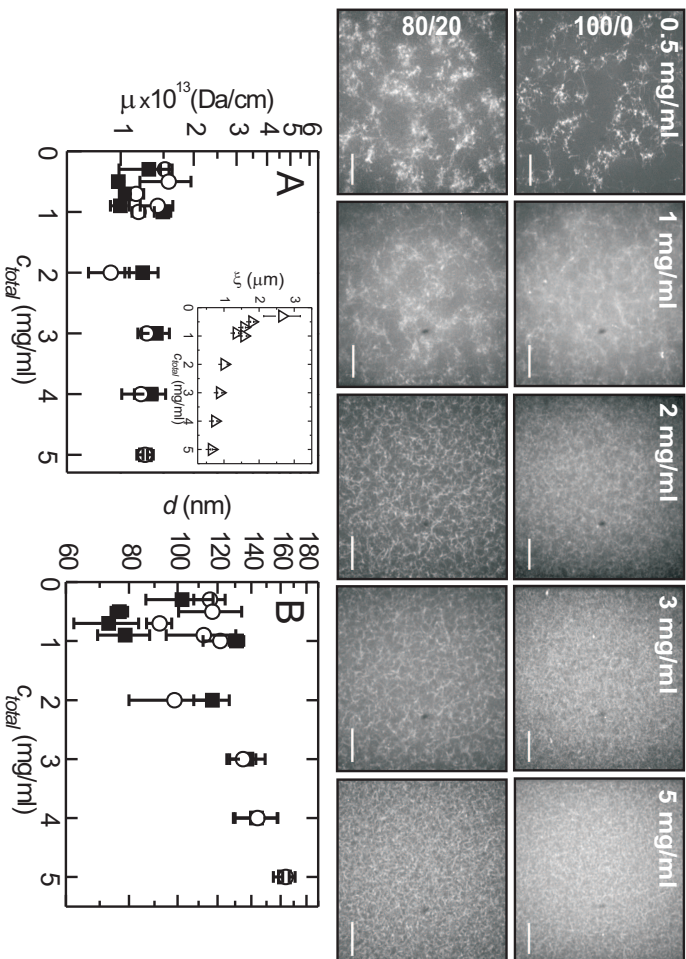


FIGURE 6.7. Effect of total collagen concentration on network architecture and fiber diameter for pure type I and hybrid (80/20) I/V collagen networks. *Top row of images:* Confocal micrographs of pure collagen I networks with concentration as indicated. *Bottom row of images:* Corresponding confocal images of hybrid collagen networks. Images are maximum intensity projections of z-stacks of 101 planes over a depth of 10 μm . Bars, 10 μm . (A) Fiber mass/length ratio and (B) diameter for pure type I networks (solid squares) and 80/20 I/V networks (open circles) measured on hydrated collagen gels by turbidimetry. Inset in (A) shows the concentration dependence of the network mesh size that is expected for pure type I collagen networks based on the known collagen mass concentration and measured fiber mass/length ratio, assuming a homogeneous fiber distribution.

[139]. Fig. 6.9 shows that the measured diameters do scale as \sqrt{N} , but the absolute values are larger than the predicted values by a factor 2. This difference suggests that the fibers are more open than regularly packed fibers, which is compatible with the loose bundling seen in the AFM images (Fig. 6.6, image panels).

For comparison, we also measured the fiber diameter from the apparent height observed by AFM (Fig. 6.6 B). In agreement with the turbidity data, AFM imaging also demonstrated a reduction in fiber diameter with increasing collagen V content, but this reduction was stronger than the reduction observed with turbidimetry. All height values were lower than the diameter values measured by turbidimetry. This may reflect shrinkage of the fibers imaged by AFM during drying. Furthermore, turbidimetry may measure a larger average diameter due to scattering contributions from bundles of collagen fibrils. For pure type V fibrils, AFM gave a substantially lower diameter value than turbidimetry, namely ~ 7 nm. Our data are consistent with prior electron microscopy (EM) studies [3, 28, 56], which reported a decrease of fiber diameter from ~ 150 nm for pure collagen I to 25-40 nm for pure collagen V. However, a direct quantitative comparison is difficult since both AFM and EM probably suffer from (different degrees of) fiber shrinkage due to drying, and since fiber bundles contribute to light scattering in a way that is difficult to model theoretically.

To evaluate the dependence of fiber diameter on collagen concentration, we performed turbidimetry on gels of varying total concentration but fixed collagen V content (0% or 20%). The average mass/length ratio of the fibrils was similar in both types of networks and did not show a clear dependence on collagen concentration. On average, the mass/length ratio was around $1.2 \cdot 10^{13}$ Da/cm (Fig. 6.7 A), corresponding to ~ 1300 molecules/cross-section (Fig. 6.8 B). The diameter of the fibrils showed two distinct concentration regimes. At low collagen concentrations (0.3-1 mg/ml), the diameter of the fibers showed large, inconsistent variations with collagen concentration (Fig. 6.7 B). The diameter varied from 76 to 130 nm for pure collagen I fibers, and from 90 to 120 nm for the hybrid fibers. These large variations may reflect the heterogeneous structure of the low-density networks visible by confocal microscopy. At high collagen concentrations (2-5 mg/ml), where the network structure is more homogeneous, the fiber diameter showed a progressive increase with increasing collagen concentration. The diameter of pure collagen I fibers increased from 117 to 163 nm, and the diameter of hybrid fibers increased from 100 to 164 nm (increases significant with $p < 0.001$). The increase in fiber diameter between 2 and 5 mg/ml collagen seems contradictory with the constant mass/length ratio in this concentration regime. A possible explanation for this apparent contradiction is lateral aggregation of the fibrils, which has also been reported in prior EM and confocal studies [323, 317]. Our turbidity measurements are consistent with loose lateral bundling, since the measured diameters are consistently larger than the values expected for fibers with a regular lateral packing (Fig. 6.9).

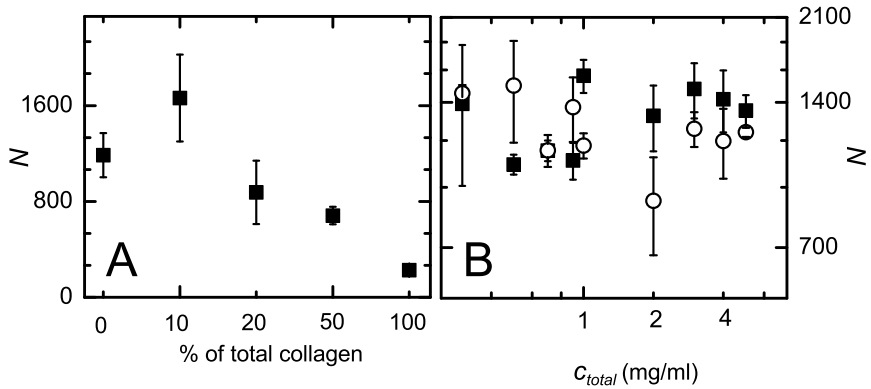


FIGURE 6.8. Number of collagen monomers per cross-section N , calculated from mass/length ratios measured by turbidimetry, assuming a D-periodic axial packing. (A) Dependence of N on collagen V content for mixed collagen I/V networks at a constant total collagen concentration of 2 mg/ml. (B) Dependence of N on total collagen concentration for pure collagen I networks (solid squares) and for mixed 80/20 collagen I/V networks (open circles).

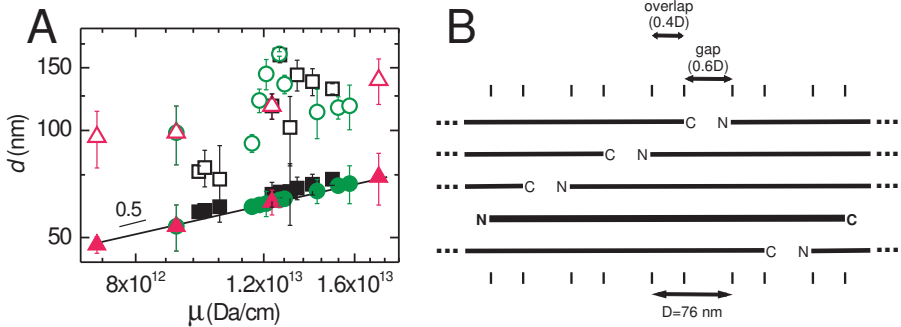


FIGURE 6.9. (A) Diameter of hydrated fibrils measured by turbidimetry (open symbols) and expected diameter calculated from the measured mass/length ratio (closed symbols), assuming regular axial and lateral packing, where $d = 1.83\sqrt{N}$ and N is the number of molecules per cross-section. Data are plotted versus the mass/length ratio measured by turbidimetry. Symbols denote: pure collagen I networks (squares), collagen I/V 80/20 networks (circles) and networks with different I/V ratio (triangles). Solid line indicates expected \sqrt{N} scaling. (B) Cartoon showing axial packing of collagen fibers.

6.4 DISCUSSION

The main finding in this chapter is that collagen V addition strongly decreases the elastic shear modulus of collagen I gels. Incorporation of 10% collagen V decreased the stiffness 2-fold, while 20% collagen V reduced the stiffness 3-5 fold. Pure collagen V networks were 10-fold softer than pure collagen I networks. Fluorescence microscopy showed no major change in network microstructure in the presence of collagen V. Turbidimetry showed that hybrid fibers had a

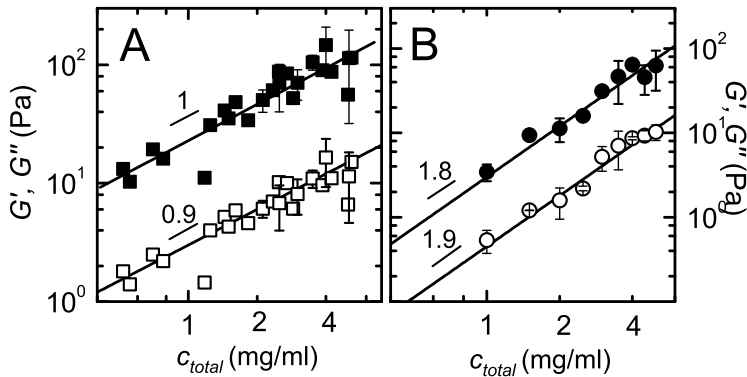


FIGURE 6.10. Linear elastic (solid symbols) and viscous (open symbols) shear moduli for (A) pure type I collagen networks and (B) mixed 80/20 collagen type I/V networks. Lines indicate power-law fits with exponent as indicated.

smaller mass/length ratio and somewhat smaller diameter than pure collagen I fibrils. AFM confirmed that the fibers became thinner with increasing collagen V content, and showed that pure collagen V fibers were shorter than collagen I containing fibers. Moreover, AFM images showed evidence of a tendency for collagen fibers to form loose bundles.

To interpret the effect of collagen V on network stiffness, in terms of the structural properties of the networks, we will compare the measured concentration dependence of the network stiffness (Fig. 6.3 A) with theoretical models for stiff biopolymers. There are two distinct models, *thermal* models based on entropic elasticity and *athermal* models based on enthalpic elasticity. In both cases, one needs to further distinguish between nonaffine and affine regimes. Computer simulations predict that sparsely crosslinked networks will deform in a nonuniform (*nonaffine*) manner [118, 311, 72, 144, 49, 67]. There are no simple analytical models in this regime. Densely crosslinked networks will deform *affinely*, resulting in fiber stretching. In this regime, the network elasticity can be calculated analytically from the number density of the fibers and their stretching rigidities [285].

Affine models predict power law dependencies of the linear elastic modulus, G_0 , on fiber concentration, according to $G_0 \sim c^{11/5}$ for a thermal sys-

tem [195] and $G_0 \sim c^1$ for an athermal system [119, 49]. A log-log plot of our data suggests power-law scaling with exponents of 1.0 ± 0.1 for pure type I gels and 1.8 ± 0.1 for 80/20 collagen I/V networks (Fig. 6.10). However, when plotted on linear scales (Fig. 6.3 A), the data actually show two distinct concentration regimes: below 3 mg/ml the stiffness increases with concentration, but above 3 mg/ml it is constant. The simple scaling predictions assume a constant fiber diameter. We showed that the fiber diameter changes with concentration (Fig. 6.7 B). This will affect the bending and stretching rigidity of the fibers, as well as the scaling of fiber density with protein concentration. Therefore, we do not expect a simple scaling law for $G_0(c)$. Prior studies of collagen rheology [323, 294, 297, 156, 282, 283] reported widely varying power law exponents ranging from 1 to 3. Our observations suggest that this variability may be, at least in part, related to different concentration dependencies of the fibril diameter, which will likely depend on the collagen source, presence of telopeptides, and assembly conditions.

Treating the fibers as homogeneous elastic cylinders of radius r and Young's modulus E , the bending rigidity is $\kappa_{bend} = \pi E r^4 / 4$ and the stretching rigidity is $\kappa_{stretch} = \pi E r^2$. The length density of fibers per volume, ρ , follows from the fiber mass/length ratio and weight concentration of collagen as $\rho = c N_A / \mu$, assuming randomly arranged fibers, where N_A is Avogadro's constant. The mesh size, $\xi = \rho^{1/2}$, should decrease from 2.7 μm at 0.3 mg/ml collagen to 0.6 μm at 5 mg/ml (open triangles in inset of Fig. 6.7 A). This prediction is in qualitative agreement with the confocal images, at least above 2 mg/ml collagen, where the networks are rather homogeneous. At lower concentrations, the images show network inhomogeneities, so that the calculation underestimates the mesh size (below, we neglect this effect). Note that the calculated mesh size at a collagen concentration of 2 mg/ml is smaller than the mesh size obtained by binarizing the confocal images (1 μm compared to 3 μm), which may reflect network inhomogeneities. However, the optical mesh size also has a sizeable error, on the order of 1 μm , and is sensitive to the threshold value chosen for binarizing the images. We therefore treat this parameter as indicative of changes in response to changes in collagen concentration, but do not use it in calculations of network elasticity below.

If the network is composed of filaments with appreciable thermal bending, the network elasticity can be calculated from the entropic resistance of polymer segments between crosslinks to stretch. This approach has been previously applied to collagen gels [243, 323]. The linear elastic modulus is $G_0 = 6\rho k_B T l_p^2 / l_c^3$, where k_B is Boltzmann's constant, T is absolute temperature, and l_p is persistence length, which is related to the bending rigidity as $l_p = \kappa_{bend} / k_B T$ [195]. The crosslink distance, l_c , is proportional to the entanglement length, l_e , and related to ρ and l_p by the scaling relation [195]: $l_c = A l_p^{1/5} \rho^{-2/5}$, where A is unknown but empirically found to be close to 1 (see Chapter 3). Treating the fibers as homogeneous elastic beams with $E = 70$ MPa (a value chosen to be consistent with two prior studies of collagen gel rheology [282, 260, 283] and consistent with single fibril measurements, as summarized in the Table 1 in the Appendix) and a diameter equal to the average value measured by turbidimetry, we obtain $l_p = 15$ cm at 2 mg/ml collagen and $G_0 = 452$ kPa, which is

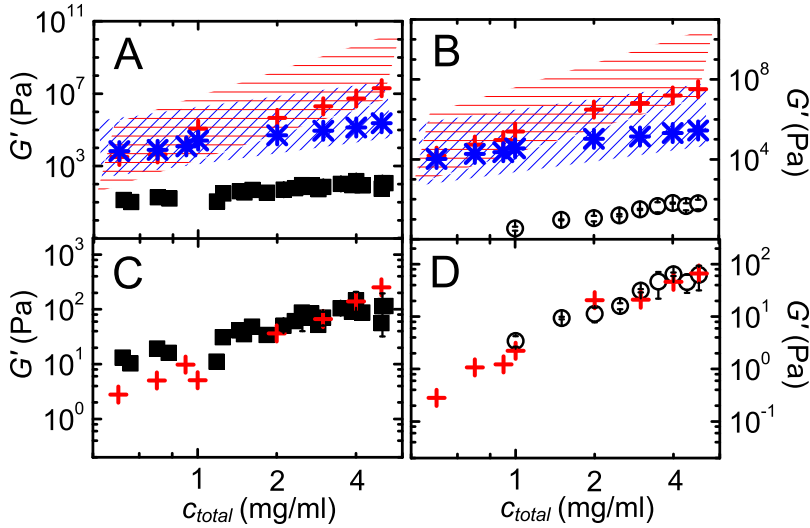


FIGURE 6.11. Experimental data for collagen network stiffness as a function of total collagen concentration, compared with theoretical estimates. Collagen fibers are modeled as simple elastic beams with a diameter measured by turbidimetry and a Young's modulus of 70 MPa. (A) Squares represent experimental data for a pure collagen I network. Crosses show the affine entropic model prediction, assuming that the network compliance is dominated by the thermal (entropic) compliance of collagen fibers when stretched. Stars represent the affine mechanical model prediction, assuming that the network compliance is dominated by mechanical (enthalpic) stretching of collagen fibers. Shaded areas behind symbols show predicted, from affine entropic and affine enthalpic model, range of elastic modulus based on a Young's modulus in the range of 30-800 MPa. (B) Affine entropic and affine mechanical prediction for collagen 80/20 networks (open circles represent experimental data). (C) Affine entropic model (crosses), using the fiber persistence length as a free parameter, with $l_p = 180 \mu\text{m}$ for collagen type I networks and (D) $l_p = 70 \mu\text{m}$ for hybrid 80/20 gels.

10^4 times larger than the measured modulus (Fig. 6.11 A). Even if we allow for variations in fiber diameter (over a range of 100 to 160 nm as measured by turbidimetry) or Young's modulus (over the range of 30-1500 MPa reported in the literature), we cannot account for this large discrepancy. However, this estimate disregards the complex internal structure of the fibers. If we instead treat l_p as a free parameter to account for fiber softening due to molecular defects such as kinks [204], slippage between fibrillar subunits [273, 204, 45], or lateral inhomogeneities in molecular packing [113], we can only get agreement between our data and the model if we assume $l_p = 180 \mu\text{m}$ for pure collagen I (Fig. 6.11 C) and $l_p = 70 \mu\text{m}$ for hybrid (80/20) networks (Fig. 6.11 D). These values are many orders of magnitude smaller than anticipated based on the bulk

Young's modulus. Interestingly, the numbers are closer to values reported in a recent EM study, where a persistence length of 10 μm was inferred from the shape of collagen fibrils deposited and dried on an EM grid [274]. There are two alternative interpretations of this intriguing finding. One interpretation is that the fibrils are indeed much more flexible than anticipated based on continuum elastic calculations due to their complex internal structure. A minimum limit on the persistence length can be estimated by modeling the collagen fibril as a bundle of fully decoupled tropocollagen molecules [61]. This yields an estimate of 17 μm for fibrils with 1200 molecules per cross-section, each having a persistence length of 14.5 nm [288]. However, collagen fibrils look very straight in all our AFM and optical microscopy (bright field) images. An alternative explanation for the short l_p reported from the EM study is that it reflects intrinsic curvature rather than thermal fluctuations. This interpretation was also put forward by A. Stein and D. Vader et al in their rheology study [282, 283], where experimental data were well-fit by a computational 3D-fiber model assuming that the fibers are rigid rods (having no thermal fluctuations), but with an intrinsic curvature characterized by a geometrical persistence length of 20 μm . We favor this second explanation, and believe that it is unlikely that collagen network elasticity is entropic in origin. However, a definitive test will be needed in the form of direct dynamic measurements of the filament persistence length in solution. This can be achieved by measuring thermal bending undulations of the fibers, e.g. by optical tweezers [232].

If we assume instead that the fibers behave as stiff rods, the network elasticity should be enthalpic in origin and reflect the mechanical resistance of the fibers to axial stretch. The elasticity of an isotropic network of rods is $G' = (1/15)\rho\kappa_{stretch}$. At 2 mg/ml collagen (where the fiber diameter is 117 nm), $\kappa_{stretch}$ is 753 nN and G' is 50 kPa, which is 1000-fold larger than the measured stiffness (Fig. 6.11 A). This large discrepancy suggests that the collagen networks do not deform affinely at the fiber scale. Any nonaffine deformation such as fiber bending and reorientation will reduce G' relative to the affine limit [311, 118, 144, 67, 282, 283, 135, 40]. It is difficult to calculate the impact of nonaffinity on the rheology since G' will be sensitive to the exact network connectivity, which is determined by collagen fiber length and the topology and mechanical properties of the noncovalent (physical) crosslinks between fibers, which are all unknown. A more promising approach is to simulate 3D-fiber networks using collagen-based parameters as input [49, 144, 67, 282, 283].

Our nonlinear rheology data provide circumstantial evidence of nonaffinity. We showed that networks up to 2 mg/ml collagen strain-stiffen. In networks of stiff rods, strain-stiffening is indeed expected when the elastic energy is predominantly stored in fiber bending. The reason is that large shears align the filaments, inducing a transition to a stiffer elastic regime dominated by fiber stretching [224, 67]. Numerical simulations also suggest that nonaffine strain-induced alignment explains the nonlinearity of collagen networks [282, 283]. Interestingly, we observed that networks of more than 2 mg/ml collagen strain-weaken. We speculate that the thicker fibers formed in this regime are too stiff to bend, forestalling a bending-to-stretching transition. We plan to measure nonaffinity directly by mapping the 3D-strain field of sheared collagen gels by

confocal microscopy. Prior microscopy studies suggest nonaffinity [260, 250, 54]. Further evidence for nonaffinity was presented in the form of a system size dependence of the nonlinear rheology [8].

There is currently no simple analytical expression to predict the elastic modulus of networks of stiff polymers that deform nonaffinely. This hampers a quantitative interpretation of the dependence of collagen network stiffness on collagen V content. Collagen V does not appear to substantially modify the network architecture. Nevertheless, it is conceivable that collagen V changes intermolecular interactions between tropocollagen monomers. Collagen fibrils have a complicated internal architecture, involving laterally associated microfibrils, that themselves are built up of tropocollagen subunits that are noncovalently bonded. It is conceivable that incorporation of collagen V alters the intermolecular spacing and/or intermolecular adhesion, thereby influencing the shear strength between adjacent molecules and the bending rigidity. This could be tested by bending or stretching tests on single fibers [273, 321, 296, 271]. The molecular adhesion between collagen I and V molecules could be tested by osmotic pressure measurements coupled with X-ray scattering [170]. Alternatively, collagen V may alter interfibrillar interactions and thus the network connectivity. Our AFM images showing loose bundling of hybrid fibrils suggest that the hybrid fibers may be more adhesive than pure collagen I or pure collagen V fibrils. Since the elasticity of the collagen networks is nonaffine in origin we cannot easily distinguish between effects of collagen V on the fiber or network level. Multiscale simulation models of collagen networks taking into account collagen's remarkable hierarchical structure may potentially facilitate a molecular interpretation of the influence of co-polymerizing agents such as collagen V on network mechanics [45].

Collagen V's effect on the rheology of collagen networks may play an important role in soft connective tissues *in vivo*. Most healthy adult tissues contain only 2-5% collagen V [202], but the collagen V level is higher in embryonic and regenerating tissues [255, 35]. Moreover, several connective tissue diseases [197, 7, 308] and pathological conditions such as tumors, atherosclerotic plaques, and scars [35] are associated with anomalous levels of collagen V. Our work suggests that collagen V influences collagen matrix mechanics. This may in itself adversely affect tissue function, but it may also influence the behavior of the resident cells. It has been shown that cell adhesion, cytoskeletal structure, and even differentiation are strongly influenced by the stiffness of the extracellular collagen matrix [328, 75]. *In vitro* studies revealed several effects of collagen V on cell behavior: collagen V enhances collagen gel contraction by fibroblasts [21] and affects cell migration [35, 198, 238, 6, 58]. It has been suggested that differences in integrin-mediated cellular interactions with collagen might be involved [21]. Since our findings show that collagen V can influence collagen network mechanics, it is conceivable that collagen V may also influence cell behavior by causing mechanical changes in the extracellular matrix. However, to test this hypothesis, it would be necessary to measure effects of changing collagen V levels on the mechanical properties of biological tissues. The effect of collagen V on tissue mechanics *in vivo* may namely be different from its effect *in vitro*. Collagen V *in vivo*, for instance, retains long propeptides, in contrast

to the atelocollagen V used in this study, whose effect on collagen rheology is yet unknown. Furthermore, collagenous tissues contain many non-collagenous components such as proteoglycans and glycoproteins, which may modulate the overall mechanical response.

6.5 CONCLUSION

We discovered that incorporation of collagen type V substantially lowers the stiffness of reconstituted networks of collagen type I over a wide range of total collagen concentrations. Homotypic and heterotypic collagen networks both display two distinct concentration regimes, differing in structural organization and mechanical behavior. At low concentrations (1 mg/ml or less), the networks are somewhat heterogeneous, strain-stiffen, and the plateau modulus increases with increasing collagen concentration. In contrast, at high concentrations (more than 2 mg/ml), the networks are more homogeneous and strain-soften and the plateau modulus is concentration-independent. A direct comparison of the rheology data with theoretical predictions for stiff polymers suggests that the network elasticity is dominated by nonaffine deformation modes. Unfortunately, there is no tractable analytical expression available which predicts the network modulus in this mechanical regime, hampering a quantitative interpretation of the influence of collagen V. Collagen V may potentially affect the intermolecular interactions among tropocollagen monomers, which may in turn affect the rheology by changing the rigidity of the fibrils as well the interactions among fibrils. The effect of collagen V on network stiffness is relevant to interpret the role of changed collagen V levels in fetal development and natural tissue regeneration as well as in various connective tissue disorders. Moreover, our findings suggest that collagen composition can be used as a powerful control parameter to design collagen-based biomaterials with controlled mechanical properties.

6.6 APPENDIX

6.6.1 SUMMARY OF YOUNG'S MODULI (E) AND PERSISTENCE LENGTHS (l_p) DETERMINED FOR HYDRATED COLLAGEN FIBRILS

TABLE I. Summary of Young's moduli (E) and persistence lengths (l_p) determined for hydrated collagen type I fibrils from various sources, using various experimental techniques. Persistence length values with asterisk are calculated from E and the fiber diameter, d , assuming homogeneous and linear elasticity.

E , mean (range) (MPa)	l_p	D (nm)	Method	Collagen source	Ref.
32	0.004-0.03 cm*	10-30	AFM ¹ stretching	Reconstituted from collagen produced by fibroblasts	[103]
70-170	493-6421 cm*	280-426	AFM bending	Bovine tendon	[321]
250-450	459-826 cm*	~200	AFM stretching	Bovine tendon	[296]
470 (110-1470)	952-21713 cm*	205-448	MEMS ² stretching	Sea cucumber dermis	[271]
1.2	0.03-0.7 cm*	70-150	Fibril indentation	Bovine tendon	[105]
500	573428 cm*	1000	Fiber stretching	Rabbit patellar tendon	[205]
35 kPa*	10 μ m	50-500	Fiber shape analysis	Bovine skin	[274]

¹ Atomic Force Microscopy

² MicroElectroMechanical System

* Calculated assuming continuum elasticity, and an isotropic cylindrical rod

I would like to thank Saskia Duineveld, Marina Soares e Silva, Martijn de Wild and Hans Zeijlemaker for assistance with experiments; Fred MacKintosh and Chase Broedersz (Vrije Universiteit, Amsterdam) and Kees Storm (Technische Universiteit, Eindhoven) for helpful discussions about collagen mechanics; and Maarten Merks (Technische Universiteit, Eindhoven) for his gift of CNA35.

7 *In vitro* RECONSTITUTION OF COMPOSITE NETWORKS OF VIMENTIN AND MICROTUBULES

THE shape of cells is defined by their internal cytoskeleton, which consists of microtubules, actin filaments, and intermediate filaments interconnected by crosslinking proteins and motors. This composite protein network enables cells to withstand mechanical forces, but also to actively generate forces. Studies of networks composed of either actin with intermediate filament or actin with microtubules indicate that the disparate bending rigidities of the filaments and interactions between them can lead to surprising non-additive effects on network elasticity. Composite networks of intermediate filaments, which are the most flexible among all cytoskeletal filaments, and microtubules, which are the most rigid, have not been studied yet. In this chapter, we reconstitute an *in vitro* system composed of microtubules and vimentin, which is a type III intermediate filament. Since both proteins require different buffer conditions for proper assembly, we used electron and fluorescence microscopy to image filaments formed in different buffers and identify conditions allowing for simultaneous polymerization of microtubules and vimentin. Confocal microscopy revealed that microtubules embedded in vimentin networks were bent, possibly due to forces exerted by polymerizing vimentin filaments. With the aid of rheology measurements we found that the mechanical properties of reconstituted microtubule-vimentin networks were intermediate between those of pure MTs and pure IFs. The new composite cytoskeletal model system created in this chapter paves the way for future systematic studies of the influence of filament interactions on cytoskeletal network mechanics.

7.1 INTRODUCTION

The mechanical properties of living cells are mainly determined by the cytoskeleton, a cytoplasmic biopolymer network consisting of actin filaments, microtubules (MTs) and intermediate filaments (IFs). IFs are a large superfamily with at least 65 distinct proteins in man, which are differentially expressed in a tissue-dependent and developmentally regulated manner [130, 126, 127]. IF proteins are categorized into six types (types I-VI), or, alternatively, in three assembly groups, known as groups I, II, and III, which can coexist as three separate IF systems within the same cell [125, 226, 89].

All three cytoskeletal filament types can be classified as semiflexible polymers with a persistence length, l_p , that has a similar magnitude as the contour length, l_c . However, they have highly disparate bending rigidities: MTs are the most rigid filaments with $l_p=5$ mm, actin filaments are more flexible with $l_p=15$ μm , and intermediate filaments are the most flexible with $l_p=0.5\text{-}1$ μm [32, 97, 264, 164, 209, 182, 138, 210, 18]. *In vivo*, the filaments are known to colocalize and strongly interact with each other. In fibroblasts, for example, association of IFs and actin [106], IFs and MTs [110], and actin and MTs [32] was found. Actin networks are often considered to be the main component responsible for the viscoelastic properties of cells [236] and for their stress-stiffening response to an imposed mechanical stretch [84, 292]. However, recent studies show that intermediate filaments also play a major role in cell mechanical resistance. For instance, keratin determines the mechanical strength of keratinocyte cells [194, 90], while vimentin contributes to the linear stiffness and stress-stiffening of fibroblasts [302, 234].

There are many indications that the three types of filaments influence each other's organization and that interactions between them influence the overall mechanics of cells [55, 249, 60, 100, 227]. This crosstalk involves structural as well as regulatory interactions [171]. It is known, for instance, that the spatial arrangement of microtubules depends not only on microtubule organizing centers (MTOCs) [37], but also on the cytoplasmic environment. Microtubules growing in the peripheral actin-myosin cortex are bent by contractile myosin-driven forces [33]. Since the actin network is elastic, it suppresses large scale microtubule buckling and allows microtubules to bear enhanced compressive loads [32, 68]. This is consistent with the so-called tensegrity model, which states that cellular shape stability is achieved via a balance between actin filaments and IFs loaded under tension and MTs and thick actin bundles under compression [147, 278].

To obtain physical insight into the mechanisms by which the cytoskeleton controls cell mechanics, there have been many *in vitro* studies of purified cytoskeletal systems. Most of these studies have considered networks reconstituted from one filament type, either alone or with regulatory proteins such as crosslinkers and motors specific for that type. It was shown that crosslinked networks of actin as well as networks of IFs exhibit a rich mechanical behavior, which is tuned by filament and crosslinker density [94, 182, 180, 119, 118]. At low filament and crosslink densities, the network elasticity is dominated by nonaffine, bending modes and the networks generally strain-weaken. At high

filament and crosslink densities, the elasticity is dominated by affine filament stretching and the networks strain-stiffen due to the entropic resistance of the filaments when their thermal slack is pulled out [195, 285]. The molecular structure of the crosslinking proteins also affects the network response, for instance by affecting the network architecture [176] or by directly contributing to the macroscopic network compliance [189, 41]. The complex, bundle-like internal architecture of IFs was shown to make them extremely extensible, in contrast to actin filaments, which are rather inextensible [240, 150]. Contrary to actin and IF networks, MT networks strain-weaken, independent of filament and crosslink density [183, 48]. Given their large bending rigidity, MTs likely behave as athermal rods, which bend and/or reorient when the network is sheared, rather than stretch.

In vitro systems of individual cytoskeletal network are unlikely to capture the full richness of the mechanics of the *in vivo* cytoskeleton. To date there have only been a handful of *in vitro* studies probing the mechanical consequences of the composite nature of the cytoskeleton. It has been shown that rigid MTs embedded in networks of more flexible actin filaments can change the nonlinear elastic response even at low MT density [181, 10]. The MTs suppress bending fluctuations of actin filaments, and thereby make the strain field more affine. MTs can thereby convert the strain-weakening response of sparsely crosslinked actin networks into an affine strain-stiffening response. It was furthermore shown by microrheology that MTs make actin networks compressible [229], which was rationalized by theoretical calculations [69]. Addition of stiff rods to an incompressible elastic medium such as an actin network reduces the effective Poisson ratio. MTs do not contribute to the linear elasticity of composite MT-actin network [181], suggesting that they interact only by steric repulsion with actin.

By contrast, addition of actin filaments to networks of vimentin or neurofilaments (NF), which both belong to the family of IFs, increases the linear elastic modulus over that of the two separate protein systems [76, 172]. This nonadditivity suggests the presence of attractive interactions between IFs and actin filaments. Indeed, it was shown that the C-terminal tail domain of vimentin mediates direct interactions with actin [76]. The composite networks also exhibited a weaker frequency dependence of the elastic modulus, which likewise indicates interactions between actin and vimentin. In networks composed of NFs and actin, the long side extensions of the NFs were shown to cross-bridge actin filaments and inhibit lateral alignment of NFs [172]. This was shown to reduce efficient cross-bridging among NFs, thereby reducing the mechanical resistance of composite actin-NF networks to large stresses compared to pure NF networks.

The mechanical behavior of composite networks of MTs and IFs has not yet been reported. Since MTs are at least 1000-fold more rigid than IFs, we anticipate rich mechanical behavior in this case. It has been proposed that IFs may increase the resistance of MTs to compressive loads by acting as an elastic support [38]. Moreover, IFs may potentially reinforce networks of MTs, which by themselves strain-weaken. Conversely, MTs may reinforce IF networks by acting as long and rigid inclusions. Reinforcement of soft networks by stiff elements such as carbon nanotubes increases the linear elasticity as well as the mechanical resistance when there are direct interactions between the com-

ponents [50, 4, 101]. Intriguingly, even in the absence of direct interactions, MTs can still promote strain-stiffening behavior of F-actin [181].

In this chapter, we reconstitute composite networks of microtubules and intermediate filaments from purified bovine brain tubulin and human recombinant vimentin. Vimentin is a class III and assembly group 2 type of intermediate filament, which occurs in nearly all mesenchymal cells [126]. Individual filaments and composite networks were assembled using different buffer conditions, in order to identify conditions that would allow for simultaneous polymerization of both filament types. Confocal and electron microscopy (EM) were used to visualize network and filament structures (see Chapter 2). The nonlinear viscoelastic properties of the networks were probed by large amplitude oscillatory shear tests in a plate-plate rheometer.

7.2 SAMPLE PREPARATION

7.2.1 VIMENTIN NETWORK PURIFICATION AND ASSEMBLY

Human vimentin was expressed in *Escherichia (E.) Coli* and purified from inclusion bodies [129], followed by ion exchange chromatography on an anion exchange columns (DEAE-Sepharose) and a cation exchange column (CM-Sepharose, GE Healthcare life Sciences). The protein was eluted with a potassium chloride gradient. The vimentin was pure as assessed by SDS-PAGE gel electrophoresis, which revealed only a single band at the expected molecular weight of 54 kDa. Purified vimentin was stored at -80°C in a pH 7.5 buffer (5 mM Tris-HCl, 1 mM dithiothreitol (DTT), 1 mM ethylenediaminetetraacetic acid (EDTA), 1 mM ethylene glycol tetraacetic acid (EGTA), 10 mM methyl ammonium chloride (MAC)), which contained 8 M urea to keep the protein soluble. Before use, the urea concentration was reduced to 1 M by sequential dialysis against buffers (5 mM Tris-HCl, 1 mM DTT, 1 mM EDTA, and 0.1 mM EGTA, pH 8.4) of stepwise decreasing urea concentration (6 M, 4 M, 2 M). We used a cellulose membrane of 8-10 kDa molecular weight cut-off (Spectra/Pro) for the dialysis. Finally, the urea concentration was reduced to 0 M by dialyzing the sample overnight at 4°C against fresh dialysis buffer. Vimentin is present in this buffer in the form of tetramers, as observed by analytical ultracentrifugation [129]. Vimentin forms parallel coiled-coil dimers upon lowering the urea concentration to 6 M [129] (Fig. 7.1). The dimers are rod-shaped with a length of 45-50 nm. In 4.5 M urea, the dimers laterally associate into antiparallel tetramers. Due to this antiparallel arrangement, IFs possess no structural polarity, in contrast to actin filaments and MTs [218]. The final protein concentration was determined by a Bradford assay (Sigma Aldrich) with bovine serum albumin in water as a standard. Vimentin was polymerized by mixing vimentin tetramers in dialysis buffer with assembly buffer, as explained in the Section 7.3.

7.2.2 COMPOSITE VIMENTIN-MICROTUBULE NETWORK ASSEMBLY

Microtubules were pre-polymerized at few different concentrations from a tubulin stock solution (Cytoskeleton) in a 37 °C water bath for 1 hour, and stabilized with 10 μ M taxol (Sigma Aldrich). Taxol-stabilized microtubules were mixed with vimentin tetramer solutions of varying vimentin concentration. Vimentin polymerization was then initiated by addition of 1/10 of 10X assembly buffer to the total sample volume and warming to 22 °C. For confocal imaging, unlabeled tubulin was mixed with rhodamine labeled tubulin (Cytoskeleton) in a 10:1 molar ratio. Vimentin was not labeled.

7.3 RESULTS

7.3.1 NETWORK AND FILAMENT STRUCTURE

In vitro reconstitution of composite networks of two filament types is challenging since each filament type has individual requirements for native-like assembly. Intermediate filaments display a marked polymorphism depending on the temperature, pH, ionic strength, and specific salt and buffer types present during assembly [124, 284]. Similarly, the growth and dynamics of microtubules is highly sensitive to buffer conditions [303], temperature [92], and solution pH [244]. To optimize the conditions for both microtubules and vimentin assembly, we first screened different buffer conditions for the individual networks, checking the filament structure by EM and fluorescence microscopy.

Based on viscometry studies and EM, it is known that the main structural changes during vimentin assembly take place within the first hour of polymerization [310, 286, 228]. Upon mixing of vimentin tetramers with assembly buffer, the tetramers laterally associate into hexadecamers, which subsequently laterally associate to form Unit-Length-Filaments (ULFs) with a diameter of 16 nm. The ULFs anneal longitudinally to form short filaments, which lengthen over time [123, 275, 235] (Fig. 7.1 A). The diameter of mature IFs is \sim 10 nm, smaller than the diameter of individual ULFs [128], due to radial compaction during the first hour of the assembly process [128]. Combined with structural rearrangements involving changes in the relative position of tetramers with respect to each other [123], polymerization finally leads to the formation of 10 nm diameter filaments. Mass-per-length measurements by scanning transmission electron microscopy showed that the mass/length ratio of vimentin filaments formed by rapid dilution varies along the filament backbone between 24 and 40 molecules (or 6 to 10 tetramers) per cross-section [129, 128, 129]. In contrast, filaments formed slowly by dialysis against assembly buffer are smoother, with a constant mass/length ratio of 37 kDa/nm, or 29 molecules per cross-section [129].

We first assembled vimentin networks at different protein concentrations (0.14, 2 and 3 mg/ml) in a 45 mM Tris-HCl buffer of pH 7.0 with 50 mM NaCl. Similar buffer conditions (but with 25 mM Tris-HCl and pH 7.5) were previously shown to promote the formation of normal, 10 nm wide filaments [131]. Our EM imaging showed that the filaments were several micrometers long, gen-

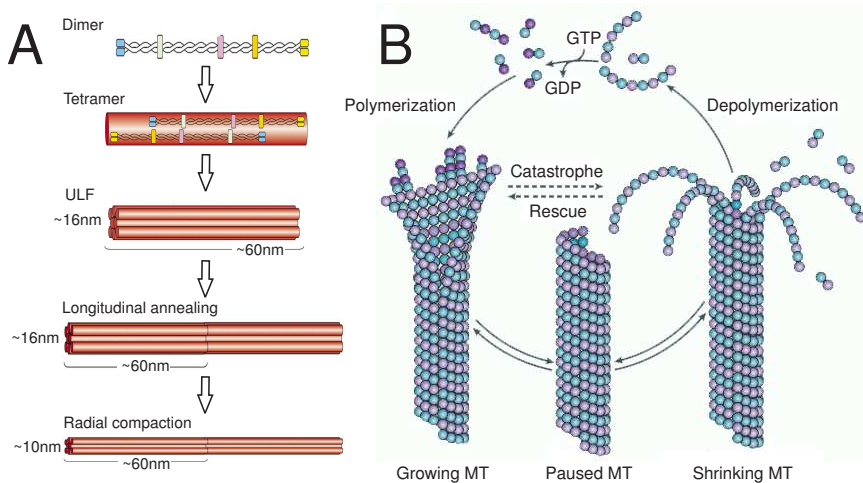


FIGURE 7.1. Schematic showing different stages of intermediate filament assembly (A) and dynamic instability of microtubules (B). Pictures adapted from [100, 66].

tly curved, and entangled (Fig. 7.2 A-C). We note that the density of filaments on the surface is not representative of the bulk density. For the 0.14 mg/ml network, the EM grid displayed a similar filament density everywhere, but for the 2 mg/ml and 3 mg/ml networks, most of the grid surface was too densely covered to identify filaments. The average diameter of the filaments was approximately 10 nm at all three concentrations, consistent with previous reports [123]. At the highest concentration of 3 mg/ml, the filaments appear more straight and aligned (Fig. 7.2 C), which may be caused by shear forces applied during sample deposition and/or drying onto the EM grid.

We next replaced the 45 mM Tris-HCl buffer with a sulfonate 1,4-Piperazinediethanesulfonic acid (PIPES) buffer of the same concentration but lower pH (6.8). This buffer is the most commonly used buffer for MTs and its replacement had a significant effect on the structure of the vimentin filaments (Fig. 7.3 A). After 1 hour of polymerization at 0.2 mg/ml vimentin, only short filaments accompanied by small subunits (white arrow) were visible. The filaments rarely overlapped and often had a branched and unwound structure (black arrows). Increasing the protein concentration to 2 mg/ml led to filament aggregation (Fig. 7.3 B), but the filament length remained small. When the PIPES concentration was lowered from 45 to 25 mM, and the pH increased to 7.0, we observed a striking change in filament morphology: long and entangled filaments were again formed, comparable to the filaments formed in Tris-HCl buffer (Fig. 7.3 C).

IFs assembly is highly dependent on ionic strength and usually polymerization takes place in the presence of sodium chloride [128]. Assembly of microtubules, on the other hand, requires magnesium ions, which have a catalytic effect on hydrolysis of tubulin-associated Guanosine-5'-triphosphate (GTP) [220].

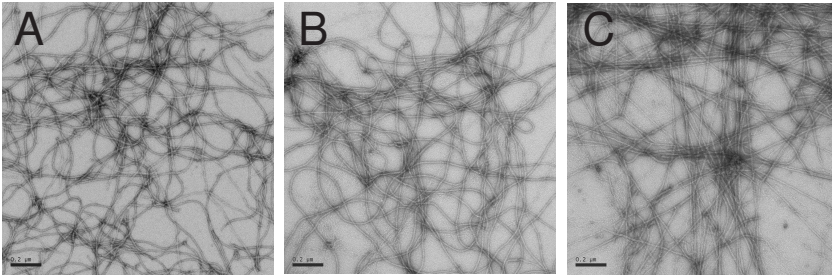


FIGURE 7.2. Electron microscopy images of vimentin networks assembled at 22 °C with different protein content in buffer containing 45 mM Tris-HCl, 50 mM NaCl, pH 7.0. (A) 0.14 mg/ml vimentin, (B) 2 mg/ml vimentin, (C) 3 mg/ml vimentin. Scale bars, 200 nm.

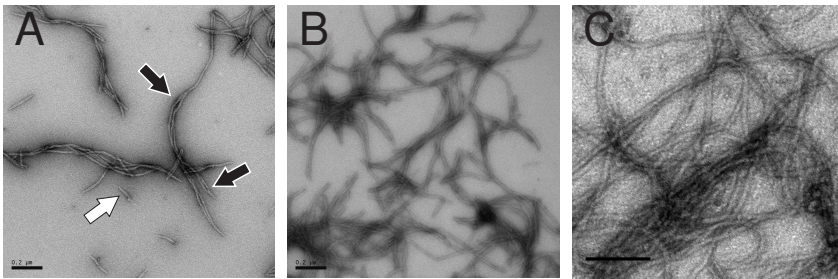


FIGURE 7.3. Electron microscopy images showing the effect of different buffer conditions on assembly of 0.2 mg/ml (A, C) and 2 mg/ml vimentin networks (B). Networks were assembled at 22 °C in: (A) and (B) 45 mM PIPES, 50 mM NaCl, 1 mM EGTA, 4 mM MgCl₂, pH 6.8, (C) 25 mM PIPES, 1 mM EGTA, 4 mM MgCl₂, pH 7.0. Scale bars, 200 nm.

This energy source destabilizes the MT lattice, leading to dynamic instability: MTs are continually in either a growing or shrinking state [140, 300] (Fig. 7.1 B). Magnesium ions required by MTs are compatible with IF assembly, but act as crosslinks, causing an increase in network stiffness [180, 161, 182].

To test the influence of different salts on vimentin network structure, we assembled vimentin in the presence or absence of sodium and magnesium chloride. With no salt present, vimentin forms network with filaments that are ~24 nm in diameter (Fig. 7.4 A). This is more than twice the thickness of filaments assembled in the standard buffer, which contains 50 mM Na⁺ (Fig. 7.4 B). Addition of 4 mM Mg²⁺ to the buffer did not noticeably change the network or filament structure (Fig. 7.4 C). These results indicate that the main components of the MT buffer that affect vimentin assembly are the PIPES buffer and/or the pH.

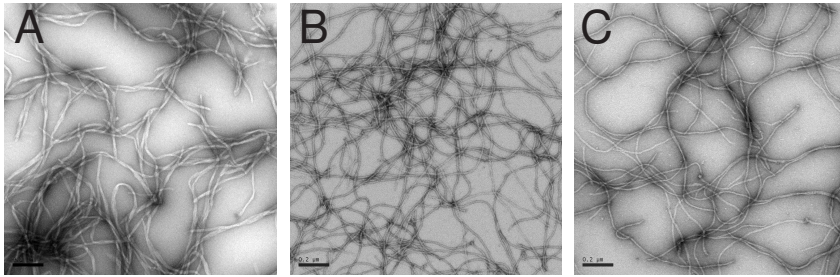


FIGURE 7.4. Electron microscopy images showing the effect of NaCl and MgCl₂ on assembly of 0.2 mg/ml vimentin network. Networks were polymerized at 22 °C in: (A) 45 mM Tris-HCl, pH 7.0, (B) 45 mM Tris-HCl, 50 mM NaCl, pH 7.0, (C) 45 mM Tris-HCl, 50 mM NaCl, 4 mM MgCl₂, pH 7.0. Scale bars, 200 nm.

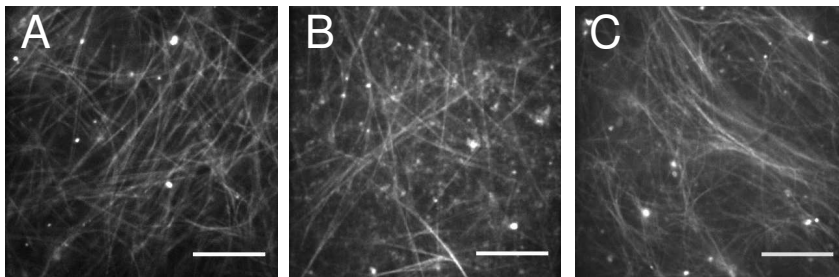


FIGURE 7.5. Confocal microscopy images of 1 mg/ml taxol stabilized microtubules. Filaments were polymerized at 37 °C in buffer containing: (A) 80 mM PIPES, 1 mM EGTA, 4 mM MgCl₂, pH 6.8, (B) 25 mM PIPES, 1 mM EGTA, 4 mM MgCl₂, pH 6.8, (C) 25 mM PIPES, 50 mM NaCl, 1 mM EGTA, 4 mM MgCl₂, pH 6.8. The bright blobs are likely due to aggregated tubulin. Scale bars, 10 μm.

Microtubules are commonly reconstituted in MRB80 buffer, which contains 80 mM PIPES, 1 mM EGTA, 4 mM MgCl₂, pH 6.8. Under these buffer conditions, MTs polymerize into long, straight filaments, as shown in the fluorescence micrograph in Fig. 7.5 A. Owing to their large persistence length, microtubules (which have lengths of several microns) undergo only slight bending undulations. Decreasing the PIPES concentration to 25 mM, the concentration which is compatible with vimentin assembly, did not perceptibly change the appearance of the MTs (Fig. 7.5 B). Addition of 50 mM sodium ions, however, resulted in networks with filaments that were unusually thin (Fig. 7.5 C).

Since the dynamics of microtubules are known to be pH-sensitive [244], we tested the effect of pH on MT assembly. The optimum pH for MT polymerization was reported to be close to 6.8 [289]. Indeed, MTs assembled in 25 mM PIPES buffer of pH 6.8 formed a homogenous network with long and straight filaments (Fig. 7.6 A). Increasing the pH to 7.0 did not change the network structure

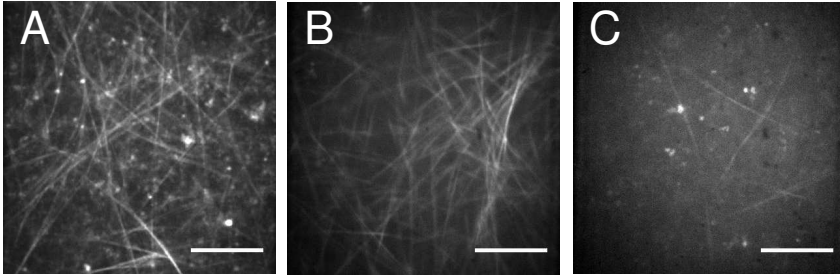


FIGURE 7.6. Confocal microscopy images of 1 mg/ml taxol stabilized microtubules, showing the effect of solution pH on MT assembly: (A) pH 6.8, (B) pH 7.0, (C) pH 7.4. Filaments were polymerized at 37 °C in buffer containing 25 mM PIPES, 1 mM EGTA, 4 mM MgCl₂. Scale bars, 10 μm.

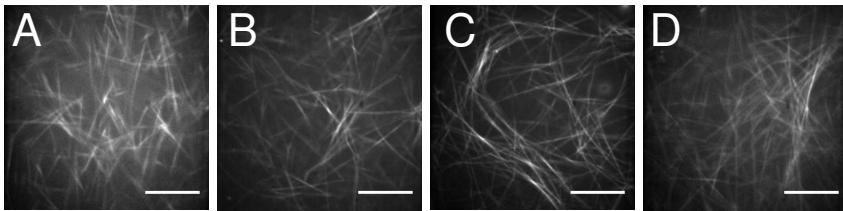


FIGURE 7.7. Confocal microscopy images of 1 mg/ml taxol stabilized microtubules, showing changes in filament length over time. Filaments were polymerized at 37 °C in buffer containing 25 mM PIPES, 1 mM EGTA, 4 mM MgCl₂, pH 7.0 for (A) 15 min, (B) 30 min, (C) 45 min and (D) 1 hour. Scale bars, 10 μm.

(Fig. 7.6 B), but an even higher pH of 7.4, which is commonly used for vimentin assembly, inhibited MT assembly; even after 1 hour, only a few, short filaments were seen (Fig. 7.6 C). We next tested the influence of polymerization time on MT length under buffer conditions compatible with vimentin (25 mM PIPES, 1 mM EGTA, 4 mM MgCl₂, pH 7.0). Within the first 45 minutes of polymerization, the MT length increased with increasing polymerization time (Fig. 7.7 A-C). However, after 1 hour (comparable to the time scale of vimentin assembly), the networks consisted of filaments with an average length exceeding tens of micrometers (Fig. 7.7 D).

From all tested conditions, only the buffer containing 25 mM PIPES, 1 mM EGTA, 4 mM MgCl₂, and pH 7.0 supported proper assembly of homotypic networks of vimentin and MTs. To test whether the two filament types also assemble properly when mixed together, we imaged networks of vimentin mixed with 0.2 mg/ml MTs that had been pre-formed under the same conditions as vimentin. As revealed by EM, both filament types do indeed coexist (Fig. 7.8 A): long and relatively straight microtubules (see arrows) are sur-

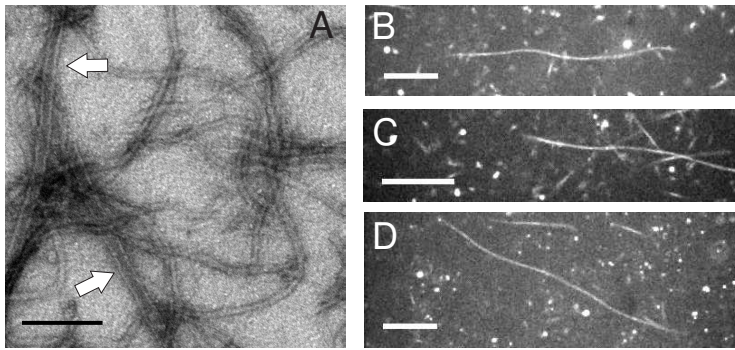


FIGURE 7.8. Microscopy images of composite networks prepared by polymerizing vimentin for 1 hour at 22 °C in the presence of 0.2 mg/ml taxol-stabilized microtubules (pre-formed for 1 hour at 37 °C). The buffer contains 25 mM PIPES, 1 mM EGTA, 4 mM MgCl₂, pH 7.0. (A) EM image of composite MT-vimentin network with 0.2 mg/ml vimentin. Arrows point to MTs, which are clearly recognizable as hollow tubules. (B, C, D) Confocal microscopy images of fluorescently labeled MTs embedded in 0.2, 0.5 and 1 mg/ml vimentin networks, respectively. Scale bars, 10 μ m.

rounded by a network of thinner and more curved vimentin filaments. Confocal microscopy of fluorescently labeled MTs embedded inside vimentin networks showed that the MTs are somewhat bent (Fig. 7.8 B-C), in sharp contrast with their straight appearance when assembled alone and observed in free solution (Fig. 7.7 D). This observation suggests that internal stresses in the vimentin network, which may build up during polymerization, distort the MTs. Compressive stresses on stiff filaments embedded in an elastic background may cause short wavelength buckling [32, 68, 158, 38]. Interestingly, fluorescently labeled actin filaments embedded in dark, entangled actin networks were also reported to be highly bent, which was tentatively ascribed to transient entropic trapping of bent filament segments in network void spaces [252].

7.3.2 MECHANICS OF VIMENTIN-MICROTUBULE NETWORKS

To test the effect of MTs on the mechanical behavior of vimentin networks, we assembled networks of the separate filament types as well as composite networks in a buffer containing 25 mM PIPES, 1 mM EGTA, 4 mM MgCl₂, and pH 7.0 and measured the viscoelastic shear moduli by rheology. Experiments were performed at 22 °C by large amplitude oscillatory shear tests (see Chapter 2), using a parallel plate geometry with a diameter of 40 mm and gap of 80 μ m.

The stiffness of pure vimentin networks increased weakly with increasing protein concentration, scaling as $G' \sim c^x$ with an exponent of 0.2 (Fig. 7.9, black squares). G' showed a similar concentration dependence when filaments were assembled in a conventional Tris-based vimentin buffer (45 mM Tris-HCl, 50 mM NaCl, pH 7.0), but with a ca. 1.9-fold larger magnitude (Fig. 7.9, green

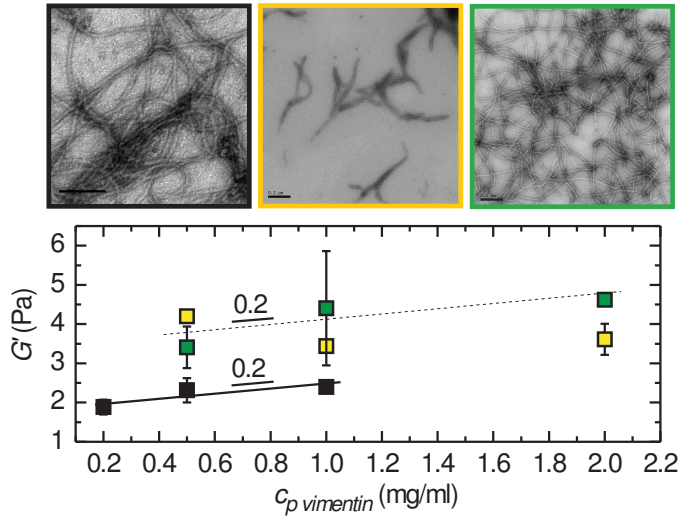


FIGURE 7.9. Dependence of the linear elastic modulus (at 0.5 Hz) on vimentin concentration in the presence of three different assembly buffers: optimal buffer for composite system (black squares; 25 mM PIPES, 1 mM EGTA, 4 mM $MgCl_2$, pH 7.0), non-optimal buffer for composite system (yellow squares; 45 mM PIPES, 50 mM NaCl, 1 mM EGTA, 4 mM $MgCl_2$, pH 6.8), and normal vimentin assembly buffer (green squares; 45 mM Tris-HCl, 50 mM NaCl, pH 7.0). EM images on top show the corresponding filament structure. Scale bars, 200 nm.

squares). The IF proteins vimentin, desmin, and neurofilaments, typically exhibit a weak concentration dependence with an exponent close to 1 in the absence of crosslinks [264, 180, 242] and a stronger dependence with an exponent of 2 in the presence of multivalent cations, which act as crosslinks [325, 182]. However, the exponent can also be much lower, depending on IF type and buffer conditions. For instance, exponents of 0.47 have been reported for vimentin, and 0.7 for desmin [264]. The origin of these variations in the concentration dependence is hitherto unexplained. It is possible that the variability is related to the degree of adhesiveness between the IFs, which is known to be sensitive to the salt concentration and pH. When assembled in the PIPES pH 6.8 buffer that produced short, branched and unwound filaments (Fig. 7.3 A-B), the network stiffness was independent of protein concentration (Fig. 7.9, yellow squares). Surprisingly, even at low protein content, where EM showed only small aggregates of short filaments, the networks were still predominantly elastic and G' was even somewhat larger than for networks prepared in the other two buffers that both favored assembly of normal-looking filaments. This shows that it is important to combine rheology with EM when the assembly conditions are varied, to check the structure of the filaments.

Addition of 0.1 mg/ml preformed microtubules to networks of vimentin resulted in an increase in network elasticity compared to the pure vimentin net-

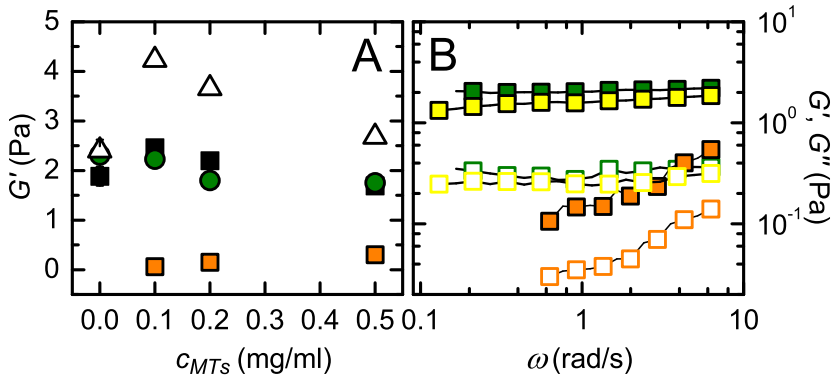


FIGURE 7.10. Linear viscoelastic behavior of composite vimentin-microtubule networks. (A) Influence of MT addition on the linear elastic modulus of networks of 0.2 (black squares), 0.5 (green circles), and 1 mg/ml (black open triangles) vimentin. Orange squares show stiffness of pure MT networks. (B) Frequency dependence of the linear elastic (solid symbols) and viscous (open symbols) moduli for 0.5 mg/ml pure vimentin network (black circles), 0.5 mg/ml pure MT network (orange squares), and composite vimentin-MT network (both proteins at 0.5 mg/ml, yellow symbols).

works (Fig. 7.10 A). This increase was substantial (about a factor of 2) for networks of 1 mg/ml vimentin (open triangles), but it was only slight for more dilute vimentin networks (black squares: 0.2 mg/ml, green circles: 0.5 mg/ml). The stiffness of the composite networks containing 0.1 mg/ml MTs was significantly higher than that of the corresponding pure MT network (orange squares), suggesting that vimentin dominates the elastic response. Increasing the MT concentration to 0.2 or 0.5 mg/ml decreased the stiffness of the composite networks. For 1 mg/ml vimentin networks, G' remained higher in the presence of MTs than for the pure vimentin network, but at 0.2 and 0.5 mg/ml vimentin, G' became comparable to that of the pure vimentin networks at large MT concentration.

To test whether MTs change the dynamics of stress relaxation in composite networks, we measured the frequency dependence of the linear viscoelastic moduli. Pure networks of vimentin showed an essentially frequency-independent G' over the entire range of frequencies probed, with no characteristic relaxation time. The loss tangent, which is the ratio G''/G' , was about 0.15 (Fig. 7.10 B). This behavior indicates that the vimentin networks are soft gels with solid-like behavior. In contrast, G' of pure MT networks displayed a pronounced frequency dependence, and the loss tangent was 0.29. Composite networks had an intermediate rheological behavior, though closer to that of vimentin than to that of MTs: G' was weakly dependent on frequency, and the loss tangent was 0.16.

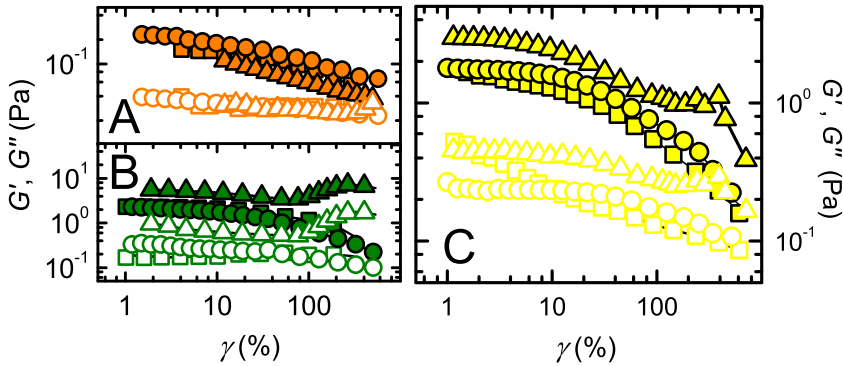


FIGURE 7.11. Nonlinear behavior of vimentin and MT networks subject to oscillatory shear at a fixed frequency of 0.5 Hz, showing the elastic (closed symbols) and viscous (open symbols) moduli. (A) Networks of pre-formed, taxol-stabilized MTs at concentrations of 0.1 (squares), 0.2 (circles) and 0.5 mg/ml (triangles) strain-soften. (B) Dilute vimentin networks (0.2 mg/ml, squares; 0.5 mg/ml, circles) strain-soften whereas 1 mg/ml networks (triangles) strain-stiffen. (C) Nonlinear behavior of composite vimentin-MT networks containing 0.5 mg/ml MTs; symbols same as in (B).

We probed the nonlinear viscoelastic response of the networks by subjecting them to large amplitude oscillatory shear at a constant oscillation frequency of 0.5 Hz. Pure MT networks responded with a very small linear regime until a critical strain amplitude of $\sim 1\%$, followed by a steady decrease of the elastic and viscous modulus with increasing strain amplitude (Fig. 7.11 A). This strain-softening behavior occurred for MT concentrations of 0.1, 0.2, and 0.5 mg/ml. These observations are consistent with earlier studies of MT rheology [183, 48], where the strain-softening behavior was ascribed to disruption of weak (nonspecific) adhesions between MTs and MT reorientation with increasing deformation. Networks composed of vimentin filaments showed two distinct types of nonlinear response depending on protein content. Dilute networks (0.2 and 0.5 mg/ml) strain-softened above a critical strain amplitude of $\sim 10\%$ while denser networks (1 mg/ml) showed a strain-stiffening response (Fig. 7.11 B). However, the increase in network stiffness in denser networks was preceded by a small dip in G' . This type of nonmonotonic behavior has also been observed for networks of desmin (a type III IF) [14]. Upon incorporation of MTs in the 1 mg/ml vimentin network, the strain-stiffening behavior was markedly suppressed. The elastic modulus was constant until a strain amplitude of $\sim 10\%$, similar to the pure vimentin system, thereafter decreased, and then slightly increased again at a strain amplitude of about 200%. The breakage strain was $\sim 300\%$, similar to that of the pure vimentin network. The presence of MTs in the more dilute vimentin networks did not noticeably affect the nonlinear, strain-softening response.

7.4 DISCUSSION AND CONCLUDING REMARKS

In this chapter, we developed a novel *in vitro* model system that will enable us in future to study the mechanical consequences of mixing different cytoskeletal filament types, specifically stiff microtubules and flexible vimentin filaments. We screened different polymerization buffer compositions to identify conditions that favor simultaneous polymerization of both filament types. We observed that both vimentin and MT assembly are very sensitive to buffer type and concentration, the presence of specific salts, and solution pH. We identified an optimal buffer composition (25 mM PIPES, 1 mM EGTA, 4 mM MgCl₂, and pH 7.0) that supports proper assembly of MTs as well as vimentin, as verified by electron microscopy. We performed first rheological experiments on both the pure and the composite networks in this buffer.

The vimentin networks behaved as weak viscoelastic solids with shear moduli of a few Pascal. The elastic modulus increased rather weakly with vimentin concentration, according to a power law with exponent 0.2. This increase is weaker than observed previously for entangled vimentin networks (exponents 0.5-1, [264, 180]) and crosslinked networks (exponent 2, [325, 182]), and weaker than theoretically predicted for networks of semiflexible polymers that are entangled (exponent 1.4, [136]) or crosslinked (exponent 2.2, [195, 94]). Prior studies of other IF systems (desmin) also showed a weaker than linear increase, with exponent 0.5 or 0.7 [264]. Vimentin networks are crosslinked by divalent cations such as Mg²⁺, which was present in our buffer [180]. It will be interesting to perform more systematic measurements of the dependence on the rheology on vimentin concentration at different Mg²⁺ concentrations. In our experiments, we used a fixed concentration of Mg²⁺, meaning that the crosslinker to vimentin molar ratio decreased with increasing vimentin concentration. This changing crosslink density could possibly contribute to the weak dependence of G' on vimentin concentration.

The enhancement of the linear elastic modulus of 1 mg/ml vimentin networks with different amounts of MTs suggests that there may potentially be direct interactions between vimentin and MTs. However, the evidence is not very strong at this stage. More systematic and extensive rheological measurements on composite networks with different compositions will be needed. Networks with equal weight concentrations of MTs and vimentin (both 0.5 mg/ml) had a stiffness comparable to that of the pure vimentin system of 0.5 mg/ml. This is consistent with prior measurements of mixtures of tissue-purified vimentin and MTs at a constant total protein concentration of 1 mg/ml [152].

Rheological measurements are an indirect indicator of filament-filament interactions. In future, it will be interesting to combine them with more direct experimental assays such as co-sedimentation assays and video microscopy tracking of filament diffusion in the composite networks. We are unaware of any literature on interactions between vimentin and MTs [266]. It has been reported however, that vimentin interacts with actin, through its tail domain [53], and that microtubules interact with neurofilaments via the long neurofilament side-arms [137].

In future it will be interesting to supplement the minimal model system

developed in this chapter with purified proteins that are known to crosslink MTs to vimentin *in vivo*, such as plectin [309, 290, 129], which is a member of the plakin family of cytolinkers. IFAP-300K protein [178, 132] is also a candidate cross-linker. Microtubule-associated protein MAP-2, which binds with high affinity to microtubules and projects long arms from the MT surface, has also been shown to interact with IFs [173, 120, 30] as well as actin [108, 107]. Motor protein such as kinesin and dynein, which *in vivo* are responsible for transporting IF precursor particles along MTs [121, 114, 237, 199, 329], could be used to study active turnover of the IF network in the presence of MTs and motor-mediated interactions [114, 174].

We observed little effect of the MTs on the nonlinear response of the vimentin networks. Networks of 0.2 and 0.5 mg/ml vimentin strain-softened, and this response was unchanged in the presence of MTs. Given the low protein density, the network deformation is likely nonaffine. With increasing strain amplitude, networks of 1 mg/ml vimentin first strain-softened slightly and then strain-stiffened. Addition of MTs made the initial strain-softening response stronger, but the subsequent strain-stiffening response remained. Thus, we did not observe reinforcement of the nonlinear response of vimentin networks by the MTs, in contrast with experiments on composite networks of actin and MTs [181]. However, more systematic measurements screening different vimentin and MT concentrations are needed to verify whether reinforcement can indeed be excluded. Another factor is the length distribution of the MTs, which is also expected to influence the transition between nonaffine and affine deformations, as shown by recent simulations [11]. It would be interesting to check how MTs of different lengths may affect the nonlinear response of the composite networks.

The data presented here are the first attempt to understand the physical principles that govern the mechanical behavior of composite IF-MT systems. A proper integration of IFs with other filament structures, including MTs and associated proteins, is necessary to maintain proper viscoelastic properties of living cells. At least 86 different human diseases arise from mutations in more than 50 different genes that encode the family of IF proteins [291, 223]. These mutations are likely to include defects in IF assembly or their interaction with other cytoskeletal components. The *in vitro* system developed in this chapter may help to bring us closer to understanding the role of molecular structure and interactions of cytoskeletal filaments in shaping cell mechanics.

I would like to thank Roland Dries, Saskia Duineveld, and Marjolein Kuit-Vinkenoog for helping me to set up and implement the purification of recombinant vimentin at AMOLF; Tatjana Wedig and Dorothee Möller (DKFZ Heidelberg) for invaluable advise and help with the vimentin purification and for performing electron microscopy; Peter Peters (NKI, Amsterdam) for kindly hosting us for electron microscopy and Martijn de Wild for helping imaging of MT-IF networks; Yvette Welling for performing particle tracking microrheology (not reported here); Svenja-Marei Kalisch, Magdalena Preciado Lopez and Marina Soares e Silva for assistance with assembly of microtubules; and Stefan Winheim (DKFZ, Heidelberg) for generously providing the vimentin labeling protocol. Finally, I thank Harald Herrmann (DKFZ, Heidelberg) for his kind hospitality, and his invaluable advise and encouragement over the years.

8 TOWARDS *in situ* VISUALIZATION OF BIOPOLYMER NETWORKS UNDER SHEAR

T HIS chapter describes the design and first testing of a home-made shear cell device. This setup combined with a confocal microscope creates a tool to visualize and quantify deformations of biopolymer networks subjected to a shear deformation on the micron scale. We illustrate the performance of the shear cell by confocal observations of fluorescently labeled fibrin coarse clots under shear. The possibility to identify network deformation mechanisms under shear will help to understand the origin of the remarkable mechanical properties of biopolymer networks, which include strain-stiffening and high extensibility. Furthermore, the shear will enable a quantitative analysis of the degree of non-affinity of the strain field in sheared gels by tracking displacements of fluorescently labeled beads embedded in the network. Finally, for sufficiently thick and rigid filaments such as fibrin or collagen fibers, it should be possible to directly observe fiber bending or stretching, and the mechanism of network rupture at large shear strain.

8.1 INTRODUCTION

Cell and tissue deformability depend on networks of protein biopolymers. These biopolymers are many orders of magnitude stiffer than typical synthetic polymers because they are built from much larger, macromolecular protein building blocks. Synthetic polymers tend to be highly flexible and act as linear springs. Their rheology is often well described by the classical rubber elastic theory, which assumes that the deformation is uniform, or affine [167, 74]. This is a good assumption for rubber-like materials, since they have a very small mesh size [257]. In case of an affine deformation, the polymers are predominantly stretched, and the network elasticity can be calculated by orientationally averaging over the entropic stretch response of the individual polymer chains. Due to the small persistence length of the chains, the force-extension behavior is linear over a wide range of applied strain, up to hundreds of percents [16]. In contrast, the mechanical response of networks of stiff biopolymers tends to be highly nonlinear, with strain-stiffening setting in already at strains of a few percent [94, 285, 195]. Moreover, simulations of stiff fiber networks in two and three dimensions show that the strain field can be highly nonaffine, and that this nonaffinity may actually cause nonlinear elasticity [118, 311, 67, 135, 144, 311, 40]. The degree of nonaffinity depends on crosslink density and filament bending stiffness. At high crosslink density, the strain field is affine (A) and the polymers are predominantly stretched. However, decreasing either the crosslink density or the bending stiffness of the fibers leads to a shift to nonaffine (NA) deformations, involving fiber bending or reorientation. Recent lattice simulations demonstrated an additional nonaffine regime where filament bending and stretching are coupled [40]. Other recent simulations showed that the crosslink density where fiber networks transition between NA and A behavior sets in is also sensitive to length polydispersity: even a small fraction of longer filaments in a network of shorter ones can shift the NA/A crossover point to lower crosslink densities [11].

While there has been much computational effort on nonaffine phenomena and shear-dependent microstructure in biopolymer networks, there has been little experimental work on real systems [190, 307, 16]. Rheology can give indirect information about the occurrence of nonaffine deformations. For instance, when the elastic modulus of a network is lower than expected on theoretical grounds in the affine limit, it is likely that nonaffinity is present. Such a discrepancy was observed in Chapter 6 for networks of collagen fibrils. However, it is not straightforward to make a quantitative comparison of experiments with theory, since this approach requires that the bending stiffness of the fibers and the network connectivity is well-known. Another indirect indication of nonaffinity is a system-size dependence of the rheology, as reported for collagen networks [8], though it is difficult to distinguish nonaffine effects from other effects such as slippage at the plates or network confinement.

A more direct experimental approach to probe nonaffinity is to map the 3D-strain field inside sheared gels by optical microscopy. The strain field can be obtained by analysis of bright field or fluorescence images of the network itself, either by extracting filament contours [282] or by cross-correlating images [295].

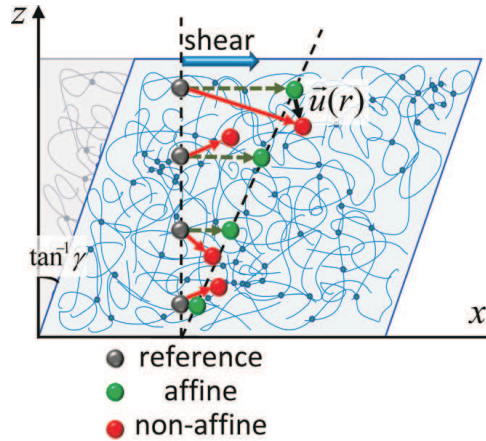


FIGURE 8.1. Schematic representation of biopolymer network subjected to an oscillatory shear in a parallel plate shear cell. The 3D strain field can be mapped by measuring displacements of embedded fluorescent tracer beads. Deviations, of the positions from an affine response (displacement in the direction of shear (x -axis), grey to green) are a measure of nonaffinity in the displacement field. γ denotes strain. Picture adapted from [16].

Alternatively, fluorescent tracer beads can be embedded in the network and tracked with sub-pixel accuracy [190, 307]. The degree of nonaffinity can be deduced from the deviation of bead displacements from the imposed macroscopic shear, and from the angle and relative position of particle pairs before and after shear (Fig. 8.1). Such a bead-tracking approach was used to show that F-actin networks crosslinked by small rigid crosslink proteins deform increasingly non-affinely when the crosslink density or the length of the filaments is decreased, consistent with numerical predictions [190]. Actin networks crosslinked by the flexible crosslinking protein filamin were shown to display filament alignment under shear [189] while fibrin networks become less nonaffine with increasing applied strain amplitude, reflecting entropic origin of the nonlinear elasticity [307]. In contrast, the degree of nonaffinity in gels of flexible polyacrylamide chains was shown to be independent of the density of polymer chains or crosslinks [16]. The nonaffinity in this system was ascribed to structural inhomogeneities introduced during gel preparation.

Strain field mapping of sheared networks by optical microscopy requires shear cells with at least one glass plate that is transparent for visible light. Two different categories of shear cell geometries have been developed. The first category is that of parallel plate shear cells, where the sample is sheared by translating two parallel plates that are larger than their separation relative to each other. This geometry was used for quantifying nonaffinity in actin networks [190] and for imaging of colloidal suspensions under flow [1, 2, 63, 319, 117, 116, 62, 276, 23, 24]. Planar shear is convenient for oscillatory measurements but is unsuitable for flow (continuous shear) experiments since only a finite strain can

be achieved. Rotational geometries, which are used in traditional rheometers, are more flexible, allowing both oscillatory and continuous shear measurements. Such a system equipped with a counter-rotating cone and plate [70, 319, 318, 34, 217] or plate-plate cell [109, 25, 248] was used for colloidal suspensions. The advantage of counter-rotating plates, which move in opposite directions, is that a zero velocity plane is situated at a gap height that depends on the relative velocities of the two plates. Sheared objects can be conveniently imaged in this stationary plane without moving out of the field of view. Most shear cells to date were custom-built, but recently several groups placed rotational rheometers on top of a microscope, so that simultaneous measurements of the shear stress can be made [263, 307, 23, 16, 24, 31].

We decided to build a parallel plate shear cell with one stationary and one translating plate. The parallel plate design is convenient for crosslinked biopolymer networks, for which we use almost exclusively oscillatory tests. The cell was designed for small sample volumes, which is important since we work with purified proteins that are generally obtained in small yields. Moreover, we implemented temperature and humidity control, in order to maintain physiological 37 °C conditions. The cell was designed to access a large frequency range (<0.1 to 100 Hz), similar to that accessible by standard bulk rheology. Furthermore, the cell can reach, depending on gap size, large strain amplitudes of up to 2000%. This covers the high strain regimes at which stretching of extensible fibers such as fibrin and intermediate filaments can be observed, as well as ventual network rupture.

This chapter describes the design of this new shear cell device, which can be placed on a confocal microscope to image changes in the microstructure of biopolymer networks in response to an applied shear over a large range of frequencies and strain amplitudes. We demonstrate the performance of this setup by test experiments with fluorescently labeled fibrin networks. Combined with rheometry, which provides the macroscopic network stiffness, this new device can provide new insights into the mechanisms that govern the highly nonlinear response of the biopolymer networks that structure living cells and tissues.

8.2 PARALLEL PLATE SHEAR CELL

To visualize changes in the structure of biopolymer networks in response to a macroscopic shear deformation on microscopic length scales, we designed a shear cell (SC) with two glass plates. The cell can be mounted directly on top of a Leica (Leica Microsystems, Rijswijk, Netherlands) inverted spinning (Nipkow) disc confocal microscope (Fig. 8.2 A). The spinning disc permits fast confocal scanning at frame rates of hundreds frames per second [316]. The sample is confined between a moveable top plate, and a stationary bottom plate, through which it can be imaged using a high numerical aperture, 100x oil immersion objective. The two main components of the shear cell device are: (1) a cylindrical fixture with movable shaft that provides the shearing motion and (2) a position sensor (optoNCDT, Micro-Epsilon Messtechnik, Ortenburg, Germany)

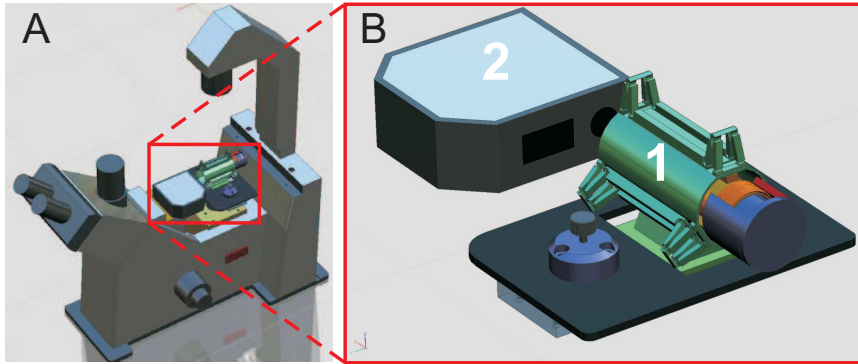


FIGURE 8.2. Schematic view of setup for visualization of biopolymer networks under macroscopic shear. (A) Shear cell placed on top of a Leica inverted confocal microscope. (B) Close-up of the shear cell, showing its two main parts: 1-movable shaft and 2-position sensor.

that records the displacement of the top plate (Fig. 8.2 B).

The movable shaft consists of a titanium (grade 5) hinge spring system, placed on a core tube and protected by a metal casing (Fig. 8.2 B). The hinge spring system is connected at the bottom with a plastic holder for the top microscope coverslip (Fig. 8.3 C). The movement of the SC is based on the Lorentz force principle. An applied electric current induces a magnetic field between two magnets (Fig. 8.3 A). The home-made voice coil (84 coils separated with 0.4 mm distance) that is wound on one side of the core tube is then pushed back and forth, in and out of the magnetic field produced by the Neodymium magnets (grade N52). Since the hinge spring system is mounted directly on the core tube and is connected with the top coverslip holder, it will move the top plate and produce a shear in the direction parallel to the bottom glass slide.

Both glass plates are microscope coverslips of $24 \times 32 \text{ mm}^2$ with a thickness of 0.15 mm (#1.5 coverslips, Marienfeld Laboratory Glassware, Germany). They are held in place by metal bars with screws on the two shorter sides and are easily exchangeable. A micrometer screw mounted on the bottom metal glass holder (Fig. 8.3 D) can be used to adjust the gap distance between the plates over a range of 0 to $800 \mu\text{m}$. Alignment of the slides parallel with each other is achieved by adjusting three screw legs mounted on the bottom part of the hinge spring system casing (Fig. 8.3 C). The distance between the plates at different xy-locations within the focal planes was measured with the z-focus of the microscope objective. Fluorescently labeled particles with a diameter of $1 \mu\text{m}$ stuck to the bottom and top coverslip were imaged by confocal microscopy and used as a reference for plate alignment. The shear cell legs were adjusted until the height variation between the two plates over the whole coverslip area was less than $2 \mu\text{m}$.

To enable experiments at physiological temperatures of 37°C , the bottom glass slide holder was equipped with several surface-mounted power resistors

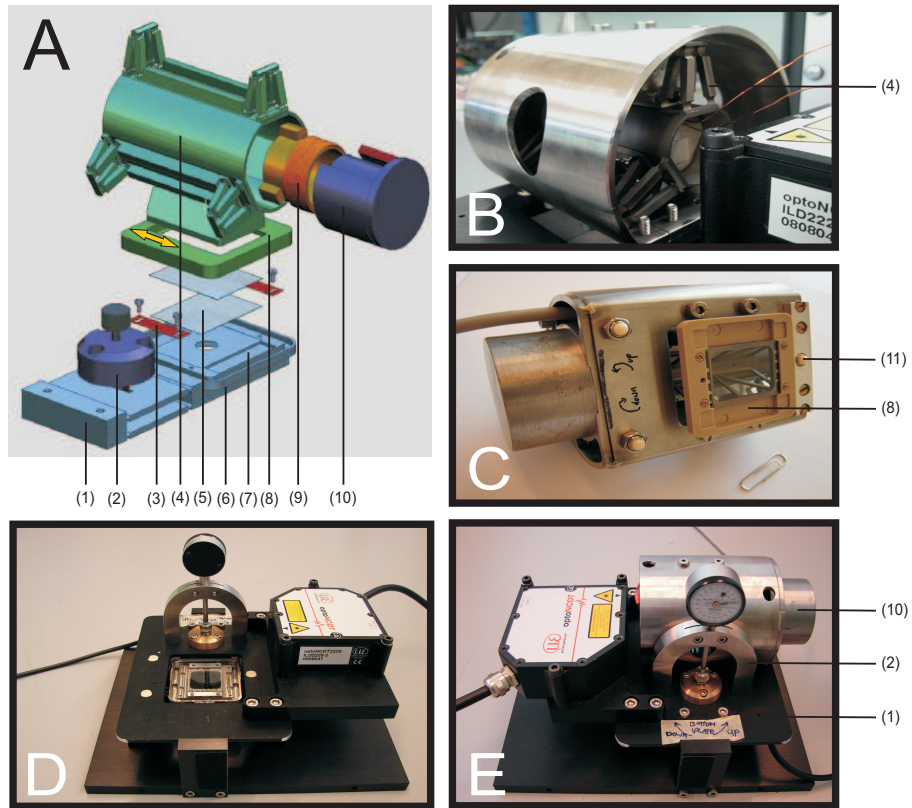


FIGURE 8.3. Shear cell (SC) design. (A) Schematic representation of the individual SC components: (1) SC bottom plate, (2) micrometer screw for gap adjustment, (3) metal bar with screws to hold the bottom microscope coverslip, (4) hinge spring system, (5) bottom glass coverslip, (6) temperature control sensors, (7) solvent trap filled with water, (8) movable holder with the top microscope glass slide, (9) core tube with voice coil, (10) two magnets, (11) screw leg(s) for parallel alignment of the two glass coverslips. (B) Photograph of the metal core with the hinge spring system surrounded by metal casing. (C) Bottom view of the hinge-spring system, showing the movable top glass holder with a glass slide and three screw legs used to align the plates. (D) Photograph of the shear cell bottom plate with position sensor, micrometer screw and bottom glass slide holder. (E) Photograph of the fully assembled shear cell.

(SMD) and 3 temperature sensors (TSIC506FTB, Zentrum Mikroelektronik Dresden, Germany). Due to thermal conduction along the metal holder, an equal temperature is maintained all around the sample. To minimize evaporation, rectangular wells were cut in the bottom glass holder which could be filled with water. This water reservoir maintains moist conditions and also helps to improve the temperature gradient all around the sample. The fully assembled shear cell is shown in Fig. 8.3 E.

8.3 ELECTRONICS AND SOFTWARE INTERFACE TO CONTROL SHEAR DEFORMATION

Shear cell movement is controlled by a programmable sine-wave generator and a closed loop feedback system, both implemented in digital hardware (National Instruments Reconfigurable I/O, Austin, TX). With this generator we can apply an oscillatory shear, a constant strain, or a superposition of the two, either in a continuous or a step-wise manner. The feedback system is a proportional-integral-derivative regulator (PID) that compares the current position, which is measured with a laser position sensor (optoNCDT, Micro-Epsilon Messtechnik, Ortenburg, Germany), with the desired position from the sine-generator and outputs the required current to move the shaft to the desired position. The current is by definition equivalent in this case to the force based on the Lorentz force equation:

$$\vec{F} = q\vec{V} \times \vec{B} = q\frac{d\vec{l}}{dt} \times \vec{B} = \vec{I} dl \times \vec{B}, \quad (8.1)$$

where F is a sum of the forces necessary to overcome the inertia of the motor and plate, the force to shear the sample, and the force to move the hinge spring system. Further, q is electrical charge, V is voltage, B is magnetic induction and I is applied current, which is in the presence of spring system linear with F and with displacement. This is in contrast to a normal voice-coil system, where I is linear with F and with acceleration. The force required to move the shaft is much larger (around 9 N) than the force generated by the sample itself, which is expected to be in the pN range assuming that $F = \sigma A$, where σ denotes stress in units of Pa and A is the microscopic filament area that is approximately equal to squared network mesh size, ξ^2 (μm)². Therefore, we did not attempt to extract shear stresses from the force needed to drive the plate.

The two parameters that can be tuned during an experiment are the frequency and the amplitude of the shear. The maximum relative plate translation along the x axis is 2 mm, for frequencies below 20 Hz. With gap sizes of 400 μm , this means that we can apply strains up to 500%, which is well within the range that is relevant for biopolymer networks, even including extremely resilient materials such as fibrin and intermediate filaments, which have breakage strains of 200-300%. The maximum frequency that can be applied is 100 Hz, with a displacement of at most 100 μm . The system has a mechanical resonance frequency of 37 Hz.

To control the shear cell and visualize the data we developed software that can control the temperature, PID parameters, program the desired movement, and record the shaft motion over time. The actual shaft position, desired position, and driver current can be measured every 50 μs . The program can visualize the data as time-series graphs, power spectra, and Lissajous curves. Higher harmonic terms in the power spectrum and non-ellipsoidal shapes of the Lissajous curves can be indicative of rheological nonlinearities (see Chapter 5). However, the driver output does not correspond directly to the force generated by the sample during shearing, so the nonlinearities cannot be quantified.

The software can also automatically record images of the sheared sample in one focal plane at a time, by interfacing with a black-illuminated cooled EM-CCD camera (C9100, Hamamatsu Photonics, Herrsching an Ammersee, Germany) on the microscope. In future, we plan to extend the software for automated collection of z-stacks over time. This will be necessary to determine the 3D network structure and to measure the strain field with the use of beads embedded inside the network.

8.4 FIBRIN NETWORK UNDER SHEAR

To demonstrate the performance of the shear cell, we polymerized a coarse fibrin network with a protein concentration of 0.5 mg/ml ($G' = 4.7$ Pa, $G'' = 0.58$ Pa, $\xi \sim 4$ μm) in the shear cell, using a gap distance of 70 μm between the plates. A drop of fibrinogen solution of which 10% was labeled with Alexa488 was confined between the parallel glass plates and polymerized for 2 hours on the microscope.

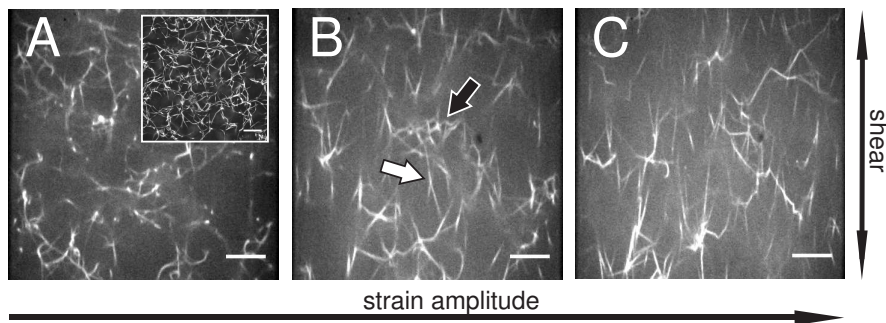


FIGURE 8.4. Polymerized 0.5 mg/ml fibrin network before shear (A) and during oscillatory shear at 0.5 Hz and increasing strain amplitude: 160% (B) and 280% (C). Images represent single planes. *Inset* in (A) shows maximum intensity projection of a z-stack of 101 planes over a depth of 10 μm . Scale bars, 10 μm .

Directly after polymerization (before shear), the network consisted of long, thermally undulated filaments (Fig. 8.4 A). The network appears to be slightly inhomogeneous when looking at a single plane. This is typical at the rather low protein concentration in this experiment. Three-dimensional image stacks obtained by scanning through the z-direction show that the fibers in fact do form a fully connected network (inset of Fig. 8.4 A). When an oscillatory shear of 160% strain and 0.05 Hz is applied, the fibrin network is visibly stretched (Fig. 8.4 B). Individual filaments are aligned and elongated along the shear direction. Depending on the filament orientation, filaments are compressed (black arrow) or extended (white arrow). Individual fibers oriented out of plane continuously appear and disappear from the imaged focal plane during oscillations, depending on their orientation with respect to the shear direction. At strains

of 280%, highly stretched filaments were observed (Fig. 8.4 C). At even higher strain amplitudes, filaments detached from the glass surfaces before we were able to observe any fiber rupture. Therefore, in future it is recommended to coat the glass surface in order to prevent network slip at high shear.

8.5 CONCLUSIONS AND OUTLOOK

In this chapter we presented a new custom-built shear cell device which can be used to visualize changes in the microstructure of biopolymer networks under shear. This tool complements bulk rheological studies and can be used to quantify the degree of nonaffinity in the mechanical response. Further modifications of the system are however needed to optimize its performance. This includes improvement of the setup itself as well as in the software interface.

Regarding improvements to the hardware, there are several issues. Manual alignment of the glass plates with the use of screw legs using fluorescence beads as a reference for the top and bottom plates, which is done in the current design, is not very accurate and rather laborious. In future it would be better to implement automated adjustment of the gap to the desired size and tilt goniometers or pivot system to ensure parallelism [319, 276]. Furthermore, with the current design it is difficult to maintain a constant and homogeneous distance between the glass plates during experiments, due to forces exerted on the plates by the sample during polymerization. These forces pull the thin coverslips towards one another, decreasing the gap and potentially bending the plates. Possible solution here is to exchange the top coverslip with a thicker glass slide, or to use spacers that guarantee a constant distance between the coverslips over the entire sample area. However, spacers may generate additional friction during sample shearing. We observed that the stability of the gap depends on the amount of sample between the plates. A small sample volume compared to the total shear cell capacity may create a liquid meniscus, introducing capillary forces that pull the plates together. Therefore, it is important to fill the entire cell with sample. Another problem with the current design is that is difficult to maintain moist conditions and prevent solvent evaporation for 37 °C experiments that take longer than 1-2 hours. Once the sample is loaded and the setup is closed, there is no easy way to refill the water in the solvent trap. This is problematic for assembly of some proteins such as fibrin and collagen, for which polymerization takes longer than 2 hours. Therefore, additional elements to ensure a saturated water atmosphere during measurements are required. Finally, the current device can apply a deformation but not measure the shear stress. In future, we plan to add a force sensor to the bottom plate of the shear cell to measure the shear stress directly. Knowledge of the shear stress is crucial to quantify the nonlinear viscoelastic response of the sample that accompanies the structural changes seen by confocal microscopy.

Regarding the software, it will be useful to synchronize shearing with acquisition of time- and/or z-stacks. This would enable 3D reconstruction of deformed networks under shear, in order to visualize deformations of filaments or quantify the 3D strain field. Strain-field mapping and network visualization are

needed to obtain a full understanding of the origin of the nonlinear mechanics of biopolymer networks.

I would like to thank Mel Bacabac for his key contributions to the development of the shear cell and the joint preliminary experiments; Erik Claij (AMOLF Electronics Engineering) and Dirk-Jan Spaanderman (AMOLF Mechanical Design Engineering) for the shear cell design; the AMOLF Mechanical Workshop for project realization, in particular Jan van der Linden who made the hinge-spring system; and Marco Seynen (AMOLF Software Engineering) for development of the shear cell software. Finally, I would like to thank Dirk-Jan, Erik, and Marco for proofreading this chapter and for all technical corrections.

BIBLIOGRAPHY

1. B. J. Ackerson. Shear induced order of hard sphere suspensions. *J. Phys.: Condens. Matter*, 2:SA389–SA392, 1990.
2. B. J. Ackerson and N. A. Clark. Shear-induced melting. *Phys Rev Lett*, 46:123–126, 1981.
3. E. Adachi and T. Hayashi. In vitro formation of hybrid fibrils of type V collagen and type I collagen. Limited growth of type I collagen into thick fibrils by type V collagen. *Connect Tissue Res*, 14(4):257–266, 1986.
4. P. M. Ajayan and J. M. Tour. Materials science: nanotube composites. *Nature*, 447(7148):1066–1068, 2007.
5. B. Alberts, A. Johnson, J. Lewis, M. Raff, K. Roberts, and P. Walter. *Molecular Biology of the Cell*, 4th edition. New York: Garland Science, 2002.
6. J. L. Andresen, T. Ledet, H. Hager, K. Josephsen, and N. Ehlers. The influence of corneal stromal matrix proteins on the migration of human corneal fibroblasts. *Exp Eye Res*, 71(1):33–43, 2000.
7. K. Andrikopoulos, X. Liu, D. R. Keene, R. Jaenisch, and F. Ramirez. Targeted mutation in the col5a2 gene reveals a regulatory role for type V collagen during matrix assembly. *Nat Genet*, 9(1):31–36, 1995.
8. R. C. Arevalo, J. S. Urbach, and D. L. Blair. Size-dependent rheology of type-I collagen networks. *Biophysical Journal*, 99:L65–L67, 2010.
9. L. E. Averett, C. B. Geer, R. R. Fuieler, B. B. Akhremitchev, O. V. Gorkun, and M. H. Schoenfish. Complexity of A-a knob-hole fibrin interaction revealed by atomic force spectroscopy. *Langmuir*, 24:4979–4988, 2008.
10. M. Bai, A. R. Missel, W. S. Klug, and A. J. Levine. The mechanics and affine-nonaffine transition in polydisperse semiflexible networks. *Soft Matter*, 7:907–914, 2011.
11. M. Bai, A. R. Missel, A. J. Levine, and W. S. Klug. On the role of the filament length distribution in the mechanics of semiflexible networks. *Acta Biomater*, 7(5):2109–2118, 2011.
12. K. Bailey, W. T. Astbury, and K. M. Rudall. Fibrinogen and fibrin as a members of the keratin-myosin group. *Nature*, 151:716–717, 1943.

13. M. D. Bale and J. D. Ferry. Strain enhancement of elastic modulus in fine fibrin clots. *Thromb Res*, 52(6):565–572, 1988.
14. H. Bar, M. Schopferer, S. Sharma, B. Hochstein, N. Mucke, H. Herrmann, and N. Willenbacher. Mutations in desmin’s carboxy-terminal ”tail” domain severely modify filament and network mechanics. *J Mol Biol*, 397(5):1188–1198, 2010.
15. C. Baravian and D. Quemada. Using instrumental inertia in controlled stress rheometry. *Rheol Acta*, 37:223–233, 1998.
16. A. Basu, Q. Wen, X. Mao, T. C. Lubensky, P. A. Janmey, and A. G. Yodh. Nonaffine displacements in flexible polymer networks. *Macromolecules*, 44:16711679, 2011.
17. M. Bathe, C. Heussinger, M. M. A. E. Claessens, A. R. Bausch, and E. Frey. Cytoskeletal bundle mechanics. *Biophys J*, 94:2955–2964, 2008.
18. R. Beck, J. Deek, M. C. Choi, T. Ikawa, O. Watanabe, E. Frey, P. Pincus, and C. R. Safinya. Unconventional salt trend from soft to stiff in single neurofilament biopolymers. *Langmuir*, 26(24):18595–18599, 2010.
19. E. Bell, B. Ivarsson, and C. Merrill. Production of a tissue-like structure by contraction of collagen lattices by human fibroblasts of different proliferative potential in vitro. *PNAS*, 76(3):1274–1278, 1979.
20. P. M. Bendix, G. H. Koenderink, D. Cuvelier, Z. Dogic, B. N. Koeleman, W. M. Briher, C. M. Field, L. Mahadevan, and D. A. Weitz. A quantitative analysis of contractility in active cytoskeletal protein networks. *Biophys J*, 94:3126–3136, 2008.
21. A. D. Berendsen, A. L. J. J. Bronckers, T. H. Smit, X. F. Walboomers, and V. Everts. Collagen type V enhances matrix contraction by human periodontal ligament fibroblasts seeded in three-dimensional collagen gels. *Matrix Biol*, 25(8):515–522, 2006.
22. S. Bernocco, F. Ferri, A. Profumo, C. Cuniberti, and M. Rocco. Polymerization of rod-like macromolecular monomers studied by stopped-flow, multiangle light scattering: set-up, data processing, and application to fibrin formation. *Biophys J*, 79(1):561–583, 2000.
23. R. Besseling, L. Isa, E. R. Weeks, and W. C. K. Poon. Quantitative imaging of colloidal flows. *Adv Colloid Interface Sci*, 146(1-2):1–17, 2009.
24. R. Besseling, E. R. Weeks, A. B. Schofield, and W. C. K. Poon. Three-dimensional imaging of colloidal glasses under steady shear. *Phys Rev Lett*, 99(2):028301, 2007.
25. R. Biehl and T. Palberg. Modes of motion in a confined colloidal suspension under shear. *Europhys. Lett.*, 66:291–295, 2004.

26. D. E. Birk. Type V collagen: heterotypic type I/V collagen interactions in the regulation of fibril assembly. *Micron*, 32(3):223–237, 2001.
27. D. E. Birk, J. M. Firch, and T. F. Linsenmayer. Organization of collagen types I and V in the embryonic chicken cornea. *Invest Ophthalmol Vis Sci*, 27:1470–1477, 1986.
28. D. E. Birk, J. M. Fitch, J. P. Babiarz, K. J. Doane, and T. F. Linsenmayer. Collagen fibrillogenesis in vitro: interaction of types I and V collagen regulates fibril diameter. *J Cell Sci*, 95:649–657, 1990.
29. D. E. Birk, J. M. Fitch, J. P. Babiarz, and T. F. Linsenmayer. Collagen type I and type V are present in the same fibril in the avian corneal stroma. *J Cell Biol*, 106(3):999–1008, 1988.
30. G. S. Bloom, F. C. Luca, and R. B. Vallee. Cross-linking of intermediate filaments to microtubules by microtubule-associated protein 2. *Ann N Y Acad Sci*, 455:18–31, 1985.
31. P. E. Boukany, O. Hemminger, S. Q. Wang, and L. J. Lee. Molecular imaging of slip in entangled dna solution. *Phys Rev Lett*, 105(2):027802, 2010.
32. C. P. Brangwynne, F. C. MacKintosh, S. Kumar, N. A. Geisse, J. Talbot, L. Mahadevan, K. K. Parker, D. E. Ingber, and D. A. Weitz. Microtubules can bear enhanced compressive loads in living cells because of lateral reinforcement. *J Cell Biol*, 173(5):733–741, 2006.
33. C. P. Brangwynne, F. C. MacKintosh, and D. A. Weitz. Force fluctuations and polymerization dynamics of intracellular microtubules. *Proc Natl Acad Sci U S A*, 104(41):16128–16133, 2007.
34. V. Breedveld, D. van den Ende, M. Bosscher, R. J. Jongschaap, and J. Mellema. Measuring shear-induced self-diffusion in a counterrotating geometry. *Phys Rev E*, 63:021403, 2001.
35. R. G. M. Breuls, D. D. Klumpers, V. Everts, and T. H. Smit. Collagen type V modulates fibroblast behavior dependent on substrate stiffness. *Biochem Biophys Res Commun*, 380:425–429, 2009.
36. J. Brinckmann, H. Notbohm, and P. Muller. *Collagen - Primer in Structure, Processing, and Assembly*. Springer, 2005.
37. B. R. Brinkley, S. M. Cox, D. A. Pepper, L. Wible, S. L. Brenner, and R. L. Pardue. Tubulin assembly sites and the organization of cytoplasmic microtubules in cultured mammalian cells. *J Cell Biol*, 90(3):554–562, 1981.
38. G. W. Brodland and R. Gordon. Intermediate filaments may prevent buckling of compressively loaded microtubules. *J Biomech Eng*, 112(3):319–321, 1990.

39. C. P. Broedersz, K. E. Kasza, L. M. Jawerth, S. Muenster, D. A. Weitz, and F. C. MacKintosh. Nonlinear rheology of cross linked biopolymer gels. *Soft Matter*, 6:4120, 2010.
40. C. P. Broedersz, X. Mao, T. C. Lubensky, and F. C. MacKintosh. Criticality and isostaticity in fiber networks. *Soft Condensed Matter*, arXiv:1011.6535v1.
41. C. P. Broedersz, C. Storm, and F. C. MacKintosh. Nonlinear elasticity of composite networks of stiff biopolymers with flexible linkers. *Phys Rev Lett*, 101(11):118103, 2008.
42. J. L. Brokaw, C. J. Doillon, R. A. Hahn, D. E. Brik, R. A. Berg, and F. H. Silver. Turbidimetric and morphological studies of type I collagen fiber self assembly in vitro and the influence of fibronectin. *Journal of Biological Macromolecules*, 7:135–140, 1985.
43. A. E. X. Brown, R. Litvinov, D. E. Discher, and J. W. Weisel. Forced unfolding of coiled-coils in fibrinogen by single-molecule AFM. *Biophys J*, 92:L39–L41, 2007.
44. A. E. X. Brown, R. I. Litvinov, D. E. Discher, P. K. Purohit, and J. W. Weisel. Multiscale mechanics of fibrin polymer: Gel stretching with protein unfolding and loss of water. *Science*, 325:741–744, 2009.
45. M. J. Buehler. Nature designs tough collagen: Explaining the nanostructure of collagen fibrils. *PNAS*, 103:1228512290, 2006.
46. M. J. Buehler and Y. C. Yung. Deformation and failure of protein materials in physiologically extreme conditions and disease. *Nat Mater*, 8(3):175–188, 2009.
47. C. Bustamante, J. F. Marko, E. D. Siggia, and S. Smith. Entropic elasticity of lambda-phage DNA. *Science*, 265:1599, 1994.
48. R. E. Buxbaum, T. Dennerll, S. Weiss, and S. R. Heidemann. F-actin and microtubule suspensions as indeterminate fluids. *Science*, 235(4795):1511–1514, 1987.
49. G. A. Buxton and N. Clarke. Bending to stretching transition in disordered networks. *Phys Rev Lett*, 98:238103, 2007.
50. W. J. Cantwell and J. Morton. The impact resistance of composite materials - a review. *Composites*, 22:347–362, 1991.
51. M. E. Carr, D. A. Gabriel, and J. MacDonagh. Influence of factor XIII and fibronectin on fiber size and density in thrombin-induced fibrin gels. *J Lab Clin Med*, 110:747–752, 1987.
52. M. E. Carr and J. Hermans. Size and density of fibrin fibers from turbidity. *Macromolecules*, 11:46–50, 1978.

53. R. B. Cary, M. Klymkowsky, R. M. Evans, A. Domingo, J. A. Dent, and L. E. Backhus. Vimentin's tail interacts with actin-containing structures in vivo. *J Cell Sci*, 107:1609–1622, 1994.
54. P. L. Chandran and V. H. Barocas. Affine versus non-affine fibril kinematics in collagen networks: theoretical studies of network behavior. *J Biomech Eng*, 128(2):259–270, 2006.
55. L. Chang and R. D. Goldman. Intermediate filaments mediate cytoskeletal crosstalk. *Nat Rev Mol Cell Biol*, 5(8):601–613, 2004.
56. H. Chanut-Delalande, A. Fichard, S. Bernocco, R. Garrone, D. J. Hulmes, and F. Ruggiero. Control of heterotypic fibril formation by collagen V is determined by chain stoichiometry. *J Biol Chem*, 276(26):24352–24359, 2001.
57. O. Chaudhuri, S. H. Parekh, and D. A. Fletcher. Reversible stress softening of actin networks. *Nature*, 445(7125):295–298, 2007.
58. M. A. Chernousov, R. C. Stahl, and D. J. Carey. Schwann cell type V collagen inhibits axonal outgrowth and promotes Schwann cell migration via distinct adhesive activities of the collagen and noncollagen domains. *J Neurosci*, 21(16):6125–6135, 2001.
59. K. S. Cho. A geometrical interpretation of large amplitude oscillatory shear response. *J. Rheol*, 49:747–758, 2005.
60. Y. H. Chou, F. W. Flitney, L. Chang, M. Mendez, B. Grin, and R. D. Goldman. The motility and dynamic properties of intermediate filaments and their constituent proteins. *Exp Cell Res*, 313(10):2236–2243, 2007.
61. M. M. A. E. Claessens, M. Bathe, E. Frey, and A. R. Bausch. Actin-binding proteins sensitively mediate F-actin bundle stiffness. *Nat Mater*, 5:748–753, 2006.
62. I. Cohen, B. Davidovitch, A. B. Schofield, M. P. Brenner, and D. A. Weitz. Slip, yield, and bands in colloidal crystals under oscillatory shear. *Phys Rev Lett*, 97(21):215502, 2006.
63. I. Cohen, T. G. Mason, and D. A. Weitz. Shear-induced configurations of confined colloidal suspensions. *Phys Rev Lett*, 93(4):046001, 2004.
64. J. P. Collet, J. L. Moen, Y. I. Veklich, O. V. Gorkun, S. T. Lord, G. Montalescot, and J. W. Weisel. The alpha-C domains of fibrinogen affect the structure of the fibrin clot, its physical properties, and its susceptibility to fibrinolysis. *Blood*, 106:3824–3830, 2005.
65. J. P. Collet, H. Shuman, R. E. Ledger, S. Lee, and J. W. Weisel. The elasticity of an individual fibrin fiber in a clot. *PNAS*, 102:9133–9137, 2005.

66. C. Conde and A. Caceres. Microtubule assembly, organization and dynamics in axons and dendrites. *Nat Rev Neurosci*, 10(5):319–332, 2009.
67. E. Conti and F. C. MacKintosh. Cross-linked networks of stiff filaments exhibit negative normal stress. *Phys Rev Lett*, 102:088102, 2009.
68. M. Das, A. J. Levine, and F. C. MacKintosh. Buckling and force propagation along intracellular microtubules. *EPL*, 84:18003–p1, 2008.
69. M. Das and F. C. Mackintosh. Poisson’s ratio in composite elastic media with rigid rods. *Phys Rev Lett*, 105(13):138102, 2010.
70. D. Derks, H. Wisman, A. van Blaaderen, and A. Imhof. Confocal microscopy of colloidal dispersions in shear flow using a counter-rotating coneplate shear cell. *J. Phys.: Condens. Matter*, 16:S3917–S3927, 2004.
71. B. A. DiDonna and A. J. Levine. Filamin cross-linked semiflexible networks: fragility under strain. *Phys Rev Lett*, 97(6):068104, 2006.
72. B. A. DiDonna and T. C. Lubensky. Nonaffine correlations in random elastic media. *Phys Rev E*, 72:066619, 2005.
73. R. F. Doolittle and J. M. Kollman. Natively unfolded regions of the vertebrate fibrinogen molecule. *Proteins*, 63:391–397, 2006.
74. S. F. Edwards. The theory of rubber elasticity. *Proc. R Soc Lond. A*, 351:397–406, 1976.
75. A. J. Engler, S. Sen, H. L. Sweeney, and D. E. Discher. Matrix elasticity directs stem cell lineage specification. *Cell*, 126(4):677–689, 2006.
76. O. Esue, A. A. Carson, Y. Tseng, and D. Wirtz. A direct interaction between actin and vimentin filaments mediated by the tail domain of vimentin. *J Biol Chem*, 281(41):30393–30399, 2006.
77. R. H. Ewoldt. *Rheology of Complex Fluid Films for Biological and Mechanical Adhesive Locomotion*. PhD thesis, Massachusetts Institute of Technology, 2006.
78. R. H. Ewoldt, C. Clasen, A. E. Hosoi, and G. H. McKinley. Rheological fingerprinting of gastropod pedal mucus and synthetic complex fluids for biomimicking adhesive locomotion. *Soft Matter*, 3:634–643, 2007.
79. R. H. Ewoldt, A. E. Hosoi, and G. H. McKinley. New measures for characterizing nonlinear viscoelasticity in large amplitude oscillatory shear. *Journal of Rheology*, 52:doi:10.1122/1.2970095, 2008.
80. R. H. Ewoldt and G. H. McKinley. Creep ringing in rheometry or how to deal with oft-discarded data in step stress tests. *Rheology Bulletin*, 76:4–24, 2007.

81. R. H. Ewoldt, G. H. McKinley, and A. E. Hosoi. Fingerprinting soft materials: A framework for characterizing nonlinear viscoelasticity. *Soft Condensed Matter*, DOI: 10.1122/1.2970095.
82. M. R. Falvo, D. Millard, E. T. O'Brien, R. Superfine, and S. T. Lord. Length of tandem repeats in fibrins alpha-C region correlates with fiber extensibility. *J Thromb Haemost*, 6:1991–1993, 2008.
83. E. Farge and A. C. Maggs. Dynamic scattering from semiflexible polymers. *Macromolecules*, 26:5041–5044, 1993.
84. P. Fernandez, P. A. Pullarkat, and A. Ott. A master relation defines the nonlinear viscoelasticity of single fibroblasts. *Biophys J*, 90(10):3796–3805, 2006.
85. J. D. Ferry and P. R. Morrison. Preparation and properties of serum and plasma proteins. VIII. The conversion of human fibrinogen to fibrin under various conditions. *J Am Chem Soc*, 69:388–400, 1947.
86. A. Fichard, J. P. Kleman, and F. Ruggiero. Another look at collagen V and XI molecules. *Matrix Biology*, 14:515–531, 1994.
87. M. Fixman and J. Kovac. Polymer conformational statistics. III. Modified Gaussian models of stiff chains. *J Chem Phys*, 58:1564–1568, 1973.
88. W. E. Fowler, R. R. Hantgan, J. Hermans, and H. P. Erickson. Structure of the fibrin protofibril. *PNAS*, 1981:4872–4876, 1978.
89. E. Fuchs and K. Weber. Intermediate filaments: structure, dynamics, function, and disease. *Annu Rev Biochem*, 63:345–382, 1994.
90. D. Fudge, D. Russell, D. Beriault, W. Moore, E. B. Lane, and A. W. Vogl. The intermediate filament network in cultured human keratinocytes is remarkably extensible and resilient. *PLoS One*, 3(6):e2327, 2008.
91. E. Fukada and M. Kaibara. The dynamic rigidity of fibrin gels. *Biorheology*, 10:129–138, 1973.
92. D. K. Fygenson, E. Braun, and A. Libchaber. Phase diagram of microtubules. *Phys. Rev. E*, 50:15791588, 1994.
93. S. N. Ganeriwala and C. A. Rotz. Fourier transform mechanical analysis for determining the nonlinear viscoelastic properties of polymers. *Polym Eng Sci*, 27:165–178, 1987.
94. M. L. Gardel, J. H. Shin, F. C. MacKintosh, L. Mahadevan, P. Matsudaira, and D. A. Weitz. Elastic behavior of cross-linked and bundled actin networks. *Science*, 304:1301–1305, 2004.
95. C. Gerth, W. W. Roberts, and J. D. Ferry. Rheology of fibrin clots. II. Linear viscoelastic behavior in shear creep. *Biophys Chem*, 2:208–217, 1974.

96. F. Gittes and F. C. MacKintosh. Dynamic shear modulus of a semiflexible polymer network. *Phys Rev E*, 58:R1241–R1244, 1998.
97. F. Gittes, B. Mickey, J. Nettleton, and J. Howard. Flexural rigidity of microtubules and actin filaments measured from thermal fluctuations in shape. *J Cell Biol*, 120(4):923–934, 1993.
98. F. Gittes, B. Schnurr, P. D. Olmsted, F. C. MacKintosh, and C. F. Schmidt. Microscopic viscoelasticity: Shear moduli of soft materials determined from thermal fluctuations. *Phys Rev Lett*, 17:3286–3289, 1997.
99. C. J. Glover, L. V. McIntire, C. H. Brown, and E. A. Natelson. Rheological properties of fibrin clots. Effects of fibrinogen concentration, Factor XIII deficiency, and Factor XIII inhibition. *J Lab Clin Med*, 86:644–656, 1975.
100. L. M. Godsel, R. P. Hobbs, and K. J. Green. Intermediate filament assembly: dynamics to disease. *Trends Cell Biol*, 18(1):28–37, 2008.
101. J. P. Gong. Why are double network hydrogels so tough? *Soft Matter*, 6:DOI: 10.1039/B924290B, 2010.
102. O. V. Gorkun, Y. I. Veklich, L. V. Medved, A. H. Henschen, and J. W. Weisel. Role of the alpha-C domains of fibrin in clot formation. *Biochemistry*, 33:6986–6997, 1994.
103. J. S. Graham, A. N. Vomund, C. L. Phillips, and M. Grandbois. Structural changes in human type I collagen fibrils investigated by force spectroscopy. *Exp Cell Res*, 299(2):335–342, 2004.
104. R. Granek. From semi-flexible polymers to membranes: Anomalous diffusion and reptation. *J Phys II*, 7:1761–1788, 1997.
105. C. A. Grant, D. J. Brockwell, S. E. Radford, and N. H. Thomson. Effects of hydration on the mechanical response of individual collagen fibrils. *Applied Physics Letters*, 92:233902, 2008.
106. K. J. Green and R. D. Goldman. Evidence for an interaction between the cell surface and intermediate filaments in cultured fibroblasts. *Cell Motil Cytoskeleton*, 6:389–405, 1986.
107. L. M. Griffith and T. D. Pollard. Evidence for actin filament-microtubule interaction mediated by microtubule-associated proteins. *J Cell Biol*, 78(3):958–965, 1978.
108. L. M. Griffith and T. D. Pollard. The interaction of actin filaments with microtubules and microtubule-associated proteins. *J Biol Chem*, 257(15):9143–9151, 1982.
109. N. Grizzuti and O. Bifulco. Effects of coalescence and breakup on the steady-state morphology of an immiscible polymer blend in shear flow. *Rheologica Acta*, 36:406–415, 1997.

110. G. Gurland and G. G. Gundersen. Stable, detyrosinated microtubules function to localize vimentin intermediate filaments in fibroblasts. *J Cell Biol*, 131(5):1275–1290, 1995.
111. M. Guthold, W. Liu, E. A. Sparks, L. M. Jawerth, L. Peng, M. Falvo, R. Superfine, R. R. Hantgan, and S. T. Lord. A comparison of the mechanical and structural properties of fibrin fibers with other protein fibers. *Cell Biochem Biophys*, 49:165–181, 2007.
112. M. Guthold, W. Liu, B. Stephens, S. T. Lord, R. R. Hantgan, D. A. Erie, R. M. T. Jr, and R. Superfine. Visualization and mechanical manipulations of individual fibrin fibers suggest that fiber cross section has fractal dimension 1.3. *Biophys J*, 87:42264236, 2004.
113. T. Gutsman, G. E. Fantner, M. Venturoni, A. Ekani-Nkodo, J. B. Thompson, J. H. Kindt, D. E. Morse, D. K. Fygenson, and P. K. Hansma. Evidence that collagen fibrils in tendons are inhomogeneously structured in a tubelike manner. *Biophysical Journal*, 84:25932598, 2003.
114. F. K. Gyoeva and V. I. Gelfand. Coalignment of vimentin intermediate filaments with microtubules depends on kinesin. *Nature*, 353(6343):445–448, 1991.
115. A. K. Harris, D. Stopak, and P. Wild. Fibroblast traction as a mechanism for collagen morphogenesis. *Nature*, 290(5803):249–251, 1981.
116. M. Haw, W. C. K. Poon, P. Pusey, P. Hebraud, and F. Lequeux. Colloidal glasses under shear strain. *Physical Review E*, 58:4673–4682, 1998.
117. M. D. Haw, W. C. K. Poon, and P. N. Pusey. Direct observation of oscillatory-shear-induced order in colloidal suspensions. *Physical Review E*, 57:6859–6864, 1998.
118. D. A. Head, A. J. Levine, and F. C. MacKintosh. Deformation of cross-linked semiflexible polymer networks. *Phys Rev Lett*, 91:108102, 2003.
119. D. A. Head, A. J. Levine, and F. C. MacKintosh. Distinct regimes of elastic response and deformation modes of cross-linked cytoskeletal and semiflexible polymer networks. *Phys Rev E Stat Nonlin Soft Matter Phys*, 68:061907, 2003.
120. R. Heimann, M. L. Shelanski, and R. K. Liem. Microtubule-associated proteins bind specifically to the 70-kDa neurofilament protein. *J Biol Chem*, 260(22):12160–12166, 1985.
121. B. T. Helfand, L. Chang, and R. D. Goldman. Intermediate filaments are dynamic and motile elements of cellular architecture. *J Cell Sci*, 117:133–141, 2004.

122. M. J. Hendrix, E. D. Hay, K. von der Mark, and T. F. Linsenmayer. Immunohistochemical localization of collagen types I and II in the developing chick cornea and tibia by electron microscopy. *Invest Ophthalmol Vis Sci*, 22(3):359–375, 1982.
123. H. Herrmann and U. Aebi. Intermediate filament assembly: fibrillogenesis is driven by decisive dimer-dimer interactions. *Curr Opin Struct Biol*, 8(2):177–185, 1998.
124. H. Herrmann and U. Aebi. Intermediate filament assembly: temperature sensitivity and polymorphism. *Cell Mol Life Sci*, 55(11):1416–1431, 1999.
125. H. Herrmann and U. Aebi. Intermediate filaments and their associates: multi-talented structural elements specifying cytoarchitecture and cytodynamics. *Curr Opin Cell Biol*, 12(1):79–90, 2000.
126. H. Herrmann and U. Aebi. Intermediate filaments: molecular structure, assembly mechanism, and integration into functionally distinct intracellular Scaffolds. *Annu Rev Biochem*, 73:749–789, 2004.
127. H. Herrmann, H. Bar, L. Kreplak, S. V. Strelkov, and U. Aebi. Intermediate filaments: from cell architecture to nanomechanics. *Nat Rev Mol Cell Biol*, 8(7):562–573, 2007.
128. H. Herrmann, M. Haner, M. Brettel, N. O. Ku, and U. Aebi. Characterization of distinct early assembly units of different intermediate filament proteins. *J Mol Biol*, 286(5):1403–1420, 1999.
129. H. Herrmann, M. Haner, M. Brettel, S. A. Muller, K. N. Goldie, B. Fedtke, A. Lustig, W. W. Franke, and U. Aebi. Structure and assembly properties of the intermediate filament protein vimentin: the role of its head, rod and tail domains. *J Mol Biol*, 264(5):933–953, 1996.
130. H. Herrmann, M. Hesse, M. Reichenzeller, U. Aebi, and T. M. Magin. Functional complexity of intermediate filament cytoskeletons: from structure to assembly to gene ablation. *Int Rev Cytol*, 223:83–175, 2003.
131. H. Herrmann, L. Kreplak, and U. Aebi. Isolation, characterization, and in vitro assembly of intermediate filaments. *Methods Cell Biol*, 78:3–24, 2004.
132. H. Herrmann and G. Wiche. Plectin and IFAP-300K are homologous proteins binding to microtubule-associated proteins 1 and 2 and to the 240-kilodalton subunit of spectrin. *J Biol Chem*, 262(3):1320–1325, 1987.
133. C. Heussinger, M. Bathe, and E. Frey. Statistical mechanics of semiflexible bundles of wormlike polymer chains. *Phys Rev Lett*, 99:048101, 2007.
134. C. Heussinger and E. Frey. Floppy modes and nonaffine deformations in random fiber networks. *Phys Rev Lett*, 97(10):105501, 2006.

135. C. Heussinger, B. Schaefer, and E. Frey. Nonaffine rubber elasticity for stiff polymer networks. *Phys Rev E*, 76:031906, 2007.
136. B. Hinner, M. Tempel, E. Sackmann, K. Kroy, , and E. Frey. Entanglement, elasticity, and viscous relaxation of actin solutions. *Phys. Rev. Lett.*, 81:26142617, 1998.
137. N. Hirokawa. Cross-linker system between neurofilaments, microtubules, and membranous organelles in frog axons revealed by the quick-freeze, deep-etching method. *J Cell Biol*, 94(1):129–142, 1982.
138. M. Hohenadl, T. Storz, H. Kirpal, K. Kroy, and R. Merkel. Desmin filaments studied by quasi-elastic light scattering. *Biophys J*, 77(4):2199–2209, 1999.
139. D. F. Holmes and K. E. Kadler. The precision of lateral size control in the assembly of corneal collagen fibrils. *J. Mol. Biol*, 345:773–784, 2005.
140. T. Horio and H. Hotani. Visualization of the dynamic instability of individual microtubules by dark-field microscopy. *Nature*, 321(6070):605–607, 1986.
141. J. R. Houser, N. E. Hudson, L. Ping, E. T. O. III, and R. Superfine. Evidence that alpha-C region is origin of low modulus, high extensibility, and strain stiffening in fibrin fibers. *Biophys J.*, 99:3038–3047, 2010.
142. S. Hsu, A. M. Jamieson, and J. Blackwell. Viscoelastic studies of extracellular matrix interactions in a model native collagen gel system. *Biorheology*, 31(1):21–36, 1994.
143. N. E. Hudson, J. R. Houser, E. T. O’Brien, R. M. Taylor, R. Superfine, S. Lord, and M. R. Falvo. Stiffening of individual fibrin fibers equitably distributes strain and strengthens networks. *Biophys J*, 98(8):1632–1640, 2010.
144. E. M. Huisman, C. Storm, and G. T. Barkema. Monte carlo study of multiply crosslinked semiflexible polymer networks. *Phys Rev E*, 78:051801, 2008.
145. K. Hyun, J. G. Nam, M. Wilhelm, K. H. Ahn, and S. J. Lee. Nonlinear response of complex fluids under LAOS (large amplitude oscillatory shear) flow. *Rheology Journal*, 15:97–205, 2003.
146. K. Hyun and M. Wilhelm. Establishing a new mechanical nonlinear coefficient Q from FT-Rheology: First investigation of entangled linear and comb polymer model systems. *Macromolecules*, 42:411422, 2009.
147. D. E. Ingber. Tensegrity I. Cell structure and hierarchical systems biology. *J Cell Sci*, 116:1157–1173, 2003.
148. M. Jahnel, T. A. Waigh, and J. R. Lu. Thermal fluctuations of fibrin fibres at short time scales. *Soft Matter*, 4:1438–1442, 2008.

149. P. A. Janmey, E. J. Amis, and J. D. Ferry. Rheology of fibrin clots. VI. Stress relaxation, creep, and differential dynamic modulus of fine clots in large shearing deformations. *J Rheol*, 27:135–153, 1983.
150. P. A. Janmey, U. Euteneuer, P. Traub, and M. Schliwa. Viscoelastic properties of vimentin compared with other filamentous biopolymer networks. *J Cell Biol*, 113(1):155–160, 1991.
151. P. A. Janmey, S. Hvidt, J. Lamb, and T. P. Stossel. Resemblance of actin-binding protein/actin gels to covalently crosslinked networks. *Nature*, 345:89–92, 1990.
152. P. A. Janmey, J. V. Shah, K. P. Janssen, and M. Schliwa. Viscoelasticity of intermediate filament networks. *Subcell Biochem*, 31:381–397, 1998.
153. P. A. Janmey, J. P. Winer, and J. W. Weisel. Fibrin gels and their clinical and bioengineering applications. *J Roy Soc Interface*, 6:1–10, 2009.
154. M. Kaibara, E. Fukada, and K. Sakaoku. Rheological study on network structure of fibrin clots under various conditions. *Biorheology*, 18:23–35, 1981.
155. H. Kang, Q. Wen, P. A. Janmey, J. X. Tang, E. Conti, and F. C. MacKintosh. Nonlinear elasticity of stiff filament networks: Strain stiffening, negative normal stress, and filament alignment in fibrin gels. *J Phys Chem B*, 113:3799–3805, 2009.
156. L. J. Kaufman, C. P. Brangwynne, K. E. Kasza, E. Filippidi, V. D. Gordon, T. S. Deisboeck, and D. A. Weitz. Glioma expansion in collagen I matrices: Analyzing collagen concentration-dependent growth and motility patterns. *Biophys J*, 89:635–650, 2005.
157. M. Kerker. *The scattering of light and other electromagnetic radiation*. New York: Academic, 1969.
158. N. Kikuchi, A. Ehrlicher, D. Koch, J. A. Kas, S. Ramaswamy, and M. Rao. Buckling, stiffening, and negative dissipation in the dynamics of a biopolymer in an active medium. *Proc Natl Acad Sci U S A*, 106(47):19776–19779, 2009.
159. C. O. Klein, H. W. Spiess, A. Calin, C. Balan, and M. Wilhelm. Separation of the nonlinear oscillatory response into a superposition of linear, strain hardening, strain softening, and wall slip response. *Macromolecules*, 40:42504259, 2007.
160. G. H. Koenderink, M. Atakhorrami, F. C. MacKintosh, and C. F. Schmidt. High-frequency stress relaxation in semiflexible polymer solutions and networks. *Phys Rev Lett*, 96:138307, 2006.
161. S. Koster, Y. C. Lin, H. Herrmann, and D. A. Weitz. Nanomechanics of vimentin intermediate filament networks. *Soft Matter*, 6:1910–1914, 2010.

162. K. N. Krahn, C. V. C. Bouten, S. van Tuijl, M. A. M. J. van Zandvoort, and M. Merckx. Fluorescently labeled collagen binding proteins allow specific visualization of collagen in tissues and live cell culture. *Anal Biochem*, 350(2):177–185, 2006.
163. L. Kreplak, H. Bar, J. F. Leterrier, H. Herrmann, and U. Aebi. Exploring the mechanical behavior of single intermediate filaments. *J Mol Biol*, 354:569577, 2005.
164. L. Kreplak and D. Fudge. Biomechanical properties of intermediate filaments: from tissues to single filaments and back. *Bioessays*, 29(1):26–35, 2007.
165. M. H. Kroll, J. D. Hellums, L. V. McIntire, A. I. Schafer, and J. L. Moake. Platelets and shear stress. *Blood*, 88:1525–1541, 1996.
166. K. Kroy and E. Frey. Force-extension relation and plateau modulus for wormlike chains. *Phys Rev Lett*, 77:306–309, 1996.
167. L. D. Landau and E. M. Lifshitz. *Theory of elasticity*. Butterworth-Heinemann, 1995.
168. C. M. Lapiere, B. Nusgens, and G. E. Pierard. Interaction between collagen type I and type III in conditioning bundles organization. *Connective Tissue Research*, 5:21–29, 1977.
169. N. Laurens, P. Koolwijk, and M. P. M. D. Maat. Fibrin structure and wound healing. *J Thromb Haemost*, 4:932–939, 2008.
170. S. Leikin, D. C. Rau, and V. A. Parsegian. Direct measurement of forces between self-assembled proteins: temperature-dependent exponential forces between collagen triple helices. *PNAS*, 91(1):276–280, 1994.
171. J. F. Leterrier, P. A. Janmey, and J. Eyer. Microtubule-independent regulation of neurofilament interactions in vitro by neurofilament-bound ATPase activities. *Biochem Biophys Res Commun*, 384(1):37–42, 2009.
172. J. F. Leterrier, J. Kas, J. Hartwig, R. Vegners, and P. A. Janmey. Mechanical effects of neurofilament cross-bridges. Modulation by phosphorylation, lipids, and interactions with F-actin. *J Biol Chem*, 271(26):15687–15694, 1996.
173. J. F. Leterrier, R. K. Liem, and M. L. Shelanski. Interactions between neurofilaments and microtubule-associated proteins: a possible mechanism for intraorganellar bridging. *J Cell Biol*, 95(3):982–986, 1982.
174. G. Liao and G. G. Gundersen. Kinesin is a candidate for cross-bridging microtubules and intermediate filaments - selective binding of kinesin to detyrosinated tubulin and vimentin. *J Biol Chem.*, 273:9797–9803, 1998.
175. O. Lieleg and A. R. Bausch. Cross-linker unbinding and self-similarity in bundled cytoskeletal networks. *Phys Rev Lett*, 99(15):158105, 2007.

176. O. Lieleg, M. M. A. E. Claessens, and A. R. Bausch. Structure and dynamics of cross-linked actin networks. *Soft Matter*, 6:218–225, 2010.
177. O. Lieleg, M. M. A. E. Claessens, C. Heussinger, E. Frey, and A. R. Bausch. Mechanics of bundled semiflexible polymer networks. *Phys Rev Lett*, 99(8):088102, 2007.
178. N. Lieska, H. Y. Yang, and R. D. Goldman. Purification of the 300K intermediate filament-associated protein and its in vitro recombination with intermediate filaments. *J Cell Biol*, 101(3):802–813, 1985.
179. B. B. C. Lim, E. H. Lee, M. Sotomayor, and K. Schulten. Molecular basis of fibrin clot elasticity. *Structure*, 16:449–459, 2008.
180. Y. Lin, C. P. Broedersz, A. C. Rowat, T. Wedig, H. Herrmann, F. C. Mackintosh, and D. A. Weitz. Divalent cations crosslink vimentin intermediate filament tail domains to regulate network mechanics. *J Mol Biol*, 399(4):637–644, 2010.
181. Y. Lin, G. H. Koenderink, F. C. MacKintosh, and D. A. Weitz. Control of non-linear elasticity in F-actin networks with microtubules. *Soft Matter*, 7:902–906, 2011.
182. Y. Lin, N. Y. Yao, C. P. Broedersz, H. Herrmann, F. C. MacKintosh, and D. A. Weitz. Origin of elasticity in intermediate filament networks. *PRL*, 104:058101, 2010.
183. Y. C. Lin, G. H. Koenderink, F. C. MacKintosh, and D. A. Weitz. Viscoelastic properties of microtubule networks. *Macromolecules*, 40:7714–7720, 2007.
184. T. E. Linsenmayer, E. Gibney, F. Igoe, M. K. Gordon, J. M. Fitch, L. I. Fessler, and D. E. Birk. Type V collagen: Molecular structure and fibrillar organization of the chicken alpha 1(V) NH2-terminal domain, a putative regulator of corneal fibrillogenesis. *Journal of Cell Biology*, 121:1181–1189, 1993.
185. T. F. Linsenmayer, J. M. Fitch, and D. E. Birk. Heterotypic collagen fibrils and stabilizing collagens. Controlling elements in corneal morphogenesis? *Ann N Y Acad Sci.*, 580:143–160, 1990.
186. T. F. Linsenmayer, J. M. Fitch, J. Gross, and R. Mayne. Are collagen fibrils in the developing avian cornea composed of two different collagen types? Evidence from monoclonal antibody studies. *Ann N Y Acad Sci*, 460:232–245, 1985.
187. R. Litvinov, S. Yakovlev, G. Tsurupa, O. Gorkun, L. Medved, and J. Weisel. Direct evidence for specific interactions of the fibrinogen alpha-C domains with the central E region and with each other. *Biochemistry*, 46:9133–9142, 2007.

188. R. I. Litvinov, O. V. Gorkun, D. K. Galanakis, S. Yakovlev, L. Medved, H. Shuman, and J. W. Weisel. Polymerization of fibrin: direct observation and quantification of individual B:b knob-hole interactions. *Blood*, 109:130–138, 2007.
189. J. Liu, K. E. Kasza, G. H. Koenderink, D. Vader, C. P. Broedersz, F. C. MacKintosh, and D. A. Weitz. Microscopic origins of nonlinear elasticity of biopolymer networks. preprint, www.seas.harvard.edu/projects/weitzlab/publications.html.
190. J. Liu, G. H. Koenderink, K. E. Kasza, F. C. MacKintosh, and D. A. Weitz. Visualizing the strain field in semiflexible polymer networks: strain fluctuations and nonlinear rheology of F-actin gels. *Phys Rev Lett*, 98:198304, 2007.
191. W. Liu, L. M. Jawerth, E. A. Sparks, M. R. Falvo, R. R. Hantgan, R. Superfine, S. T. Lord, and M. Guthold. Fibrin fibers have extraordinary extensibility and elasticity. *Science*, 313:634, 2006.
192. X. Liu and G. H. Pollack. Mechanics of F-actin characterized with micro-fabricated cantilevers. *Biophys J*, 83(5):2705–2715, 2002.
193. L. Lorand and R. M. Graham. Transglutaminases: crosslinking enzymes with pleiotropic functions. *Nat Rev Mol Cell Biol*, 4(2):140–156, 2003.
194. V. Lulevich, H. Yang, R. R. Isseroff, and G. Liu. Single cell mechanics of keratinocyte cells. *Ultramicroscopy*, 110(12):1435–1442, 2010.
195. F. C. MacKintosh, J. Kas, and P. A. Janmey. Elasticity of semiflexible biopolymer networks. *Phys Rev Lett*, 75:4425–4428, 1995.
196. F. C. Mackintosh and C. F. Schmidt. Active cellular materials. *Curr Opin Cell Biol*, 22(1):29–35, 2010.
197. F. Malfait and A. D. Paepe. Molecular genetics in classic Ehlers-Danlos syndrome. *Am J Med Genet C Semin Med Genet*, 139C(1):17–23, 2005.
198. B. Marian and M. W. Danner. Skin tumor promotion is associated with increased type V collagen content in the dermis. *Carcinogenesis*, 8(1):151–154, 1987.
199. J. L. Martys, C. L. Ho, R. K. Liem, and G. G. Gundersen. Intermediate filaments in motion: observations of intermediate filaments in cells using green fluorescent protein-vimentin. *Mol Biol Cell*, 10(5):1289–1295, 1999.
200. P. A. McKee, P. Mattock, and R. L. Hill. Subunit structure of human fibrinogen, soluble fibrin, and cross-linked insoluble fibrin. *Proc Natl Acad Sci U S A*, 66(3):738–744, 1970.
201. P. A. McKee, L. A. Rogers, E. Marler, and R. L. Hill. The subunit polypeptides of human fibrinogen. *Arch Biochem Biophys*, 116(1):271–279, 1966.

202. J. S. McLaughlin, T. F. Linsenmayer, and D. E. Birk. Type V collagen synthesis and deposition by chicken embryo corneal fibroblasts in vitro. *J Cell Sci*, 94:371–379, 1989.
203. L. V. Medved', O. V. Gorkun, V. F. Manyakov, and V. A. Belitser. The role of fibrinogen alpha C-domains in the fibrin assembly process. *FEBS Lett*, 181(1):109–112, 1985.
204. K. Misof, G. Rapp, and P. Fratzl. A new molecular model for collagen elasticity based on synchrotron X-ray scattering evidence. *Biophys J*, 72(3):1376–1381, 1997.
205. H. Miyazaki and K. Hayashi. Tensile tests of collagen fibers obtained from the rabbit patellar tendon. *Biomedical Microdevices*, 2:151–157, 1999.
206. K. Mizuno, E. Adachi, Y. Imamura, O. Katsumata, and T. Hayashi. The fibril structure of type V collagen triple-helical domain. *Micron*, 32(3):317–323, 2001.
207. D. C. Morse. Viscoelasticity of tightly entangled solutions of semiflexible polymers. *Phys Rev E*, 58:R1237–R1240, 1998.
208. M. W. Mosesson, K. R. Siebenlist, J. F. Hainfeld, and J. S. Wall. The covalent structure of factor XIIIa crosslinked fibrinogen fibrils. *J Struct Biol*, 115(1):88–101, 1995.
209. N. Mucke, K. Klenin, R. Kirmse, M. Bussiek, H. Herrmann, M. Hafner, and J. Langowski. Filamentous biopolymers on surfaces: atomic force microscopy images compared with brownian dynamics simulation of filament deposition. *PLoS One*, 4(11):e7756, 2009.
210. N. Mucke, L. Kreplak, R. Kirmse, T. Wedig, H. Herrmann, U. Aebi, and J. Langowski. Assessing the flexibility of intermediate filaments by atomic force microscopy. *J Mol Biol*, 335(5):1241–1250, 2004.
211. M. F. Muller, H. Ris, and J. D. Ferry. Electron microscopy of fine fibrin clots and fine and coarse fibrin films. Observations of fibers in cross-section and in deformed states. *J Mol Biol*, 174(2):369–384, 1984.
212. J. G. Nama, K. Hyunb, K. H. Ahna, and S. J. Lee. Prediction of normal stresses under large amplitude oscillatory shear flow. *Journal of Non-Newtonian Fluid Mechanics*, 150:1–10, 2008.
213. G. W. Nelb, C. Gerth, and J. D. Ferry. Rheology of fibrin clots. III. Shear creep and creep recovery of fine ligated and coarse unligated clots. *Biophys Chem*, 5:377–387, 1976.
214. G. W. Nelb, G. W. Kamykowski, and J. D. Ferry. Kinetics of ligation of fibrin oligomers. *J Biol Chem*, 255(13):6398–6402, 1980.

-
215. G. W. Nelb, G. W. Kamykowski, and J. D. Ferry. Rheology of fibrin clots. V. Shear modulus, creep, and creep recovery of fine unligated clots. *Biophys Chem*, 13(1):15–23, 1981.
 216. S. Newman, M. Cloitre, C. Allain, G. Forgacs, and D. Beysens. Viscosity and elasticity during collagen assembly in vitro: relevance to matrix-driven translocation. *Biopolymers*, 41(3):337–347, 1997.
 217. Y. Nicolas, M. Paquesa, D. van den Ended, J. K. G. Dhonte, R. C. van Polanenc, A. Knaebelf, A. Steyerf, J. P. Munchf, T. B. J. Blijdensteina, and G. A. van Akena. Microrheology: new methods to approach the functional properties of food. *Food Hydrocolloids*, 17:907–913, 2003.
 218. L. Norlen, S. Masich, K. N. Goldie, and A. Hoenger. Structural analysis of vimentin and keratin intermediate filaments by cryo-electron tomography. *Exp Cell Res*, 313(10):2217–2227, 2007.
 219. C. R. Nunes, M. T. Roedersheimer, S. J. Simske, and M. W. Luttgcs. Effect of microgravity, temperature, and concentration on fibrin and collagen assembly. *Microgravity Sci Tec*, 8:125–130, 1995.
 220. E. T. O’Brien, E. D. Salmon, R. A. Walker, and H. P. Erickson. Effects of magnesium on the dynamic instability of individual microtubules. *Biochemistry*, 29(28):6648–6656, 1990.
 221. T. Odijk. The statistics and dynamics of confined or entangled stiff polymers. *Macromolecules*, 16:1340–1344, 1986.
 222. T. Odijk. Stiff chains and filaments under tension. *Macromolecules*, 28:7016–7018, 1995.
 223. M. B. Omary, P. A. Coulombe, and W. H. I. McLean. Intermediate filament proteins and their associated diseases. *N Engl J Med*, 351(20):2087–2100, 2004.
 224. P. R. Onck, T. Koeman, T. van Dillen, and E. van der Giessen. Alternative explanation of stiffening in cross-linked semiflexible networks. *Phys Rev Lett*, 95:178102, 2005.
 225. J. P. R. O. Orgel, T. C. Irving, A. Miller, and T. J. Wess. Microfibrillar structure of type I collagen in situ. *PNAS*, 103(24):9001–9005, 2006.
 226. R. G. Oshima. Intermediate filaments: a historical perspective. *Exp Cell Res*, 313(10):1981–1994, 2007.
 227. J. M. Paramio and J. L. Jorcano. Beyond structure: do intermediate filaments modulate cell signalling? *Bioessays*, 24(9):836–844, 2002.
 228. D. A. D. Parry, S. V. Strelkov, P. Burkhard, U. Aebi, and H. Herrmann. Towards a molecular description of intermediate filament structure and assembly. *Exp Cell Res*, 313(10):2204–2216, 2007.

229. V. Pelletier, N. Gal, P. Fournier, and M. L. Kilfoil. Microrheology of microtubule solutions and actin-microtubule composite networks. *Phys Rev Lett*, 102(18):188303, 2009.
230. J. A. Petruska and A. J. Hodge. A subunit model for the tropocollagen macromolecule. *PNAS*, 51:871–876, 1964.
231. W. Philippoff. Vibrational measurements with large amplitudes. *Trans. Soc. Rheol*, 10:DOI:10.1122/1.549049, 1966.
232. I. K. Piechocka, R. G. Bacabac, M. Potters, F. C. MacKintosh, , and G. H. Koenderink. Structural hierarchy governs fibrin gel mechanics. *Biophysical Journal*, 98:2281–2289, 2010.
233. A. C. Pipkin. *Lectures on viscoelasticity theory*. Springer, 1972.
234. M. Plodinec, M. Loparic, R. Suetterlin, H. Herrmann, U. Aebi, and C. Schoenenberger. The nanomechanical properties of rat fibroblasts are modulated by interfering with the vimentin intermediate filament system. *J Struct Biol*, 174(3):476–484, 2011.
235. S. Portet, N. Mucke, R. Kirmse, J. Langowski, M. Beil, and H. Herrmann. Vimentin intermediate filament formation: in vitro measurement and mathematical modeling of the filament length distribution during assembly. *Langmuir*, 25(15):8817–8823, 2009.
236. J. Pourati, A. Maniotis, D. Spiegel, J. L. Schaffer, J. P. Butler, J. J. Fredberg, D. E. Ingber, D. Stamenovic, and N. Wang. Is cytoskeletal tension a major determinant of cell deformability in adherent endothelial cells? *Am J Physiol*, 274:C1283–C1289, 1998.
237. V. Prahlad, M. Yoon, R. D. Moir, R. D. Vale, and R. D. Goldman. Rapid movements of vimentin on microtubule tracks: kinesin-dependent assembly of intermediate filament networks. *J Cell Biol*, 143(1):159–170, 1998.
238. I. Pucci-Minafra and C. Luparello. Type V/type I collagen interactions in vitro and growth-inhibitory effect of hybrid substrates on 8701-BC carcinoma cells. *J Submicrosc Cytol Pathol*, 23(1):67–74, 1991.
239. P. K. Purohit, R. I. Litvinov, A. E. X. Brown, D. E. Discher, and J. W. Weisel. Protein unfolding accounts for the unusual mechanical behavior of fibrin networks. *Acta Biomater*, 7(6):2374–2383, 2011.
240. Z. Qin, M. J. Buehler, and L. Kreplak. A multi-scale approach to understand the mechanobiology of intermediate filaments. *J Biomech*, 43(1):15–22, 2010.
241. Z. Qin, L. Kreplak, and M. J. Buehler. Hierarchical structure controls nanomechanical properties of vimentin intermediate filaments. *PLoS One*, 4(10):e7294, 2009.

242. S. Rammensee, P. A. Janmey, and A. R. Bausch. Mechanical and structural properties of in vitro neurofilament hydrogels. *Eur Biophys J*, 36(6):661–668, 2007.
243. C. B. Raub, J. Unruh, V. Suresh, T. Krasieva, T. Lindmo, E. Gratton, B. J. Tromberg, and S. C. George. Image correlation spectroscopy of multiphoton images correlates with collagen mechanical properties. *Biophys J*, 94(6):2361–2373, 2008.
244. C. S. Regula, J. R. Pfeiffer, and R. D. Berlin. Microtubule assembly and disassembly at alkaline pH. *J Cell Biol*, 89(1):45–53, 1981.
245. M. J. Reimers and J. M. Dealy. Sliding plate rheometer studies of concentrated polystyrene solutions: Nonlinear viscoelasticity and wall slip of two high molecular weight polymers in tricresyl phosphate. *J. Rheol*, 42:527–548, 1998.
246. W. Roberts, L. Lorand, and L. Mockros. Viscoelastic properties of fibrin clots. *Biorheology*, 10:29–42, 1973.
247. W. W. Roberts, O. Kramer, R. W. Rosser, F. H. Nestler, and J. D. Ferry. Rheology of fibrin clots. I. Dynamic viscoelastic properties and fluid permeation. *Biophys Chem*, 1:152–160, 1974.
248. B. E. Rodriguez, M. S. Wolfe, and E. W. Kaler. Reversible solidification of hard-spherulike dispersions due to colloidal crystallization. *Langmuir*, 9:1215, 1993.
249. O. C. Rodriguez, A. W. Schaefer, C. A. Mandato, P. Forscher, W. M. Bement, and C. M. Waterman-Storer. Conserved microtubule-actin interactions in cell movement and morphogenesis. *Nat Cell Biol*, 5(7):599–609, 2003.
250. B. A. Roeder, K. Kokini, and S. L. Voytic-Harbin. Fibril microstructure affects strain transition within collagen extracellular matrices. *Journal of Biomechanical Engineering*, 131:031004–1, 2009.
251. A. M. Romanic, E. Adachi, K. E. Kadler, Y. Hojima, and D. J. Prockop. Copolymerization of pNcollagen III and collagen I. pNcollagen III decreases the rate of incorporation of collagen I into fibrils, the amount of collagen I incorporated, and the diameter of the fibrils formed. *J Biol Chem*, 266(19):12703–12709, 1991.
252. M. Romanowska, H. Hinsch, N. Kirchgessner, M. Giesen, M. Degawa, B. Hoffmann, E. Frey, and R. Merkel. Direct observation of the tube model in F-actin solutions: Tube dimensions and curvatures. *EPL*, 86:26003, 2009.
253. F. J. Roska and J. D. Ferry. Studies of fibrin film. I. Stress relaxation and birefringence. *Biopolymers*, 21:1811–1832, 1982.

254. R. W. Rosser, W. W. Roberts, and J. D. Ferry. Rheology of fibrin clots. IV. Darcy constants and fiber thickness. *Biophys Chem*, 7(2):153–157, 1977.
255. M. Roulet, F. Ruggiero, G. Karsenty, and D. LeGuellec. A comprehensive study of the spatial and temporal expression of the col5a1 gene in mouse embryos: a clue for understanding collagen V function in developing connective tissues. *Cell Tissue Res*, 327(2):323–332, 2007.
256. F. Rouyer, S. Cohen-Addad, R. Hohler, P. Sollich, and S. M. Fielding. The large amplitude oscillatory strain response of aqueous foam: Strain localization and full stress fourier spectrum. *Eur Phys J E Soft Matter*, 27:309–321, 2008.
257. M. Rubinstein and S. Panyukov. Nonaffine deformation and elasticity of polymer networks. *Macromolecules*, 30:8036–8044, 1997.
258. E. A. Ryan, L. F. Mockros, A. M. Stern, and L. Lorand. Influence of a natural and a synthetic inhibitor of factor XIIIa on fibrin clot rheology. *Biophys J*, 77:2827–2836, 1999.
259. E. A. Ryan, L. F. Mockros, J. W. Weisel, and L. Lorand. Structural origins of fibrin clot rheology. *Biophys J*, 77:2813–2826, 1999.
260. E. A. Sandera, T. Stylianopoulosb, R. T. Tranquillo, and V. H. Barocas. Image-based multiscale modeling predicts tissue-level and network-level fiber reorganization in stretched cell-compacted collagen gels. *PNAS*, 20:17675–80, 2009.
261. H. M. H. F. Sanders, G. J. Strijkers, W. J. M. Mulder, H. P. Huinink, S. J. F. Erich, O. C. G. Adan, N. A. J. M. Sommerdijk, M. Merckx, and K. Nicolay. Morphology, binding behavior and MR-properties of paramagnetic collagen-binding liposomes. *Contrast Media Mol Imaging*, 4(2):81–88, 2009.
262. R. L. Satcher and C. F. Dewey. Theoretical estimates of mechanical properties of the endothelial cell cytoskeleton. *Biophys J*, 71:109–118, 1996.
263. K. M. Schmoller, P. Fernandez, R. C. Arevalo, D. L. Blair, and A. R. Bausch. Cyclic hardening in bundled actin networks. *Nat Commun*, 1:134, 2010.
264. M. Schopferer, H. Bar, B. Hochstein, S. Sharma, N. Mucke, H. Herrmann, and N. Willenbacher. Desmin and vimentin intermediate filament networks: their viscoelastic properties investigated by mechanical rheometry. *J Mol Biol*, 388(1):133–143, 2009.
265. C. Semmrich, R. J. Larsen, and A. R. Bausch. Nonlinear mechanics of entangled F-actin solutions. *Soft Matter*, 4:1675–1680, 2008.
266. J. V. Shah, L. A. Flanagan, D. Bahk, and P. Janmey. Reptation of microtubules in F-actin networks : effects of filament stiffness and network topology on reptation dynamics. *Mat. Res. Soc.*, 489:27–31, 1998.

-
267. J. V. Shah and P. A. Janmey. Strain hardening of fibrin gels and plasma clots. *Rheol Acta*, 36:262–268, 1997.
268. R. C. Sharma, A. Papagiannopoulos, and T. A. Waigh. Optical coherence tomography picorheology of biopolymer solutions. *Appl Phys Lett*, 92:173903, 2008.
269. L. Shen and L. Lorand. Contribution of fibrin stabilization to clot strength. Supplementation of factor XIII-deficient plasma with the purified zymogen. *J Clin Invest*, 71(5):1336–1341, 1983.
270. L. L. Shen, J. Hermans, J. McDonagh, R. P. McDonagh, and M. Carr. Effects of calcium ion and covalent crosslinking on formation and elasticity of fibrin cells. *Thromb Res*, 6:255–265, 1975.
271. Z. L. Shen, M. R. Dodge, H. Kahn, R. Ballarini, and S. J. Eppell. In vitro fracture testing of submicron diameter collagen fibril specimens. *Biophys J*, 99(6):1986–1995, 2010.
272. F. H. Silver and D. E. Birk. Molecular structure of collagen in solution: comparison of types I, II, III and V. *International Journal of Biological Macromolecules*, 6:125–132, 1984.
273. F. H. Silver, A. Ebrahimi, and P. B. Snowhill. Viscoelastic properties of self-assembled type I collagen fibers: molecular basis of elastic and viscous behaviors. *Connect Tissue Res*, 43(4):569–580, 2002.
274. L. Sivakumar and G. Agarwal. The influence of discoidin domain receptor 2 on the persistence length of collagen type I fibers. *Biomaterials*, 31(18):4802–4808, 2010.
275. A. V. Sokolova, L. Kreplak, T. Wedig, N. Mucke, D. I. Svergun, H. Herrmann, U. Aebi, and S. V. Strelkov. Monitoring intermediate filament assembly by small-angle x-ray scattering reveals the molecular architecture of assembly intermediates. *Proc Natl Acad Sci U S A*, 103(44):16206–16211, 2006.
276. T. Solomon and M. J. Solomon. Stacking fault structure in shear-induced colloidal crystallization. *J Chem Phys*, 124(13):134905, 2006.
277. A. S. C. Soon, S. E. Stabenfeldt, W. E. Brown, and T. H. Barker. Engineering fibrin matrices: The engagement of polymerization pockets through fibrin knob technology for the delivery and retention of therapeutic proteins. *Biomaterials*, 31:1944–54, 2010.
278. D. Stamenovic, N. Wang, and D. E. Ingber. Cellular tensegrity models in cell-substrate interactions. *Cellular Engineering: Micromechanics at the Biomolecular Interface*, editor M. R. King, Elsevier Science, 195–211, 2006.

279. K. F. Standeven, R. A. S. Ariens, and P. J. Grant. The molecular physiology and pathology of fibrin structure/function. *Blood Rev*, 19:275–288, 2005.
280. K. F. Standeven, A. M. Carter, P. J. Grant, J. W. Weisel, I. Chernysh, L. Masova, S. T. Lord, and R. A. S. Ariens. Functional analysis of fibrin gamma-chain cross-linking by activated factor XIII: determination of a cross-linking pattern that maximizes clot stiffness. *Blood*, 110:902–907, 2007.
281. E. D. Stasio, C. Nagaswami, J. W. Weisel, and E. D. Cera. Cl^- regulates the structure of the fibrin clot. *Biophys J*, 75:19731979, 1998.
282. A. M. Stein, D. A. Vader, L. M. Jawerth, D. A. Weitz, and L. M. Sander. An algorithm for extracting the network geometry of three-dimensional collagen gels. *Journal of Microscopy*, 232:463475, 2008.
283. A. M. Stein, D. A. Vader, D. A. Weitz, and L. M. Sander. The micromechanics of three dimensional collagen-I gels. *Complexity*, 16:22–28, 2010.
284. P. Steinert, L. N. Marekov, and D. A. Parry. Diversity of intermediate filament structure. Evidence that the alignment of coiled-coil molecules in vimentin is different from that in keratin intermediate filaments. *J Biol Chem*, 268(33):24916–24925, 1993.
285. C. Storm, J. J. Pastore, F. C. MacKintosh, T. C. Lubensky, and P. A. Janmey. Nonlinear elasticity in biological gels. *Nature*, 435:191–194, 2005.
286. S. V. Strelkov, H. Herrmann, and U. Aebi. Molecular architecture of intermediate filaments. *Bioessays*, 25(3):243–251, 2003.
287. K. Stuart and A. Panitch. Characterization of gels composed of blends of collagen I, collagen III, and chondroitin sulfate. *Biomacromolecules*, 10(1):25–31, 2009.
288. Y. L. Sun, Z. P. Luo, A. Fertala, and K. N. An. Direct quantification of the flexibility of type I collagen monomer. *Biochem Biophys Res Commun*, 295(2):382–386, 2002.
289. T. Suzaki, H. Sakai, S. Endo, I. Kimura, and Y. Shigenaka. Effects of various anions, glutamate and GTP on microtubule assembly in vitro. *J Biochem*, 84(1):75–81, 1978.
290. T. M. Svitkina, A. B. Verkhovsky, and G. G. Borisy. Plectin sidearms mediate interaction of intermediate filaments with microtubules and other components of the cytoskeleton. *J Cell Biol*, 135(4):991–1007, 1996.
291. I. Szeverenyi, A. J. Cassidy, C. W. Chung, B. T. K. Lee, J. E. A. Common, S. C. Ogg, H. Chen, S. Y. Sim, W. L. P. Goh, K. W. Ng, J. A. Simpson, L. L. Chee, G. H. Eng, B. Li, D. P. Lunny, D. Chuon, A. Venkatesh, K. H.

- Khoo, W. H. I. McLean, Y. P. Lim, and E. B. Lane. The human intermediate filament database: comprehensive information on a gene family involved in many human diseases. *Hum Mutat*, 29(3):351–360, 2008.
292. X. Trepap, M. Grabulosa, F. Puig, G. N. Maksym, D. Navajas, and R. Farre. Viscoelasticity of human alveolar epithelial cells subjected to stretch. *Am J Physiol Lung Cell Mol Physiol*, 287(5):L1025–L1034, 2004.
293. Y. Tseng, K. M. An, O. Esue, and D. Wirtz. The bimodal role of filamin in controlling the architecture and mechanics of F-actin networks. *J Biol Chem*, 279(3):1819–1826, Jan 2004.
294. D. Vader, A. Kabla, D. Weitz, and L. Mahadevan. Strain-induced alignment in collagen gels. *PLoS One*, 4(6):e5902, 2009.
295. J. van den Akker, A. Pisteu, E. N. T. P. Bakker, and E. van Bavel. Decomposition cross-correlation for analysis of collagen matrix deformation by single smooth muscle cells. *Med Biol Eng Comput*, 46(5):443–450, 2008.
296. J. A. J. van der Rijt, K. O. van der Werf, M. L. Bennink, P. J. Dijkstra, and J. Feijen. Micromechanical testing of individual collagen fibrils. *Macromol Biosci*, 6(9):697–702, 2006.
297. D. Velegol and F. Lanni. Cell traction forces on soft biomaterials. I. Microrheology of type I collagen gels. *Biophys J*, 81(3):1786–1792, 2001.
298. W. A. Voter, C. Lucaveche, and H. P. Erickson. Concentration of protein in fibrin fibers and fibrinogen polymers determined by refractive index matching. *Biopolymers*, 25:2375–2384, 1986.
299. O. I. Wagner, S. Rammensee, N. Korde, Q. Wen, J. F. Leterrier, and P. A. Janmey. Softness, strength and self-repair in intermediate filament networks. *Exp Cell Res*, 313(10):2228–2235, 2007.
300. R. A. Walker, E. T. O'Brien, N. K. Pryer, M. F. Soboeiro, W. A. Voter, H. P. Erickson, and E. D. Salmon. Dynamic instability of individual microtubules analyzed by video light microscopy: rate constants and transition frequencies. *J Cell Biol*, 107(4):1437–1448, 1988.
301. N. Wang, J. P. Butler, and D. E. Ingber. Mechanotransduction across the cell surface and through the cytoskeleton. *Science*, 260:1124–1127, 1993.
302. N. Wang and D. Stamenovic. Contribution of intermediate filaments to cell stiffness, stiffening, and growth. *Am J Physiol Cell Physiol*, 279(1):C188–C194, 2000.
303. P. G. Waxman, A. A. del Campo, M. C. Lowe, and E. Hamel. Induction of polymerization of purified tubulin by sulfonate buffers. Marked differences between 4-morpholineethanesulfonate (Mes) and 1,4-piperazineethanesulfonate (Pipes). *Eur J Biochem*, 120(1):129–136, 1981.
304. J. W. Weisel. Enigmas of blood clot elasticity. *Science*, 320:456–457, 2008.

305. J. W. Weisel, C. W. Francis, C. Nagaswami, and V. J. Marder. Determination of the topology of factor XIIIa-induced fibrin gamma-chain cross-links by electron microscopy of ligated fragments. *J Biol Chem.*, 268:26618–26624, 1993.
306. J. W. Weisel and L. Medved. The structure and function of the alpha-C domains of fibrinogen. *Ann NY Acad Sci*, 936:312–327, 2001.
307. Q. Wen, A. Basu, J. P. Winer, A. Yodh, and P. A. Janmey. Local and global deformations in a strain-stiffening fibrin gel. *New J Phys*, 9:428, 2007.
308. R. J. Wenstrup, J. B. Florer, J. M. Davidson, C. L. Phillips, B. J. Pfeiffer, D. W. Menezes, I. Chervoneva, and D. E. Birk. Murine model of the Ehlers-Danlos syndrome. col5a1 haploinsufficiency disrupts collagen fibril assembly at multiple stages. *J Biol Chem*, 281(18):12888–12895, 2006.
309. G. Wiche. Role of plectin in cytoskeleton organization and dynamics. *J Cell Sci*, 111:2477–2486, 1998.
310. U. Wickert, N. Mucke, T. Wedig, S. A. Muller, U. Aebi, and H. Herrmann. Characterization of the in vitro co-assembly process of the intermediate filament proteins vimentin and desmin: mixed polymers at all stages of assembly. *Eur J Cell Biol*, 84:379–391, 2005.
311. J. Wilhelm and E. Frey. Elasticity of stiff polymer networks. *Phys Rev Lett*, 91:108103, 2003.
312. M. Wilhelm. Fourier-transform rheology. *Macromol Mater Eng*, 287:83–105, 2002.
313. M. Wilhelm, D. Maring, and H. W. Spiess. Fourier-Transform Rheology. *Rheol. Acta*, 37:399, 1998.
314. N. Willenbacher, C. Oelschlaeger, and M. Schopferer. Broad bandwidth optical and mechanical rheometry of wormlike micelle solutions. *Phys Rev Lett*, 99:068302, 2007.
315. B. R. Williams, R. A. Gelman, D. C. Poppke, and K. A. Piez. Collagen fibril formation. Optimal in vitro conditions and preliminary kinetic results. *J Biol Chem*, 253(18):6578–6585, 1978.
316. T. Wilson. *Confocal Microscopy*. Academic, San Diego, 1990.
317. G. C. Wood and M. K. Keech. The formation of fibrils from collagen solutions. 1. The effect of experimental conditions: kinetic and electron-microscope studies. *Biochem J*, 75:588–598, 1960.
318. Y. L. Wu, J. H. J. Brand, J. L. A. van Gemert, J. Verkerk, H. Wisman, A. van Blaaderen, and A. Imhof. A new parallel plate shear cell for in situ real-space measurements of complex fluids under shear flow. *Rev Sci Instrum*, 78(10):103902, 2007.

-
319. Y. L. Wu, D. Derks, A. van Blaaderen, and A. Imhof. Melting and crystallization of colloidal hard-sphere suspensions under shear. *PNAS*, 106(26):10564–10569, 2009.
 320. J. Xu, Y. Tseng, and D. Wirtz. Strain hardening of actin filament networks. *J Biophys Chem*, 275:35886–35892, 2000.
 321. L. Yang, K. O. van der Werf, C. F. C. Fitie, M. L. Bennink, P. J. Dijkstra, and J. Feijen. Mechanical properties of native and cross-linked type I collagen fibrils. *Biophys J*, 94(6):2204–2211, 2008.
 322. Y. Yang and L. J. Kaufman. Rheology and confocal reflectance microscopy as probes of mechanical properties and structure during collagen and collagen/hyaluronan self-assembly. *Biophys J*, 96(4):1566–1585, 2009.
 323. Y. Yang, L. M. Leone, and L. J. Kaufman. Elastic moduli of collagen gels can be predicted from two-dimensional confocal microscopy. *Biophys J*, 97(7):2051–2060, 2009.
 324. Z. Yang, J. M. Kollman, L. Pandi, and R. F. Doolittle. Crystal structure of native chicken fibrinogen at 2.7 Angstrom resolution. *Biochemistry*, 40:12515–12523, 2001.
 325. N. Y. Yao, C. P. Broedersz, Y. C. Lin, K. E. Kasza, F. C. MacKintosh, and D. A. Weitz. Elasticity in ionically cross-linked neurofilament networks. *Biophysical Journal*, 98:2147–2153, 2010.
 326. N. Y. Yao, R. J. Larsen, and D. A. Weitz. Probing nonlinear rheology with inertio-elastic oscillations. *J Rheol*, 52:1013–1025, 2008.
 327. C. Yeromonahos, B. Polack, and F. Caton. Nanostructure of the fibrin clot. *Biophys J*, 99(7):2018–2027, 2010.
 328. T. Yeung, P. C. Georges, L. A. Flanagan, B. Marg, M. Ortiz, M. Funaki, N. Zahir, W. Ming, V. Weaver, and P. A. Janmey. Effects of substrate stiffness on cell morphology, cytoskeletal structure, and adhesion. *Cell Motil Cytoskeleton*, 60(1):24–34, 2005.
 329. M. Yoon, R. D. Moir, V. Prahlad, and R. D. Goldman. Motile properties of vimentin intermediate filament networks in living cells. *J Cell Biol*, 143(1):147–157, 1998.

SUMMARY

Cells are active biological materials that can adapt their properties to changing circumstances. Using a dynamic internal cytoskeleton (CSK), cells can tune their behavior from fluid- to more solid-like, which helps to combine mechanical strength with shape plasticity. The presence of an external fibrous extracellular matrix (ECM) around cells further helps to protect them against mechanical deformations such as tension, compression, or shear.

Both, the CSK and the ECM are viscoelastic networks built from biopolymers that exhibit a highly nonlinear elastic response to an applied mechanical load. This nonlinear response is believed to protect cells from tearing under large external stresses. Moreover, the nonlinear elastic response of the ECM enables cells to actively modify the stiffness of the ECM. Contractile forces that they exert on the ECM create a locally stiffer environment in which cells can achieve optimal spreading. This induced stiffness gradient helps cells to mechanically interact with each other.

Depending on filament bending rigidity and the degree of crosslinking, the strain-stiffening can originate from either an entropic mechanism related to stretching of the thermally undulated filaments or from an enthalpic mechanism where network rearrangement or filament buckling take place. Both of these models for network elasticity assume that the filaments behave as rods with simple homogeneous and isotropic mechanical properties. Thus, the complex internal architecture of biopolymers is neglected while describing the origin of elastic nonlinearity. This disregard of the structural hierarchy of filaments may miss crucial effects of the mechanical features of the subunits and their spatial arrangement in the fibers on fiber and network mechanics.

The goal of this thesis was to elucidate the role of the supramolecular, internal architecture of protein filaments in the macroscopic nonlinear elasticity of the cytoskeletal and extracellular matrix networks they form. To this end, I used imaging and light scattering techniques to characterize the morphology and supramolecular structure of different biopolymer filaments and macroscopic shear rheology to relate the structural properties of those filaments to the network mechanical response, as described in Chapter 2. I used mainly two rheological techniques, namely prestress measurements and the large amplitude oscillatory shear (LAOS) method. As a complementary analysis of the nonlinear elasticity, I decomposed the raw LAOS nonlinear stress/strain data with the use of Fourier Transform spectra and Lissajous plots as shown in Chapter 5. I found that these methods have similar sensitivity to the onset of elastic nonlinearity as measurements of the differential modulus.

In Chapter 3, I show that the nonlinear elastic response of the major blood-clotting protein, fibrin, is governed by the complex architecture of fibrin fila-

ments. In the limit of “so-called” *coarse fibrin clots* that are composed of thick bundles of thin, semiflexible protofibrils, fibrin gels exhibit a complex strain-stiffening response under shear. This mechanism originates from the entropic stretching of the fibrin bundles at the network scale, followed by filament backbone stretching and entropic stretching of flexible domains inside the fibers at the filament scale. This (close to) affine response of fibrin networks is possible due to the loose connection between protofibrils into fibers that makes the fibers very flexible despite their large diameter. The sequential stretching processes on different length scales that occur with increasing levels of load endow fibrin clots with an extraordinary resilience against large deformations.

In order to obtain better insight into the contribution of the internal architecture of fibrin fibers, and especially the role of the protofibrils, in the nonlinear mechanics of fibrin networks, I continued my research in the limit of “so-called” *fine clots* as shown in Chapter 4. In this regime, fibrin filaments are thin bundles of only 3 protofibrils. Since the protofibrils are only loosely associated, they behave independently from each other and contribute individually to the mechanical response of the network. Similar to *coarse clots*, the *fine clots* show a complex nonlinear dependence on stress that can be accounted for by an affine entropic model. Under increased level of stress, the thermally undulated shape of the protofibrils is first stretched, which is followed by backbone extension and shear-induced protofibril alignment. The results obtained from fibrin clots assembled in two different structural limits taken together show that the hierarchical bundle-like architecture of fibrin filaments plays a key role in determining the nonlinear mechanical response of fibrin networks.

In vivo, cytoskeletal and ECM filaments form sometimes hybrid (or heterotypic) structures built from different type of protein subunits. The molecular composition may change molecular packing inside the filaments and interactions among filaments by changing the interactions between subunits. An example of this is collagen, the most abundant protein in the human body. Collagen fibers in most tissues consist predominantly of collagen type I, which forms heterotypic fibrils with another collagen, namely type V. This co-assembly is thought to provide a mechanism for diameter regulation. In Chapter 6 I show that the presence of different molecular types in the filament structure reduces the stiffness of hybrid collagen networks compared to homotypic collagen I gels. This suggests that collagen V changes the intermolecular interaction among tropocollagen molecules within or between fibers. The network mechanics show nonlinear strain-stiffening behavior, which is common for crosslinked semiflexible polymer gels. The origin of this nonlinear response appears to be enthalpic, in contrast to fibrin networks, where the nonlinearity is entropic in origin. This unfortunately hampers the quantitative interpretation of the influence of collagen V content on the mechanics of heterotypic collagen networks, since there is no analytical model describing this regime. One way to overcome this problem is to identify and quantify the network deformation mechanism under shear *in situ* by optical microscopy. Looking at the response of individual filaments in a shear network could help to understand better the origin of the nonaffine mechanical behavior. Therefore, in Chapter 8 I present a prototype of a shear device that can be used to visualize changes in the microstructure of biopolymer

networks under large shear by confocal microscopy. By embedding probe beads inside the network, one may directly quantify nonaffinity in the strain field and directly observe fiber bending and stretching or network rupture at large stress. Such measurements are critical to obtain a full understanding of the influence of the multiscale structure of biopolymer networks on their remarkable nonlinear elasticity.

Structural hierarchy of biopolymers results in differences in the bending rigidities of different types of filaments. The coexistence of multiple mechanically disparate structures in the cell interior and exterior suggests that the mechanical properties of networks composed of different filament types may be interdependent. To study the influence of interactions between different filament types on composite network mechanics I implemented a new *in vitro* model system. In the final chapter of this thesis, Chapter 7, I set up a composite network of microtubules (MTs) and vimentin (a type III intermediate filament (IFs) protein) in order to identify for the first time the buffer conditions that will allow for simultaneous assembly of both proteins. While the composite actin-IF or actin-MT networks have been already studied before, the effect of coexistence of intermediate filaments and microtubules is not yet known. I observed that the microtubules embedded in vimentin networks are bent, possibly due to forces exerted by polymerizing vimentin filaments. Rheological data showed that the stiffness and nonlinear response of this composite vimentin-MT system are intermediate between those of the pure components.

All the results presented in this thesis highlight the importance of the internal architecture of biopolymer filaments for the mechanical response of the networks they form. Structural hierarchy in the filament architecture results in multiple mechanical regimes that together ensure high network robustness and decrease the likelihood of catastrophic failure. Mutations in the basic structural units may lead to defects in polymer assembly, changes in mechanical properties and finally pathological conditions. Many human diseases are related to the formation of cytoskeletal or ECM filaments with a distorted internal architecture, which are too weak to withstand large load or too strong to dissipate mechanical stresses. An understanding of the contribution of the hierarchical structure to mechanical stability of biopolymers and their nonlinear mechanics is therefore crucial for future treatment strategies that may eliminate cure or certain diseases.

SAMENVATTING

Cellen hebben materiaaleigenschappen die ze zelf actief kunnen aanpassen al naar gelang de omstandigheden. Middels een dynamisch intern cytoskelet (CSK) zijn deze biologische systemen in staat hun gedrag te veranderen van vloeibaar naar vast, waardoor mechanische sterkte gecombineerd wordt met de mogelijkheid om vorm te veranderen en te bewegen. Een externe vezelige extracellulaire matrix (ECM) die de cellen omringt, verschaft de cellen verdere bescherming tegen mechanische vervorming zoals spanning, samendrukking of schuifspanning.

Het CSK en de ECM zijn beiden viscoelastische netwerken die zijn opgebouwd uit biopolymeren die zeer niet lineair reageren op een mechanische belasting. Deze niet lineaire reactie wordt verantwoordelijk gehouden voor de bescherming van cellen tegen grote externe spanningen ter voorkoming van scheuren. Bovendien zorgt het niet lineaire elastische gedrag van de ECM ervoor dat cellen de stijfheid van de ECM actief kunnen veranderen. De samen-trekkende krachten die de cellen op de ECM uitoefenen creëren lokaal een stijver netwerk waarin de cellen optimaal kunnen hechten en met elkaar kunnen communiceren over grote afstanden door mechanische interacties.

Afhankelijk van de buigstijfheid van het filament en de mate van kruisverbindingen in het netwerk kan het verstevigingsgedrag voortkomen uit óf een entropisch mechanisme gerelateerd aan het uitrekken van thermisch fluctuerende filamenten, óf uit een enthalpisch mechanisme waarin herstructurering van het netwerk plaatsvindt. Beide modellen voor de elasticiteit van het netwerk gaan er van uit dat de filamenten zich gedragen als staven met simpele homogene en isotrope mechanische eigenschappen. Hierdoor wordt de complexe interne architectuur van de biopolymeren genegeerd bij de beschrijving van de oorsprong van de elastische niet-lineairiteit. Het niet in acht nemen van de structurele hiërarchie van de filamenten zou ertoe kunnen leiden dat cruciale effecten gemist worden van de mechanische kenmerken van de eenheden en hun ruimtelijke rangschikking binnen de vezels.

Het doel van dit proefschrift was om de invloed van de supramoleculaire interne architectuur van de filamenten van het cytoskelet en extracellulaire matrix op netwerk mechanica op te helderen. Om dit te verwezenlijken heb ik enerzijds visualisatietechnieken en lichtverstrooiingstechnieken toegepast om de morfologie en de supramoleculaire structuur van verschillende eiwitfilamenten te karakteriseren, en anderzijds door middel van macroscopisch schuifspanningsreologie de mechanische reactie van het netwerk gemeten. Deze experimentele technieken worden beschreven in Hoofdstuk 2. Hoofdzakelijk heb ik twee reologische technieken gebruikt, namelijk metingen met een voorspanning en de Large Amplitude Oscillatory Shear (LAOS) methode. Zoals beschreven in Hoofdstuk 5, lev-

ert de LAOS methode gedetailleerde informatie over de niet lineaire elasticiteit wanneer de ruwe stress/strain data worden ontleed door middel van Fourier transformatie of met Lissajous plots. Ik heb gevonden dat LAOS een soortgelijke gevoeligheid vertoont voor het begin van de elastische niet-lineairiteit als meer conventionele metingen van de differentiele modulus.

In Hoofdstuk 3 onderzoek ik het mechanische gedrag van fibrine, een eiwit dat fibreuze bloedproppen vormt om wonden te dichten en wondgenezing te stimuleren. Ik laat zien dat de niet-lineaire elastische reactie van fibrine netwerken beheerst wordt door de complexe architectuur van de fibrine filamenten. In de fysiologische limiet waarin de vezels bestaan uit dikke bundels van dunne, semiflexibele protofibrillen, vertonen fibrine-gelen een complex verstevigingsgedrag bij een aangebrachte schuifspanning. Dit fenomeen vindt zijn oorsprong in het entropisch rekken van de fibrine-bundels op de schaal van het netwerk, gevolgd door het rekken van de ruggengraat van het filament en het entropisch rekken van flexibele domeinen binnenin de vezels. Ik stel een mechanisme voor waarbij deze nagenoeg affiene (strek) reactie van het fibrine netwerk wordt veroorzaakt door de losse verbindingen tussen de protofibrillen die de vezels vormen. Deze losse verbindingen maken de vezels verrassend flexibel ondanks hun grote diameter. Het stapsgewijs rekken op verschillende lengteschalen dat plaatsvindt met toenemende belasting geeft fibrine-stolsels een buitengewone veerkracht tegen grote vervormingen.

Om beter inzicht te krijgen in de rol van de interne architectuur van de fibrinevezels, en in het bijzonder de rol van de protofibrillen, binnen de niet-lineaire mechanica van de netwerken, heb ik mijn onderzoek vervolgd in de limiet van de zogenaamde fijne proppen, beschreven in Hoofdstuk 4. In dit regime bestaan de fibrinevezels uit dunne bundels van slechts 3 protofibrillen. Aangezien de protofibrillen slechts losjes zijn verbonden met elkaar, gedragen zij zich onafhankelijk van elkaar en dragen elk individueel bij aan het mechanische gedrag van het netwerk. Net als in het geval van de meer fysiologische netwerken van dikke fibers laten de fijne proppen een complexe niet-lineaire spanningsafhankelijkheid zien die verklaard kan worden aan de hand van een affiene entropisch model. Bij toenemende spanning wordt eerst de thermische fluctuerende vorm van de protofilamenten gerekt, gevolgd door rekking van de ruggengraat en uitlijning van de protofilamenten door de opgelegde schuifspanning. Samen laten de resultaten voor proppen van dikke of dunne fibrine vezels zien dat de hiërarchische bundelarchitectuur van de fibrinefilamenten een sleutelrol speelt in het niet-lineaire mechanische gedrag van fibrine netwerken.

In vivo zijn de vezels van het cytoskelet en de ECM vaak hybride (of heterotypische) structuren die opgebouwd zijn uit verschillende soorten eiwit-eenheden. De moleculaire samenstelling kan de moleculaire stapeling binnen de filamenten veranderen en ook de interacties tussen filamenten beïnvloeden. Een voorbeeld is collageen, een van de meest voorkomende eiwitten in het menselijk lichaam. Weefsels bestaan meestal uit collageenvezels die hoofdzakelijk opgebouwd zijn uit collageen type I; dit eiwit kan heterotypische vezels vormen met een ander type collageen, namelijk type V. Gedacht wordt dat deze co-assemblage de vezels voorziet van een mechanisme voor regulatie van de diameter. In Hoofdstuk 6 laat ik zien dat de aanwezigheid van collageen type V in

vezels de stijfheid van hybride collageennetwerken vermindert vergeleken met pure (homotypische) collageen I gelen. Dit suggereert dat collageen V de intermoleculaire interacties tussen tropocollageen moleculen verandert binnenin, of tussen, de vezels. De mechanica van het netwerk laat niet-lineair verstevigingsgedrag zien, wat gebruikelijk is voor kruisverbonden semiflexibele polymeergelen. De oorzaak van dit niet-lineaire gedrag lijkt enthalpisch te zijn, in tegenstelling fibrinenetwerken, waar de niet-lineariteit een entropische oorzaak heeft. Helaas wordt hierdoor de kwantitatieve interpretatie van de invloed van collageen V op de mechanica van de heterotypische collageennetwerken gehinderd, aangezien er geen analytisch model beschikbaar is dat dit regime beschrijft. Een manier om dit probleem te omzeilen is het direct identificeren en kwantificeren van de vervormingsmechanica van het netwerk onder schuifspanning met behulp van optische microscopie. Het observeren van het gedrag van de individuele filamenten in een netwerk onder schuifspanning zou kunnen helpen een beter begrip te krijgen van de oorsprong van het niet-affiene mechanische gedrag. Om dit te bewerkstelligen presenteer ik in Hoofdstuk 8 een prototype van een schuifspanningsapparaat dat aangewend kan worden om veranderingen in de microstructuur van biopolymeernetwerken te visualiseren onder grote schuifspanning met behulp van confocale microscopie. Door middel van micrometer grote bolletjes ingebed in het netwerk kan de niet-affiniteit in het vervormingsveld direct gekwantificeerd worden. Bovendien kan het buigen en rekken van de vezels of scheuren in het netwerk geobserveerd worden bij grote spanningen. Deze metingen zullen in de toekomst doorslaggevend zijn voor het verkrijgen van een compleet begrip van de invloed van de verschillende structurele lengteschalen in biopolymeernetwerken op hun niet-lineaire elasticiteit.

De structurele hiërarchie van biopolymeren resulteert in verschillen in buigstijfheden van verschillende soorten filamenten. De coëxistentie van meerdere mechanisch ongelijksoortige structuren binnen in de cel en buiten de cel suggereert dat de mechanische eigenschappen van samengestelde netwerken mogelijk synergistisch zijn. Om te kunnen onderzoeken of dit zo is heb ik een nieuw *in vitro* systeem geïmplementeerd. In het laatste hoofdstuk van dit proefschrift, Hoofdstuk 7, heb ik een modelsysteem opgezet bestaande uit opgezuiverde cellulaire microtubuli (MT) en vimentine (een type III eitwit van de familie van intermediaire filamenten (IF)). Ik heb systematisch de samenstelling van de buffer gevarieerd, om condities te vinden waaronder beide eiwitten gelijktijdig op de correcte wijze assembleren. In het verleden is reeds onderzoek gedaan naar samengestelde actine-IF en actine-MT netwerken, maar samengestelde IF-MT zijn tot op heden nog niet onderzocht. Ik heb geobserveerd dat de microtubuli binnen een vimentine netwerk gebogen zijn, waarschijnlijk door krachten uitgeoefend door de polymerisatie van de vimentine filamenten. Reologie laat zien dat de stijfheid en het niet-lineaire gedrag van het samengestelde vimentin-MT systeem liggen tussen die van de netwerken bestaande uit slechts 1 component.

Alle resultaten gepresenteerd in dit proefschrift benadrukken het belang van de interne architectuur van biopolymeerfilamenten voor het mechanische gedrag van de door hen gevormde netwerken. Structurele hiërarchie binnen de filament architectuur resulteert in meerdere mechanische regimes die er samen voor zor-

gen dat de netwerken robuust zijn en die de waarschijnlijkheid van een catastrofale bezwijking verminderen. Mutaties in de structurele basiseenheden kunnen dan ook leiden tot defecten in de architectuur en daaruit volgende mechanische eigenschappen. Meerdere ziektes die voorkomen bij de mens zijn gerelateerd aan de vorming van eiwitfilamenten in het cytoskelet of de ECM met een verwrongen interne architectuur, die te zwak zijn om een grote belasting te weerstaan of te sterk zijn om mechanische spanningen te verspreiden. Een beter inzicht in het aandeel van de hiërarchische structuur aan de mechanische stabiliteit van biopolymeren is daarom cruciaal om behandelingsstrategieën te vinden die bepaalde ziektes zouden kunnen uitschakelen of genezen.

ACKNOWLEDGEMENT

A physicist that enters a biolab for the first time is like an elephant in a pottery shop: clumsy and afraid to move around and destroy everything that surrounds him. This is more or less the memory that I have from my first few weeks at AMOLF. After breaking a few beakers and a pH electrode, discovering the miracle of flowing a sample through an insanely small flow chamber, I realized that the nanotechnology knowledge I gained during my previous studies was of no use in a biological lab. At that point, I started to wonder what was I doing there. With time, however, I came to the conclusion that it was not so hard and that the wetlab is not such a scary place, even though handling proteins may be quite challenging. I realized this mainly due to the other two group members at the time: Gijsje and Marina. Gijsje, thank you for supervision, outstanding advice and guidance from the earliest stages of this research. Thank you for your invaluable suggestions that helped me to grow as a researcher and a young scientist and, most of all, thank you for giving me a chance to become a part of this exciting scientific world. Your constant enthusiasm and passion for science has always been very motivating. Marina, without your constant help my start in such a new environment would have been extremely hard. Thank you for teaching me all the basic laboratory assays and tricks that were essential for my subsequent research. It was great being the first two students in the new group and watching the group slowly grow larger. Nefeli (a Greek baking master), Saskia (a true family woman), Jan-Willem (a wise fellow) and Mel (the invisible man), thank you for creating a warm family atmosphere early on. Jeanette, thank you for your daily portion of fine sarcasm and for “Samenvatting”. Without you, reading this part of thesis would be totally unintelligible due to my “poor” Dutch; Feng, Björn, Baldo, José, Brian, Corianne, Marjolein, Magdalena, Martijn, Marijn thank you for your willingness to share your bright thoughts during group meetings and for suggestions in the lab.

This work could not have been done without the contribution of the great theoreticians that I was lucky to meet and collaborate with during the last four years. Fred, Chase, Enrico, Moumita, Martin and Misha, thank you for all the shared ideas during our joint VU/AMOLF meetings and the broadband data flow while writing papers. Kees and Liesbeth it was always great to discuss experimental data with you. I would like to thank you all for those fruitful meetings, both the official and the less official ones that made me realize how important good communication between theoretical and experimental groups is in terms of scientific output. I would also like to send special thanks abroad to my collaborators in Heidelberg. Harald, Stefan, Tatjana, Dorothee and Norbert, thank you for introducing me to the world of intermediate filaments, for sharing knowledge and protocols, and for your help with experiments and encourage-

ment over the years. Thank you for showing me that science is not only about competing in one's field but is also about bringing people together so that they can work and share knowledge like one big family. Harald, Ueli and Bob, the example that you set for young researchers and the experience that you share with them is priceless.

During my PhD work I had the great pleasure to work with three excellent students: Anne, Karin and Yvette. Girls, thank you for your beautiful data and your commitment to the projects that were assigned to you. I could not possibly have asked for better students. Anne, I will always remember the sound of classical music coming from the rheometer basement. Yvette, your great enthusiasm for work was downright contagious, so do not lose it. Karin, it is great to see how you are already becoming a passionate and independent scientist. This is especially significant now that you have started your PhD and will probably soon have your own students. I also would like to thank Wim for a year of a challenging work and a sharp tongue :).

I am finishing my work here with many great memories not only from AMOLF but also from outside work. Laura, Christian and Paige, thank you for all those challenging climbing evenings and dinners in Heidelberg. Rutger, thank you for lending me your guitar and giving me a chance to rediscover the sound of chords after so many years. Frank, Julien, Marco M. and Marco S., thank you for being around, for chatting, laughing, providing technical help and a chestnut party (I think my hands were never so dirty and my clothes never smelled so bad from the smoke than that evening). Svenja and Gabor, thank you for enjoyable moments while traveling towards our home lands and back to rainy Holland. Bączek, Papa Rétif, Princess, Thijsje, Piste Bully fan and Łuki, thank you for great snowboarding trips, freezing crêpes lunches in the Alps, pizza dinners, boat trips, New Years Eve, shared plant and much, much more. I am going to miss you guys a lot and cannot imagine the moment when I will have to finally say goodbye to you. Roland, Chris, Saskia and Moshe, my roommates in the old AMOLF building, thank you for making my beginnings in a foreign country so easy and enjoyably. Sarah and Philippe, it was great to have you as roommates in the new building, even though it was impossible for me to follow your conversations that were too often in French :). Sarah, I love your stubbornness. Philippe, I admire your experimental/theoretical multitasking. Marjon, even though we were not roommates it still seemed like you were just next door, laughing and always pumping my mood up.

Being happy in a foreign country does not depend only on the people that surround you but also on the feeling that whatever will happen, there is always this one place that you can go back to and see beloved faces. Therefore, last but not least I would like to offer thanks from deep in my heart to Łukasz and my family. (W pełni szczęśliwy może być tylko ten kto wie, że gdzieś tam w świecie jest takie jedno małe miejsce, do którego w razie potrzeby może zawsze wrócić i uspokoić rozkołataną serce. Dlatego na samym końcu, chciałabym podziękować Łukaszowi i mojej wspaniałej rodzinie). Dziękuję Wam za Wasze wsparcie i motywację przez te wszystkie lata. Mamo, Tato, dziękuję za bycie wspaniałymi rodzicami i za Waszą troskę. Babciu, Dziadku, dziękuję za te wszystkie rozmowy przez telefon, dzięki którym czułam się bliżej domu. Maciej, Kasia P.

and Kasia J., dzięki za bycie tak wspaniałym rodzeństwem. To, że zawsze mogę Was wszystkich zobaczyć jak wracam do domu dodaje mi sił. Szkoda tylko, że na co dzień dzieli nas tyle kilometrów... Pusio, dziękuję Ci za tą przygodę, za wspaniałe cztery lata i za to, że przy Tobie czuję się bezpiecznie.

CURRICULUM VITAE

Izabela Katarzyna Piechocka was born in Poznań, Polen on August 21, 1982. She obtained her high school diploma in 2001 at the II Liceum Ogólnokształcące im. Generałowej Zamoyskiej i Heleny Modrzejewskiej in Poznań. In September 2001 she started her studies of Technical Physics at the Poznań University of Technology. She finished her Master's degree in the Physics of Materials and Nanotechnology, with a thesis entitled *Technology of oxide barrier creation on crystalline substrates [Si(111), Au(111)] and its characterization by means of scanning tunnelin microscopy*, in June 2006. After graduating, she started her PhD research in the group of Prof. Dr. Gijsje H. Koenderink at the FOM Institute AMOLF in Amsterdam in 2007. The results of this work are presented in this thesis. Upon receiving her PhD, Izabela will work as a post-doctoral fellow on FOM/ProFibrix Mini IPP project. She will study the biomechanical properties and cellular mechanoreponse in fibrin networks prepared from recombinant fibrinogen variants.